Spring 5-15-2022

Thermal Management Using Liquid-vapor Phase Change in Nanochannels

Sajag Poudel
Syracuse University

Abstract

Superior wettability of porous medium marks their potential to be used in the field of thermal management employing phase-change heat transfer. Comprehending the phenomena of wicking and liquid-vapor phase-change in micro/nano structured surfaces are key aspects towards advancing heat transfer solutions. In this work, fundamental understanding of droplet wicking, thin-film evaporation, and their subsequent application of heat-flux removal for cooling technology is first reported. The latter part of the dissertation is related to the disjoining pressure driven flow of nanoscale liquid film and liquid-vapor phase change in nano confinement.

First, experimental and numerical investigation of droplet wicking in ~728 nm height cross-connected buried SiO_2 nanochannels, with micropores of diameter ~2 μm at each intersection, is accomplished. The micropores allow water from a droplet placed on the surface to wick into the channels as well as allow thin-film evaporation from a meniscus. Experimental data in wicking-dominant regime are found to be in good agreement with analytical models and can be used to predict the wicking distance evolution in such nanochannels. Later, numerical technique of computational fluid dynamics (CFD) is employed to understand the dynamics of evaporating menisci in nanochannels and micropores. Evaporation flux at the meniscus interface of channels/pores is estimated over time. Local contact line regions are found to form underneath the pores when the meniscus recedes in the channels, thus rapidly enhancing evaporation flux as a power-law function of time. Temporal variation of wicking flux velocity and pressure gradient in the nanochannels is also independently computed, from which the viscous resistance variation is estimated and compared to the theoretical prediction. Further, to comprehend the effect of high-temperature on droplet spreading and evaporation over the nanochannels sample, experiments are conducted on a heated surface at temperatures ranging from 35°C to 90°C. Evaporation flux from

the nanochannels/micropores is estimated from the droplet experiments but is also independently confirmed via an independent set of experiments where water is continuously fed to the sample through a microtube so that it matches the evaporation rate. Heat flux as high as ~294 W/cm^2 is achieved from channels and pores. The experimental findings are applied to evaluate the use of porous nanochannel geometry in spray cooling application and is found to be capable of passively dissipating high heat fluxes up to ~77 W/cm^2 at temperatures below nucleation, thus highlighting the thermal management potential of the fabricated geometry.

Next, the porous nanochannels device capable to dissipate high heat flux is employed to regulate the temperature of a commercial PV panel by numerically integrating the device on the back face of the panel. The spatial and temporal variation of the PV surface temperature is obtained by solving the energy balance equation numerically and the extent of cooling and the resulting enhancement in the electrical power output is studied in detail. The nanochannels device is found to reduce the PV surface temperature significantly with an average cooling of 31.5 ^{o}C. Additionally, the enhancement in the electrical power output by ~33% and the reduction in the response time to 1/8th demonstrating the porous nanochannels as an efficient thermal management device.

In the later part of the work, an expression is developed for the disjoining pressure in a water film as a function of distance from the surface from prior experimental findings, which is key to understand water transport and liquid-vapor phase change in nanoscale confinement. The expression is implemented in a commercial CFD solver and the disjoining pressure effect on water wicking in nanochannels of height varying from 59 nm to 1 micron is simulated. The simulation results are in excellent agreement with experimental data, thus demonstrating and validating that near-surface molecular interactions can be integrated in continuum numerical simulations.

Following the implementation, transpiration process and the passive water transport in trees of over a height of 100 m is simulated by using a domain comprising of nanopore connected to a tube with a ground-based water tank, thus mimicking the stomata-xylem-soil pathway in trees. In addition, the implementation of disjoining pressure in CFD simulation enabled the study of homogeneous bubble nucleation in nanochannel filled with liquid water. The bubble nucleation temperature was found to be ~125^{o}C which closely matches with the experimental observation (~123^{o}C) providing the evidence on incorporation of the disjoining pressure term to account for the effect of nanoscale confinement. By means of nucleation simulation, lesser-known parameters of homogeneous nucleation including the heat-flux supplied, the liquid film thickness underneath the bubble, etc. are identified which otherwise would been challenging to achieve experimentally.

THERMAL MANAGEMENT USING LIQUID-VAPOR PHASE CHANGE IN NANOCHANNELS

By

Sajag Poudel

B.S., Visvesvaraya Technological University, 2016
M.S., Indian Institute of Technology Kanpur, 2018

DISSERTATION

Submitted in partial fulfillment of the requirements for the Degree of

Doctor of Philosophy in Mechanical & Aerospace Engineering

Syracuse University
May 2022

Dedicated to my family for their unconditional love and support.

Acknowledgments

Foremost, I would like to express my heartfelt gratitude to my advisor Dr. Shalabh Chandra Maroo for providing me the opportunity to work and perform research in the magnificent field of heat transfer. I am grateful to him for his constant guidance, motivation, enthusiasm, and immense knowledge. He has provided me prospects and suitable environment to explore the subject of my interest. He has also helped me a lot for my career planning and several other aspects beyond academics. It would have not been possible to complete my dissertation without his enormous support and supervision during the entire period of my Ph.D. at Syracuse University.

My gratefulness to the thesis committee members Dr. Jeongmin Ahn, Dr. Alan J Levy, Dr. Quinn Qiao, Dr. Radhakrishna Sureshkumar, and Dr. Jianshun Zhang, for their support and valuable comments which helped to improve my dissertation.

I wish to thank Dr. An Zou, former Research Assistant Professor for his mentorship and valuable feedback to my work. His work on fabrication of nanochannels samples and his collaboration in performing experiments greatly benefited my research. He is a good friend and always inspires me to aim high.

I would also like to thank Dr. Kashif Nawaz, Senior Scientist at The Oak Ridge National Laboratory, TN who hosted and supervised my Research Internship during Fall 2021. I also want to acknowledge all the present and former research group members, Manish Gupta, Durgesh Ranjan, Sidharth Raut, Ashok Thapa, Maheswar Chaudhary, for their support and collaboration in the lab.

Finally, my gratitude to my wife Akriti for her unconditional love and support. No sum of appreciation can compare the blessings, support and love from my parents Mr. Jagadish Chandra Upadhyaya and Mrs. Sakuntala Sharma. My gratitude goes to my teachers, mentors, and friends in Syracuse as well as in India and Nepal. I would also like to thank all faculties and staff of MAE Department as well as Syracuse University Administration for providing me all necessary facilities required for the successful completion of this dissertation.

- ***Sajag Poudel***

Table of Contents

List of Figures

List of Tables

Chapter 1. Introduction

1.1 Motivation and Literature Review

The study of phase-change heat transfer enhancement using a micro/nano structured surface has drawn special attention for researchers in the last few decades. Due to the gain in low resistance passive flow as well as high heat flux removal through latent heat, investigation of thin-film evaporation has become extensive in regard to the various thermal management procedures like heat pipes, spray cooling, electrospray [1-5], etc. Evaporation from thin-film, which exists between the intrinsic meniscus and the adsorbed film near the three-phase contact line has the minimum local thermal resistance and accounts for the major share of the total heat transfer in a two-phase system. [6-8] Thus, the systematic study of thin-film evaporation is crucial to fill in the gap for accomplishment in phase change heat transfer enhancement ultimately approaching the theoretical limit [7, 9, 10] for the employed micro/nano structured surface.

Most of the early works in phase-change heat transfer enhancement have focused either on augmenting the contact area of liquid with the substrate [11] or increasing the interfacial area by the use of microstructures which also promotes wicking for the passive supply of liquid [12, 13]. Observation in nature [7, 14] and findings in the lab [15, 16] have shown the promising performance of phase change heat transfer phenomenon in the hierarchical structures. Accordingly, numerous researchers have studied the phase change heat transfer in thin-films employing various micro/nano structured surfaces. [8, 17-22] The investigation of interfacial heat flux existing at an evaporating meniscus (interface) in different geometries (microchannel [8], nanopore [22], V-groove [21], etc.) has offered a commendable understanding of the fundamentals in thin film evaporation as well as an estimation of the theoretical limit of heat flux removable [7, 9, 10] from a micro/nano scale interface. However, the estimation of the heat flux

dissipation from a real 3D porous structure solely based on the results of a single fixed shape static 2D meniscus may be ambiguous especially when the dynamic shape of multiple menisci [23] and the limit of capillary flow [9] comes into picture.

Another important issue concerning thin-film evaporation in a micro/nano structured surface is dry out heat flux [24]. Especially the structures with open geometries like micropillars, nanopillars, nanowires, etc. which although exhibit very promising performance in heat flux dissipation, suffer from dry out due to slower rate of capillary pumping. [25, 26] Accordingly, the study of dry out heat flux in such structures has elected for optimization of the geometry to shift the critical limit of dry out [27]. Although in several such studies [25-28], the role of the heater size used, the rise in superheat of the substrate, etc. is not clear, the idea of enhancing capillarity for accomplishment in high heat flux dissipation is acknowledged.

Besides, many other researchers have also contributed to the field of thin-film evaporation by investigating the phenomenon in a practical 3D microstructured device [1, 29], which indicates the potential use of such devices in heat pipes and spray cooling technologies. Nevertheless, the past works, do not reveal explicit data on the actual performance of cooling procedures like spray cooling or heat pipes as a result of thin-film evaporation. Although the investigation of spray cooling [3, 30, 31] and associated critical limits have shown interesting outcomes, the corresponding database on the cooling performance of a microstructured surface based on thin-film evaporation is still lagging. Furthermore, along with the substantial progress in the investigation of droplet spreading in a flat [32, 33] or a structured [21, 34-36] surface, the sparsely discussed topic of droplet coupled evaporation in a micro/nano structure [37] ought to be brought in the limelight. The study of thin-film evaporation associated with droplet wicking would essentially promote a remarkable advancement in the field of spray cooling [3, 30, 31],

thin-film coatings [38], nano-fabrication [39], ink-jet printing [40], drop-wise cooling [41], etc. Finally, it is desirable to have the design of a nanostructure's geometry based on the combination of different aspects: uniform geometry, greater capillary pumping, and higher porosity yet sufficient mechanical strength. Thus, in the state of the ongoing issues, we expect to unravel the droplet coupled thin-film evaporation in a hierarchical structure and examine its inference in one of the most efficient high heat flux dissipating technology, spray cooling.

1.2 Wicking in Nanoscale Geometries

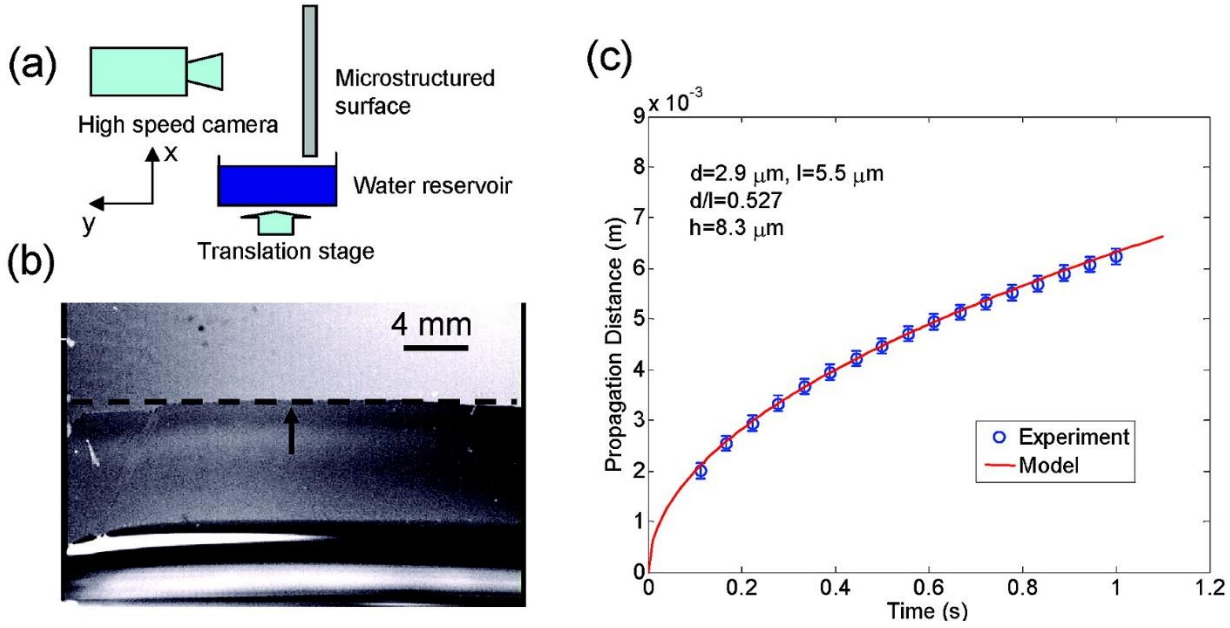

Figure 1.1. Liquid propagation (wicking) on a vertically held surface with micropillars array. (a) Experimental setup (b) High-speed camera indicates the wicking front (c) Evolution of wicking distance with time and comparison of the same with an analytical model. Reprinted with permission from Xiao, Enright, and Wang [42]. Copyright (2010) American Chemical Society.

In phase-change thermal management applications, the wettability of an employed nanostructured device is an important parameter. The importance of wicking also lies in a multitude of heat-flux dissipating applications like pool boiling heat pipes, spray cooling [11, 31, 43-46], etc. In addition to the experimental studies in wicking on micro/nano structured surfaces,

several studies in analytical modeling of wicking dynamics at micro/nanoscale have also been carried out. [42] Such analytical models are capable to predict wicking rate based on the capillary pressure of the employed geometry like micropillars [42], nanochannels [34], etc. Figure 1.1 depicts a typical case of water wicking in a micropillar-arrayed surface along with the comparison of the analytical prediction of wicking distance with the experimental observation.

1.3 Droplet-Coupled-Evaporation

Among the various studies in wicking on micro/nano structured surfaces, the study of droplet spreading and wicking is limited in literature [37]. One of the most efficient mechanisms of thermal management, spray cooling completely relies on the spread and ultimate evaporative cooling of the dispersed droplets. Thus, there lies a need and abundance of opportunities to unravel the fundaments as well as the applied aspect of droplet wicking and eventual evaporation on the micro/nano structured surface.

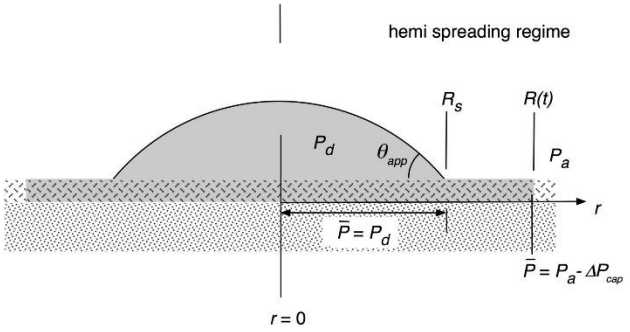

Figure 1.2 Droplet spreading and simultaneously wicking on nanoporous surface. Reprinted with permission from Wemp & Carey [36]. Copyright (2017) American Chemical Society.

Figure 1.2 shows a typical case of droplet wicking on a nanoporous surface [36]. Fundamental aspects of droplet wicking like wicking distance and evaporation rates from the structured surface can be achieved by investigating the droplet-wicking phenomenon.

1.4 Thermal Management Applications

Thermal management is an important aspect of engineering with the application ranging from electronic cooling to energy harnessing. By utilizing a proper cooling technique, higher power output in a photovoltaic can be achieved as depicted in Fig. 1.3 [47]. Similarly, efficient thermal management of electronics is also required in order to realize higher performance and speed of computation. Figure 1.4 demonstrates an exponential growth in power consumption by the CPU of cell phones with time [48]. With the increase in the number of transistors used, heat dissipation becomes an important issue and thus needs to be addressed accordingly.

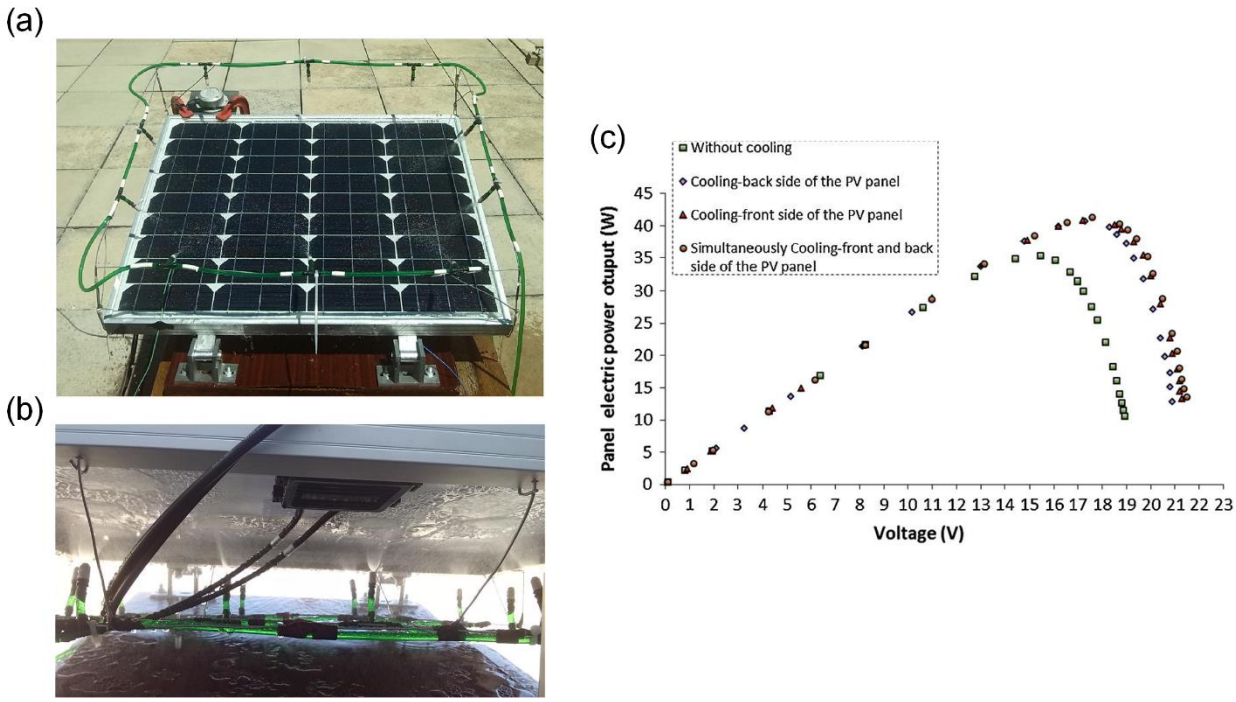

Figure 1.3. Spray cooling on PV panel to achieve higher power output. Reprinted with permission from Nižetić et al. (2016) [47]. Energy Conversion and Management.

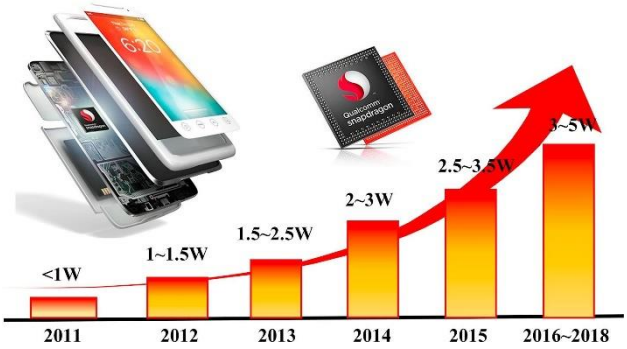

Figure 1.4. Power consumption by CPU processors of cell phones. Reprinted with permission from Tang et al. (2018) [48]. Applied Energy.

Superior wettability of micro/nano structured surfaces in an imperative parameter that marks their potential to be employed in the field of thermal management using phase change heat transfer as well as various other lab-on-chip applications. [8] Various designs of random micro/nano structures like nanowires or nanoporous layers have been explored to study wicking in relation to thermal management. However, a uniform geometry with precisely known porosity has a lot of advantages over random structures in the scenario of modeling the wicking rate [42] and estimating the evaporative cooling performance [9, 24, 26]. The dimension of such uniform structures is in the order of tens of micrometers. [24, 49] The comprehension of wicking and evaporation dynamics on uniform structure with a sub-micron scale would unravel newer insights to wicking and evaporation dynamics ultimately providing better comprehension of thermal management.

Chapter 2: Droplet Wicking in Nanochannels Sample

2.1 Introduction

Wicking is the spread of liquid on a structured or porous medium where the liquid propagation is primarily governed by capillary forces. The importance of studying the mechanism of wicking at small-scale likes is in a multitude of area like heat transfer, printing, painting, propellant transport, etc. Accordingly, many studies have been carried out to comprehend the phenomena on various micro/nano surfaces like nanowires [44], micropillars [4, 24-28, 42], nanopillars [49], nanoporous layer [29, 36], etc. However, the investigation of droplet wicking and ultimate evaporation on a sub-micron scale uniform structured surface is lacking in literature. In this chapter, the study of droplet-coupled-wicking on buried nanochannels samples is reported.

2.2 Methods

For the investigation of droplet wicking and evaporation in a uniform structure of sub-micron scale, a cross-connected buried nanochannels of height H ~ 728 nm is designed as shown in Fig. 2.1. Two different samples of buried nanochannels S5 and S10 are considered where the number '5' or '10' denote the designed width of nanochannel in μm. In a given sample, two sets of channels passing in transverse and lateral directions are interconnected and a micropore of diameter d_p ~ 2 μm is provided at each interconnection. For the fabrication of such geometry (performed by Dr. An Zou, Former Research Assistant Professor at Syracuse University), a patterned sacrificial metal layer of $Cu + Cr$ is deposited on a Si wafer by e-beam evaporator which is, in turn, buried under a 300 nm thick SiO_2 film using plasma-enhanced chemical vapor deposition (PECVD). At the intersection, a hole is created by photolithography followed by dry

etching of SiO_2. Finally, the wafer was immersed in *Cr* etchant to remove the sacrificing *Cu* layer resulting in the buried nanochannels geometry.

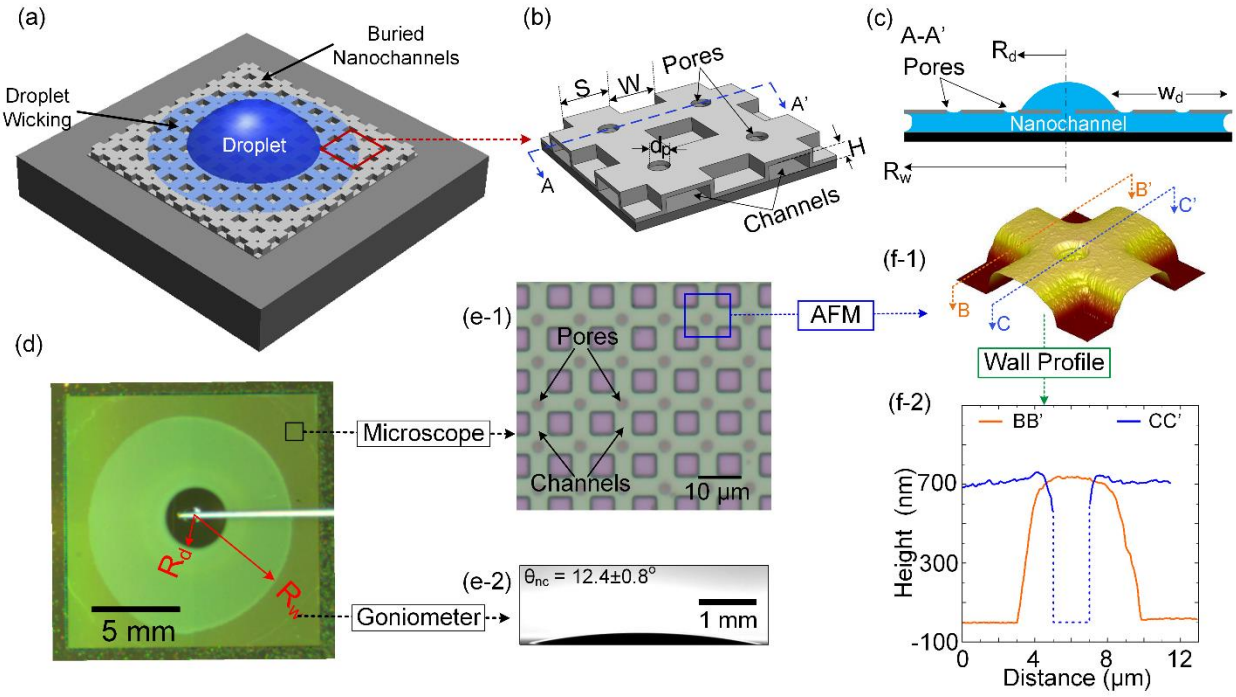

Figure 2.1. The geometry of Cross-connected buried nanochannels sample. (a) Droplet spreading and simultaneously wicking into nanochannels. (b) 2×2 cells of nanochannels. (c) A sectional view of droplet wicking. (d) High-speed camera image of droplet wicking on a sample. (e1) View under a microscope, (e2) Goniometer image and (f) AFM image of a sample. Reprinted with permission from Poudel, Zou, & Maroo [34]. Copyright (2019) American Chemical Society

The design of the height of nanochannels is based on a number of criteria considered as follows:

(i) The height of the nanochannels is limited by the maximum thickness of the sacrificial layers during nanofabrication. The limit is around 1 μm.

(ii) The factors affecting wicking like disjoining pressure, electroviscous effect, etc. come into the picture if the nanochannels height is ~ 100 nm and less.

(iii) The wicking distance should be large enough to conduct analysis with minimum errors in calculation, which prefers a higher channel.

Thus, the channel height is chosen to be ~700 nm i.e., in a sub-micron range, and it turned out to be ~728 nm after nano-fabrication processes. Further details on the design of the cross-connected buried nanochannels sample is available in Appendix A1.

A sketch of a cross-connected nanochannels sample with liquid droplet spreading and simultaneously wicking on it is shown in Fig. 2.1 (a). Similarly, the measurement of the nanochannels geometry: channel width W, spacing S, height H and the micropore diameter d_p are indicated in the isometric view of 2×2 cells of the nanochannels in Fig. 2.1 (b). The geometry of the present sample is designed such that the micropores allow the supply of liquid from bulk into the nanochannels and the interconnections of the channels enable easy liquid exchange (see Fig. 2.1 (c)).

The actual fabricated nanochannels sample of size 1.4 cm × 1.4 cm with a droplet placed on top and simultaneously spreading is depicted in Fig. 2.1 (d) along with the measure of droplet base radius R_d and wicking radius R_w. The sample's view under an optical microscope (see Fig. 2.1 (e1)) and a goniometer image for static contact angle (see Fig. 2.1 (e2)), as well as an AFM image of the fabricated nanochannels sample and the corresponding wall profile (Figs. 2.1 (f1), 2.1 (f2)), are also demonstrated.

For the wicking experiment, a sample with buried nanochannels was placed on a vertical-translation stage as shown in Fig. 2.2. A water droplet of a specific volume was generated using an automatic syringe pump, and the stage was raised slowly to have the droplet touch the top surface of the sample thus causing water to wick into the channels. The needle of the syringe was

coated with a hydrophobic material to avoid any left-over sessile droplet on the needle during droplet deposition on the sample. An automated syringe pump (error < 0.35%) was used to produce the desired droplet volume. The entire process was recorded from the top view using a high-speed camera with a frame rate of 50 fps, and primary wicking parameters: wicking radius (R_w), droplet base radius (R_d) and wicking distance (w_d) were measured with time. The experiment was repeated for all cases of two samples (see Table 2.1).

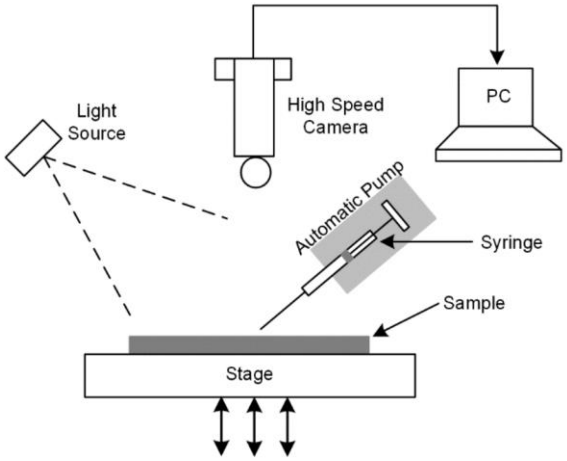

Figure 2.2. Schematic of droplet wicking experiment on nanochannels sample. Reprinted with permission from Poudel, Zou, and Maroo [34]. Copyright (2019) American Chemical Society.

Table 2.1 Different cases of droplet wicking experiments.

Sample S5: W = 4.5 μm, S = 5.7 μm, h = 728 nm and d_p = 2.0 μm		**Sample S10**: W = 9.4 μm, S = 10.2 μm, H = 728 nm and d_p = 2.1 μm	
Case	***Droplet Volume - V* (μL)**	**Case**	***Droplet Volume - V* (μL)**

S5–1/2	0.5	S10–1	1
S5–1	1	S10–2	2
S5–2	2	S10–5/2	2.5
S5–3	3	S10–3	3
S5–5	5	S10–7/2	3.5

2.3 Results

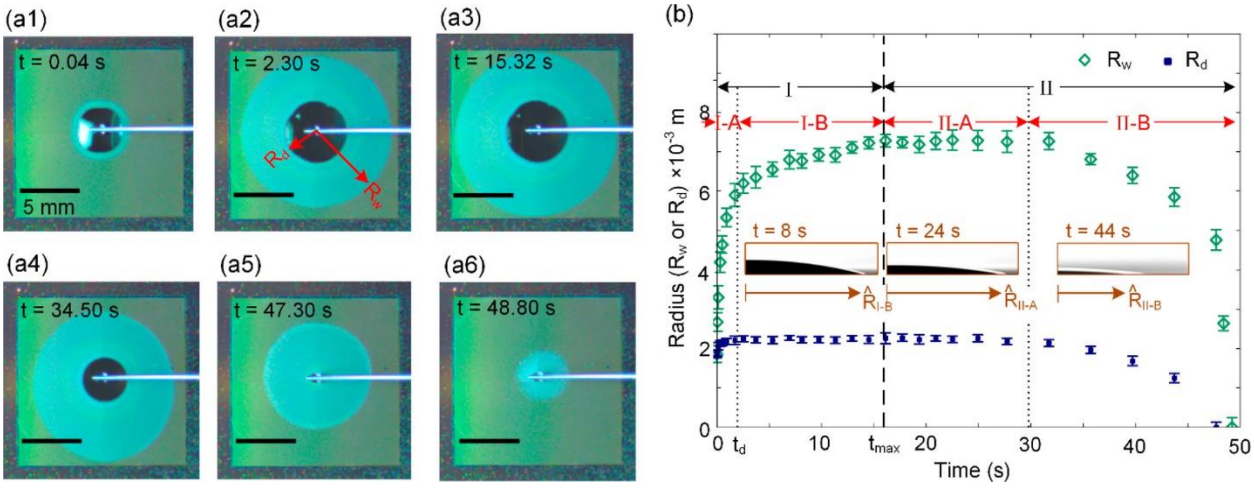

Figure 2.3 Droplet wicking on nanochannels sample (a) Sequence of high-speed camera images from top. (b) Evolution of droplet base radius and wicking radius with time along with goniometer images as insets. Reprinted with permission from Poudel, Zou, and Maroo [34]. Copyright (2019) American Chemical Society.

Figure 2.3 demonstrates an experimental observation of droplet wicking on a buried nanochannels sample [34]. The visualization and image processing technique were utilized to

achieve the comprehension of droplet spreading and wicking dynamics on nanochannels samples. Broady, the overall phenomenon is divided into wicking dominant regime (I) and evaporation dominant regime (II) as shown in Fig. 2.3 (b). As shown in Fig. 2.3, R_w initially rises and reaches its maximum value at the end of Regime-I. In Regime-II, evaporation of liquid from nanochannels a pores gets dominated thus the wicking front recedes back (i.e., R_w diminishes).

To supplement the experimental observation, we investigate the role of physical parameters like capillary pressure (P_{cap}) and viscous resistance (K_{vr}), in the dynamics of wicking flow in such nanochannels sample. Based on the thermodynamic definition of P_{cap} [42],

$$P_{cap} = \frac{\gamma r_f cos\theta_c [2*\{(W+S)^2 - W^2\} + 4WH]}{H((S+W)^2 - S^2)} \qquad \text{(Equation 2.1)}$$

Where γ is surface tension, r_f is the roughness factor $r_f \sim 1$ and θ_c is the intrinsic contact angle of a sessile droplet on bare SiO_2 sample $\theta_c \sim 26^o$.

Similarly, viscous resistance K_{vr} of wicking, flow can be deduced by solving Brinkman's equation [50] (a modified form of Navier-Stokes equation for a porous medium) where K_{vr} is equated to the ratio of dP/dx to u_{mean}.

$$K_{vr} = \frac{dP/dx}{u_{mean}} \qquad \text{(Equation 2.2)}$$

Finally, we obtain an analytical model for liquid propagation or wicking distance (w_d) inside cross-connected nanochannels as follows:

$$w_d = G\sqrt{t} \qquad \text{(Equation 2.3)}$$

Where, $G = \sqrt{\frac{2P_{cap}}{K_{vr}}}$ is the propagation coefficient [42].

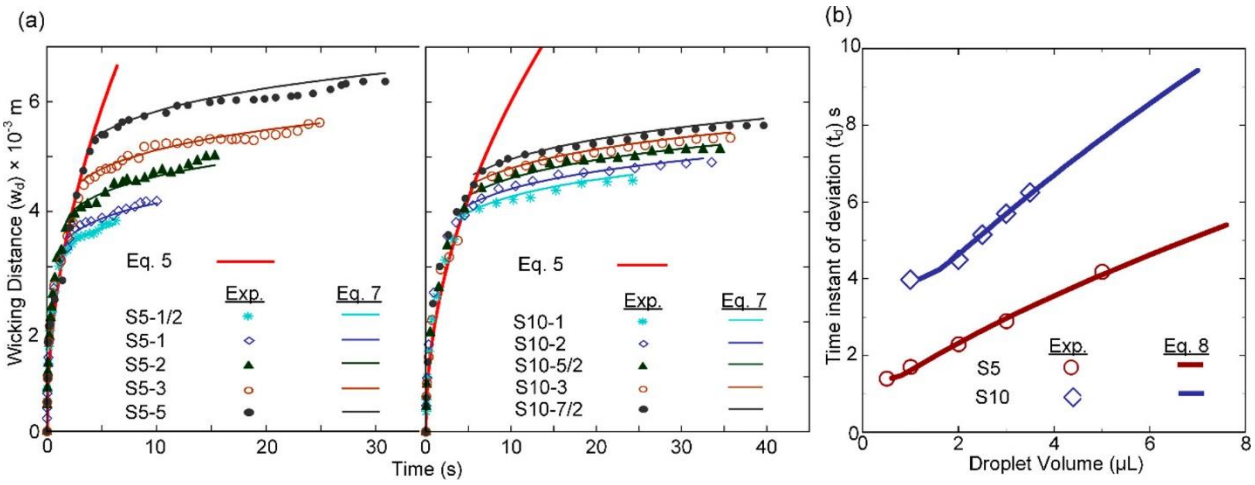

Figure 2.4 (a) Variation of wicking distance with time for S5 and S10 together with the prediction of analytical models for sub-regime I-A (Eq. 2.3) and I-B (Eq. 2.4). (b) Estimation of time instant of deviation for different droplet volumes for each nanochannels sample. Reprinted with permission from Poudel, Zou and Maroo [34]. Copyright (2019) American Chemical Society.

Based on the prediction of w_d from Eq. 2.3, the variation of the same is plotted for both nanochannels sample together with the w_d obtained experimentally for each case of droplet wicking in Fig. 2.4. The evolution of w_d with time as shown in Fig. 2.4, demonstrates that Eq. 2.3 predicts w_d only for the initial stage (sub-regime I-A) and the experimental observation deviates from the prediction of Eq. 2.3 later. It is inferred that the deduction of the wicking distance model for sub-regime I-A (see Eq. 2.3) is based on an infinite supply of liquid, however, the volume of the droplet is finite which implies the deviation of experimental results after some time. In order to model the later part of the wicking dominant regime, a semi-analytical model of droplet spreading based on the hydrodynamic dissipation approach developed by de Ruijter et al. [33] is utilized. Equation 2.4 shows the model for sub-regime I-B where 'K_{hyd}' and 'a' are fitting parameters and physically they signify the extent of dissipation and the radius of the core

region of the droplet spherical cap where radial expansion velocity is relatively negligible respectively [33].

$$w_d = K_{hyd}\left(\frac{2V}{\pi}\right)^{3/10}\left(\frac{15\gamma t}{\eta \ln(\frac{3V}{\pi a^3})}\right)^{1/10} \quad \text{(Equation 2.4)}$$

Thus, based on the above analysis for sub-regime I-A and I-B, we can develop a complete picture of wicking the dominant regime using the analytical model. The time instant at which the experimental behavior of droplet spreading deviates from one model to the other (denoted by t_d) is also plotted for different droplet volumes of each sample (see Fig. 2.4 (b)).

2.4 Summary

We fabricated cross-connected nanochannels of height ~728 nm, buried under a SiO_2 surface, with pores at each intersect to allow water to wick into the channels. Wicking in these nanochannels was studied by placing a water droplet on the top surface and recording the phenomena using a high speed camera. Various droplet volumes were used over two nanochannel samples differing in width/spacing for a total of ten experimental cases. Primary wicking parameters of wicking radius and droplet radius were analyzed over time to find that (1) they are linearly related and (2) wicking can be characterized by wicking-dominated and evaporation-dominated regimes. Each regime was further divided into two subregimes based on the evolution of wicking and droplet radii. The two wicking-dominated subregimes were explored using different analytical approaches to predict the evolution of wicking distance with time. Capillary pressure and viscous resistance were found to govern wicking in the first subregime based on good agreement between experimental results and derived analytical model. Due to the finite volume of the droplet, wicking deviates into the second subregime and is found to be governed by hydrodynamic dissipation within the droplet; this phenomenon is captured using a semi analytical model. Thus, we develop a mechanistic understanding on the evolution of

wicking in cross-connected buried nanochannels of height ~728 nm. Unlike the wicking dominant regime, the evaporation dominant regime cannot be modeled based on capillary pressure and viscous resistances. The local spatial and temporal variation of evaporation processes like evaporation flux rates, menisci curvature, liquid pressure gradient, etc. are dominant parameters in the evaporation dominant regime, which cannot be obtained from the analytical models alone. Thus, computational fluid dynamics (CFD) simulation of droplet wicking and evaporation on the nanochannels sample of consistent geometry is carried out to supplement the observation from experiments which is discussed in the next chapter.

Chapter 3: Evaporation Dynamics in Nanochannels & Micropores

3.1 Introduction

In this chapter, computational fluid dynamics (CFD) simulations are performed which supplement our experimental work to achieve a comprehensive understanding of evaporation and the dynamics associated with evaporation in the nanochannel sample. Although estimation of evaporation flux from the thin-film evaporation meniscus has been studied using numerical techniques previously, such analyses have involved a stationary (time-independent) meniscus. Furthermore, CFD simulation of droplet-coupled evaporation in uniform nano/micro structures has been lacking and is the focus of this work. Albeit this study is carried out at room temperature, the fundamental understanding attained through such CFD simulations can be extended to help design thermal management devices related to spray cooling, cooling tower heat exchangers and heat pipes.

3.2 Methods

A laminar multiphase model with a volume of fluids method is opted to simulate the droplet wicking and evaporation on the nanochannels sample by considering only one-fourth of the physical domain as shown in Fig. 3.1. Evaporation at the interface is evoked using a user-defined function, which is tailored to replicate the experimental observations. As shown in Fig. 3.1, the non-dimensional variation of R_w with non-dimensional time obtained from CFD illustrates an excellent agreement with the experimental results for sample S5. Thus, we use this numerical method to achieve a comprehensive understanding of the evaporation dominant regime of the droplet wicking phenomenon on nanochannels sample.

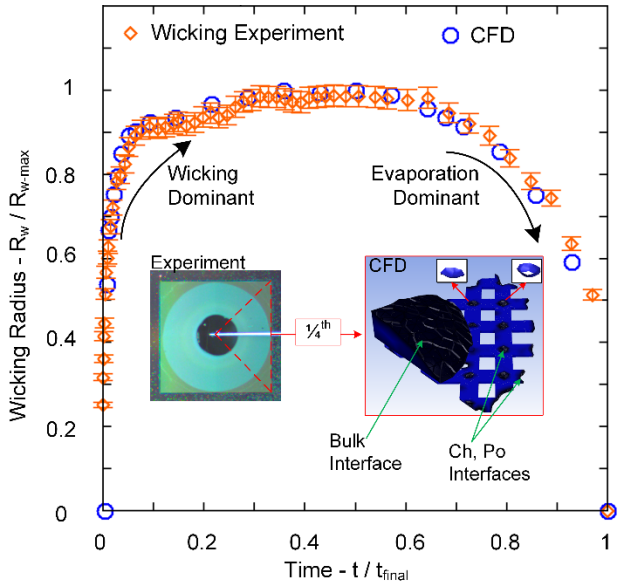

Figure 3.1 Variation of non-dimensional wicking radius with non-dimensional time illustrating the experimental and computational results. Reprinted with permission from Poudel, Zou, and Maroo [23]. Copyright (2020) American Chemical Society.

Table 3.1 Different cases of experiments and CFD simulation used to study evaporation dynamics in nanochannels with micropores

Sample – S5			**Sample – S10**		
Case	**Droplet Size**	**Method**	**Case**	**Droplet Size**	**Method**
S5-Exp	V = 2 μL	Exp.	S10-Exp	V = 2 μL	Exp.

Sample – S5			Sample – S10		
Case	**Droplet Size**	**Method**	**Case**	**Droplet Size**	**Method**
S5-CFD-All	H_c = 20 μm, R_c = 20 μm	CFD	S10-CFD-All	H_c = 20 μm, R_c = 20 μm	CFD
S5-CFD-Ch,Po		CFD	S10-CFD-Ch,Po		CFD

H_c and R_c are the initial droplet height and radius supplied in CFD simulation.

In order to evoke evaporation through a udf, we first locate all liquid-air interfaces in the computational domain thus inducing evaporation on all surfaces including the spherical cap surface above the nanochannels (see inset of Fig. 3.1); cases S5-CFD-All and S10-CFD-All correspond to this scenario. Later, we run the simulations where the udf is adjusted to locate the liquid−air interfaces only at the locations of nanochannels and micropores (see inset of Fig. 3.1), simulating evaporation only from these interfaces (cases S5-CFD-Ch,Po and S10-CFD-Ch,Po), that is, evaporation from the spherical cap does not occur. This allows us to evaluate the association of the evaporation existing at the menisci inside nanochannels and pores with the bulk liquid evaporation.

3.3 Results

From the experimental study of droplet wicking on nanochannels sample, it was recognized that studying wicking for only one particular droplet volume V is sufficient to capture the wicking behavior since the wicking characteristics in the normalized form for a given nanochannel geometry are independent of V. Thus, only one case of droplet volume for each sample is considered in CFD simulation. As shown in Table 3.1, we have two cases of CFD and only one case of an experiment for each nanochannels sample. To ease the computational burden, very reduced size of the domain with a smaller droplet is taken for CFD simulation as compared to the experiments. Later, the scaling effect arising because of the difference in magnitude of droplet size is eliminated by introducing a nondimensional time t^* defined as follows:

$$t^* = \frac{t - t_{no-sp}}{t_{final} - t_{no-sp}} \qquad \text{(Equation 3.1)}$$

Where t_{no-sp} is the instant at which the spherical cap completely wicks into the nanochannel (also shown in insets of Fig. 3.2) and t_{final} is the instant at which the liquid evaporates completely from the channels/pores. Thus, we set $t^* = 0$ as a reference when the water spherical cap completely wicks in, and water is only present in channels/pores irrespective of the experiment or CFD. Thus, the period of time $0 < t^* < 1$ constitutes the sheer phenomenon of micro/nanoscale thin-film evaporation at room temperature. Moreover, only in such a scenario ($t^* > 0$) can the mass of water (m) and the evaporation rate ($\dot{m}_e$) be experimentally determined.

$$m = \pi R_w^2 \rho H \varepsilon \qquad \text{(Equation 3.2)}$$

$$\dot{m}_e = \frac{\Delta m}{A_s \, \Delta t} \qquad \text{(Equation 3.3)}$$

where Δm is the instantaneous rate of change in mass (kg) of liquid inside the nanochannels sample in a very short duration of time Δt (s), A_s corresponds to the area of channels/pores with an evaporating meniscus at a particular instant, and is computed as:

$$A_s = \frac{\pi}{4} d_p^2 n + 2\pi R_w H \left(\frac{W}{S+W}\right) \qquad \text{(Equation 3.4)}$$

where, n is the number of pores filled with wicked-in water and exposed to the ambient, and ε is the porosity which equals 0.70 and 0.73 for S5 and S10 samples, respectively.

Similarly, for a case of CFD simulation, we calculate Δm at a time by first creating an isosurface (interface) within the computational domain where the volume fraction equals 0.5 (see inset of Fig. 3.2), followed by computing the mass flow through this isosurface in the region of channels/pores using Eqs. 3.2 – 3.3.

Table 3.2 Fitting parameters of evaporation rates for two different samples

Case	C_1	C_2	C_3	R^2 (%)	Average $\dot{m}_e$ during t* < 0 ($\times 10^{-3}$ kg/m^{2}s)		
					Curve-fit	CFD[†]	CFD[$]
S5	2.52×10^{-3}	10^{-3}	69.85	96	2.60	3.06	2.81
S10	1.81×10^{-3}	10^{-3}	115.05	92	1.90	1.96	1.84

[†]Evaporation at all liquid-air interfaces. [$]Evaporation at liquid-air interfaces restricted to nanochannels/micropores.

Figure 3.2 shows the results of $\dot{m}_e$ from CFD and experiments for the two samples S5 and S10, respectively. The non-dimensional form of evaporation flux obtained as $\dot{m}_e/\dot{m}_o$ where $\dot{m}_o$ = 1 kg/m^{2}s is considered to represent the variation of the data in order to have dimensional consistency with the logarithmic function used. A curve fit of asymptotic nature ($\dot{m}_e = C_1 + C_2.{C_3}^{t^*}$), as listed in Table 3.2, is generated from the experimental results of $\dot{m}_e$ which can predict the values of the same for $t^* < 0$. CFD results are found to be in good agreement with experimental results (for $t^* > 0$) as well as with the asymptotic curve fit (for all t^*) for both the

samples (Table 3.1). Further, the insets in Fig. 3.2 (a) shows the high-speed camera images for case S5-Exp at three different times; only one-quarter of the image of the actual nanochannels sample (see inset of Fig. 3.2) is shown.

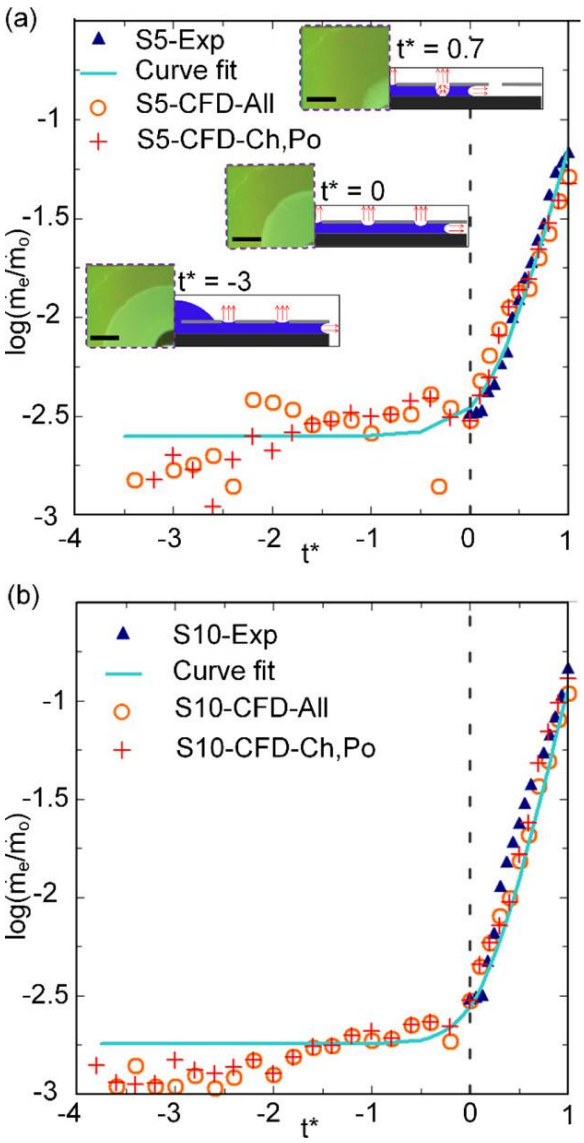

Figure 3.2 Variation of evaporation rate fluxes at nanochannels and micropores with non-dimensional time. Reprinted with permission from Poudel, Zou, and Maroo [23]. Copyright (2020) American Chemical Society.

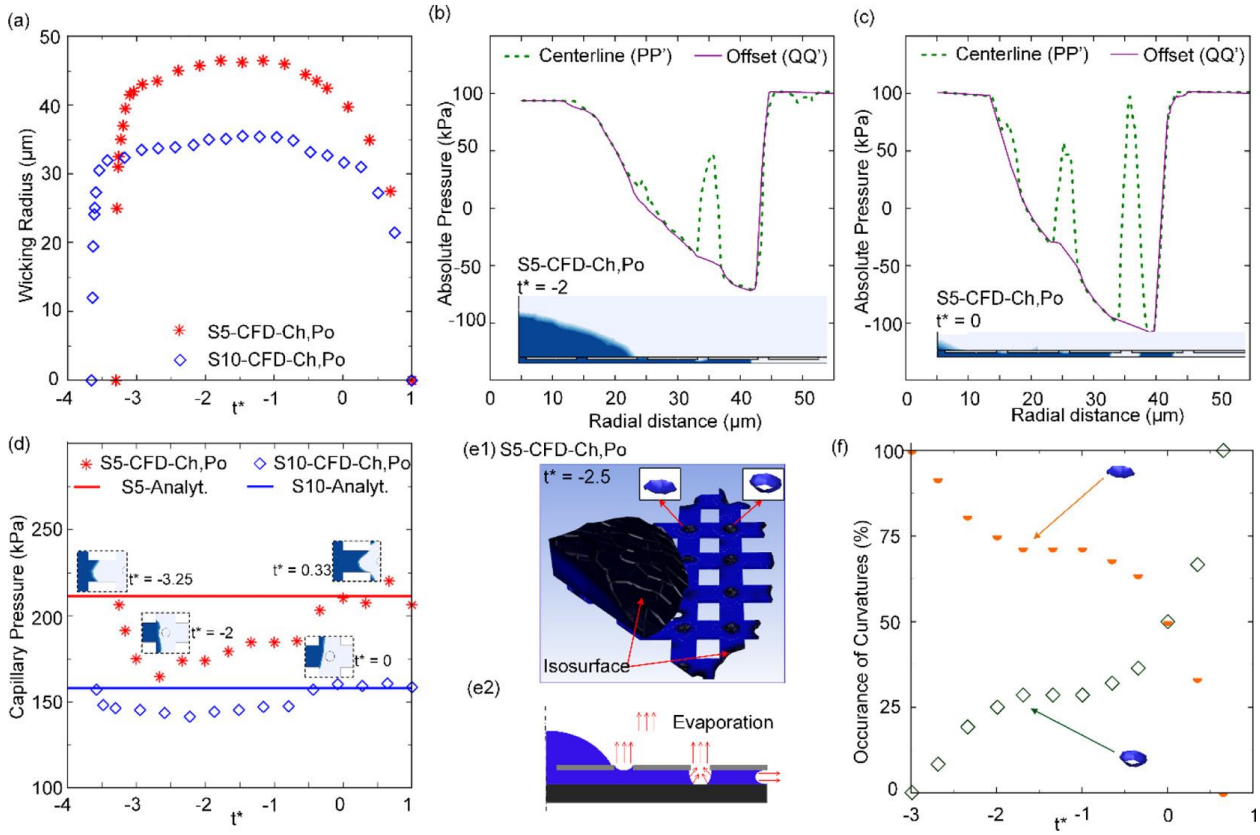

Figure 3.3 Evaporation dynamics on nanochannel sample. (a) Variation of R_w for two different samples. Variation of pressure along the length of nanochannel for S5-CFD-Ch,Po at (b) t = -2 and (c) t* = 0. (d) Comparison of P_{cap} obtained from CFD with the analytical value. (e) Cup and flared shaped evaporating menisci at micropores. (f) The occurrence of two kinds of curvatures with time. Reprinted with permission from Poudel, Zou, and Maroo [23]. Copyright (2020) American Chemical Society.*

Next, we utilize CFD to simulate two additional cases, S5-CFD-Ch,Po and S10-CFD-Ch,Po as listed in Table 3.2, where evaporation is restricted to occur only at the liquid-air interfaces of channels/pores and not from the water droplet. By doing so, although the time taken for complete evaporation of the equal quantity of liquid *V* is more than the earlier cases S5-CFD-All and S10-CFD-All, we can still plot the results of $\dot{m}_e/\dot{m}_o$ in Fig. 3.2 based on the non-dimensional time *t** (Eq. 3.1). The agreement of new plots (cases S5-CFD-Ch,Po and S10-CFD-Ch,Po) and values

(compared in Table 3.2) demonstrate that the nature of evaporation from the nanochannels/pores is independent of the evaporation at the spherical cap and that the evaporation flux rate is dominated by channels/pores.

Figure 3.3 (a) illustrates the evolution of wicking radius R_w with time for two different nanochannels geometry. As expected, S5 results in a greater wicking radius compared to S10, as the rate of wicking is directly related to the pressure gradient in the liquid. Figures 3.3 (b-c) show the pressure distribution at the mid-height of the nanochannels through the centerline and the offset at two different instants, t^*=–2 and t^*=0, for sample S5. Based on the spatial comparison with the volume-fraction contour plot (inset) at that same instance, each pressure distribution plot shows peak negative pressure at the radial distance corresponding to the liquid-air interface (meniscus) inside the nanochannels. In addition, there exist spikes in the pressure plot at PP' occurring at the location of pores as seen from the insets. These spikes are due to averaging of the negative pressure at the pore meniscus with the relatively higher positive air pressure and are dependent on the pore meniscus curvature and mesh grid size. The pressure distribution along offset (QQ') does not show such spikes as no pores are present along with this offset. In the later instant corresponding to the spherical cap completely wicking in and there is no further liquid supply to the nanochannels, the curvatures of the meniscus at pores get flared causing a local dry out directly underneath the pore as seen in the contour plot (inset) of Fig. 3.3 (c). The spike in the pressure in Fig. 3.3 (c) corresponding to such flared curvature of the meniscus is almost equal to the atmospheric pressure as a new contact line (i.e., dry region) forms underneath the pore. This also sheds light on the relative extent of spikes observed at the radial distances of ~25 μm and ~35 μm in Fig. 3.3 (c).

Moreover, the peak negative value of absolute pressure is related to the capillary pressure as $P_{cap} = P_{air} - P_{liquid}$. Thus, P_{cap} variation with t^* is also plotted for the two cases S5-CFD-Ch,Po and S10-CFD-Ch,Po (Fig. 3.3 (d)) along with the analytical value of capillary pressure calculated based on thermodynamic definition $P_{cap\text{-}td}$ [42] using Eq. 2.1.

Figure 3.3 (e1) shows wicking for case S5-CFD-Ch,Po at an instant t^* = -2.5 where the 3D cartesian contour plot is clipped at the isosurface. The isosurface in channels/pores region represents the liquid-air interfaces and associated curvatures. It is observed that the curvature at pores is of two basic types, one cup-shaped and the other flared (bell-shaped) as observed from the magnified versions in insets of Fig. 3.3 (e1) and sketch in Fig. 3.3 (e2). For case S5-CFD-Ch,Po, a plot of prevalence of these two kinds of curvatures along with t^* is shown in Fig. 3.3 (f). It is revealed that, during the latter time stage of wicking, flared curvatures are dominant which clearly explains the following: (i) spikes in pressure plot through centerline (Figs. 3.3 (b-c)) and (ii) new contact line regions underneath the pores cause the observed increase [51, 52] of mi_e for times $t^* > 0$ in Fig. 3.2.

3.4 Summary

We conducted CFD simulations and experiments of wicking-coupled evaporation in cross-connected buried nanochannels of height ~728 nm with ~2 μm diameter micropores at each intersection. Two different samples of nanochannel widths ~5 μm and ~10 μm were studied. The experimental study of water droplet spreading in the porous structure provided results on the evolution of the wicking radius and droplet base radius with time. Concentrating on the evaporation dominant regime of the wicking phenomenon, evaporation flux in channels/pores is estimated from both experiment and CFD and found to be in good agreement. CFD simulations demonstrated that evaporation of water wicked in channels/pores is independent of evaporation

of the bulk water droplet sitting above the channels. When the meniscus recedes, new contact line regions form underneath the pores causing the observed increase in evaporation flux. Wicking flux velocity, pressure distribution inside nanochannels, and curvature motion associated with wicking were also independently computed, from which the variation of viscous resistance with time is estimated. Viscous resistance is found to initially increase with time before achieving a steady value, thus implying that it is directly related to the driving force. Hence, this work articulates a wider perspective of wicking by estimating local spatial and temporal parameters which govern the phenomenon. Through CFD simulations supplemented by experiments, we are able to comprehend the lesser understood parameters, such as evaporation flux, wicking flux velocity, and pressure distribution, in wicking of water in submicron porous nano/microstructures, with potential design applications in heat pipes and spray cooling technologies.

Chapter 4: Thin-film Evaporation

4.1 Introduction

Thin film evaporation manifests itself in nearly all evaporation processes [1, 2, 4, 53-55], and surfaces are designed to amplify its occurrence to achieve high heat flux removal [1, 2, 4]. For example, over the past few years, micro/nano structures have been fabricated on surfaces to passively wick the liquid and augment thin film meniscus area, thus enhancing heat transfer. [1, 2, 4, 23, 56, 57] The way in which liquid is supplied to such structured surfaces give rise to two distinct scenarios, first where the surface is partially submerged in a pool of bulk liquid thus providing unlimited supply of liquid to the structures [46, 58], and second where liquid supply to the structured surface is limited [59] but recurs at regular intervals. An example of the latter is spray cooling [53, 60, 61] where micro/macro sized droplets are dispersed, at a desired frequency, on a heated surface where the droplets wick into the structures creating thin film regions. Unlike the first scenario, such droplet coupled thin-film evaporation present unique challenges in heat transfer characterization and is the focus of this work. In the experimental study of droplet evaporation on micro/nano structures, challenges arise due to the dynamic and transient nature of the interaction between the thin-film menisci present within the structures with the continuously changing droplet's interfacial curvature as well as decreasing droplet volume. Consequently, the experimental investigation of the droplet evaporation phenomenon on a heated surface has been studied sparsely [62-64]. An experimental study on droplet evaporation on nanoporous alumina substrate suggested nanostructuring as a tool for enhancing evaporation rates [35]. Following that, Carey et al. investigated the mechanism of droplet impinging and thin-film formation on the nanostructured surface [65]. Nevertheless, to optimize the micro/nano structures and liquid supply design as well as to maximize heat flux removal, an estimation of

heat flux at the surface as well as in micro/nano scale menisci, along with dry out limits are important. Such in-depth and complete fundamental knowledge is limited in literature [18, 22, 23], and can advance not only thermal management solutions like spray cooling and drop-wise cooling [41] but also manufacturing related technologies such as thin-film coating [66], nano-fabrication [67], and ink-jet printing [40].

Here, we report an experimental investigation of wicking and evaporation of deionized (DI) water droplet in porous nanochannels at varying surface temperatures up to 90°C. The well-defined geometry of micropores and nanochannels help estimate the sample's porosity precisely ($\varepsilon = 0.70$) enabling us to determine the heat flux at these length scales. The outcome of evaporation rate from experiments is coupled with ideal spray conditions to predict surface heat fluxes which can potentially be removed via spray cooling. We also illustrate a way to maximize heat flux dissipation in spray cooling by optimum utilization of space in the porous nanochannels.

4.2 Methods

The porous nanochannel sample comprises of cross-connected buried nanochannels of height H ~ 728 nm with a micropore of diameter d_p ~ 2 µm present at each interconnection (Figs. 4.1A-B). The channel width W ~ 4.5 µm and spacing S ~ 5.7 µm, along with H and d_p, are indicated in the isometric view of 2×2 unit cells of the sample shown in Fig. 4.1 B. With the height in sub-micron scale, the geometry is 1D nanochannel. Details of the steps of nanofabrication as well as characterization by atomic force microscopy are available in Chapter 2 as well as in the published articles [23, 68]. The micropores allow liquid from a droplet to wick into the nanochannels while the interconnected channels enable liquid exchange (a sketch with a droplet on top and simultaneous wicking is shown in Fig. 4.1A). Such a buried (enclosed) geometry of

channels boosts the capillary pressure for superior wicking than many other open structures like nanoporous layers or nanostructured surfaces, etc. Figure 4.1C illustrates a vertical cross-section of the heated sample with a wicked in droplet, menisci in channels and pores from where thin-film evaporation occurs, and evaporation from droplet interface. Figure 4.1D shows the top view of a droplet on the surface wicking into the fabricated sample of size 1.4 cm × 1.4 cm. A zoomed-in view of pores and channels is captured in Fig. 4.1E-1 while a goniometer image of droplet contact angle is shown in Fig. 4.1E-2. Further, Figs. 4.1F-1 and F-2 show a 3-D AFM image of the fabricated sample and the corresponding wall profile, respectively.

In the experimental setup, the fabricated sample is bonded atop a copper rod which has embedded cartridge heaters and is enclosed in a Teflon shell; thus, the copper rod heats the bottom surface of the sample. The temperature *T* of the bottom surface of sample is maintained by using a PID controller while the sessile droplet of DI water is generated using a syringe pump. A high-speed camera is mounted overhead the arrangement to visualize wicking from the top while a side camera at an inclination of 12^{o} is used to monitor the temporal variation of the amount of liquid sitting on the top. The two cameras are synchronized based on the instant when the droplet touched the surface, and the maximum error in synchronization is estimated to be 0.053 s based on the frame rates. Additional details of the experimental setup, repeatability of the experiments, and precision of measurement techniques are provided in the Appendix A2. Experiments are carried out with droplets of varying volume from 4 µl to 10 µl at surface temperatures varying from 35^{o}C to 90^{o}C as listed in Table 4.1 (for e.g., C50-4 corresponds to the Case with surface temperature 50^{o}C and droplet volume 4 µl). The droplet is placed on the porous nanochannels after the surface temperature achieved a steady state. The maximum surface temperature is limited to 90^{o}C in order to avoid boiling in the droplet bulk liquid.

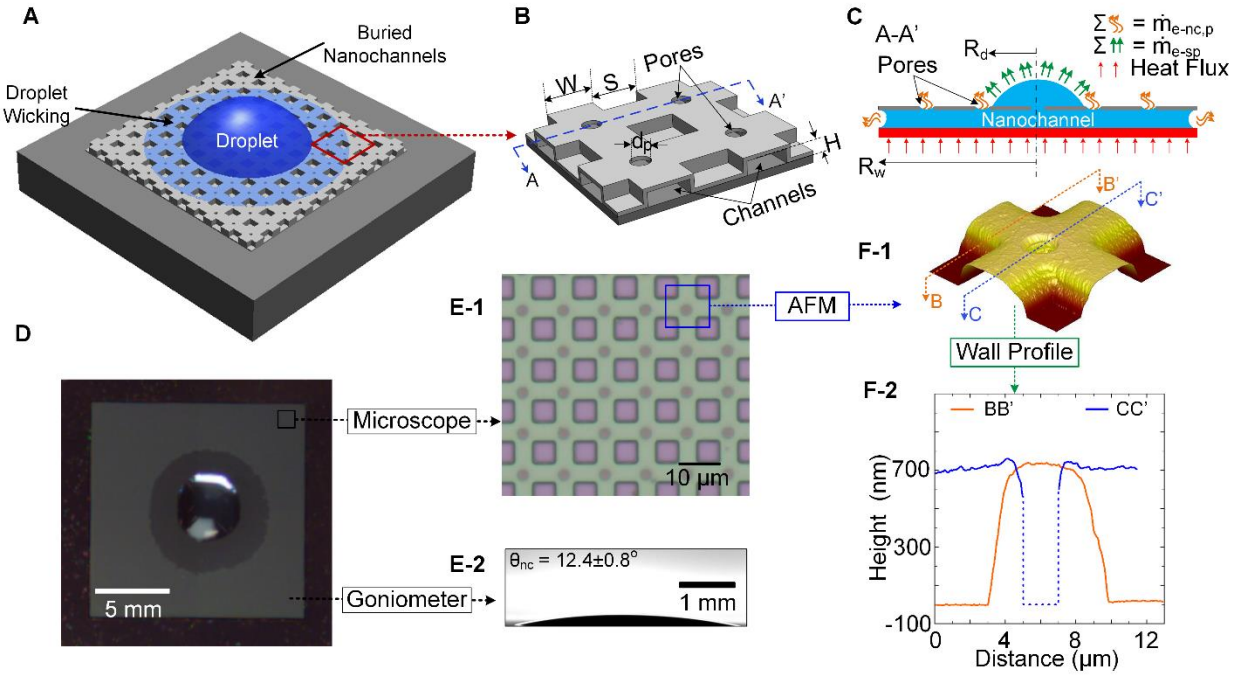

Figure 4.1 Porous nanochannels sample with channel height of 728 nm and 2 µm pores. (A) Sketch of a droplet spreading and wicking into the porous nanochannels sample. (B) Isometric view of a 2×2 unit cells showing geometrical details. (C) A cross-section sketch depicting the wicking parameters and evaporation sites. (D) A high-speed camera experimental image from the top with a water droplet sitting on the sample and water wicking in the nanochannels. (E1) Top-view of the fabricated sample showing the channels and pores as observed under an optical microscope. (E2) Contact angle of the water droplet on the sample surface. (F) AFM image of a unit cell of the sample along with height profile. Reprinted with permission from Poudel et al. [69] ACS (2020).

Table 4.1 Different cases of wicking experiments conducted based on surface temperature and droplet volume.

Case	**Temp. *T***	**Droplet Vol. *V***		**Case**	**Temp. *T***	**Droplet Vol. *V***
C35-4	35 ºC	4 µl		C75-4	75 ºC	4 µl
C35-6		6 µl		C75-6		6 µl
C35-8		8 µl		C75-8		8 µl
C35-10		10 µl		C75-10		10 µl
C50-4	50 ºC	4 µl		C90-4	90 ºC	4 µl
C50-6		6 µl		C90-6		6 µl
C50-8		8 µl		C90-8		8 µl
C50-10		10 µl		C90-10		10 µl

3. Results and Discussion

With the understanding that the dynamics of wicking at elevated temperatures will be different from the phenomenon at room temperature, we perform the droplet wicking experiments on the porous nanochannels sample at the aforementioned surface temperatures. We first study the characteristics of the liquid droplet wicking and explore the role of capillary pressure P_{cap} and viscous resistance K_{vr} on wicking dynamics at those temperatures. Figures 4.2A-B show the high-speed camera images acquired during droplet spread and simultaneous wicking in the sample for cases C50-8 and C90-8 respectively.

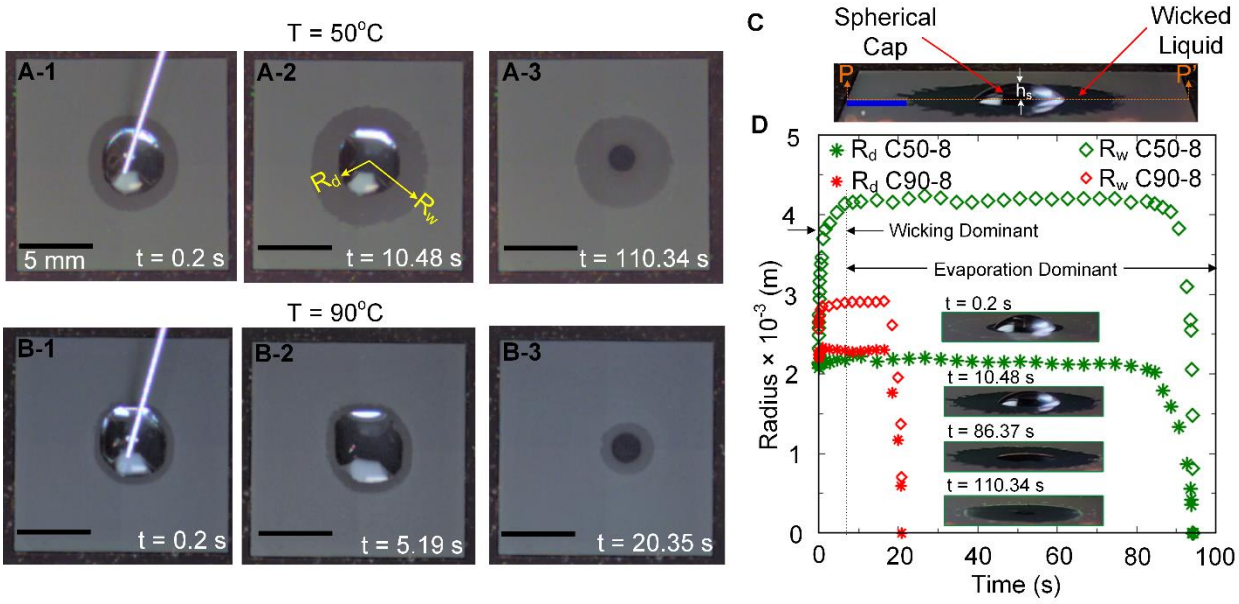

Figure 4.2. Water droplet spreading and simultaneous wicking into nanochannels. High speed camera images showing the top view of the sample at surface temperature T of (A) 50°C and (B) 90°C. (C) Side camera view of droplet wicking for case C50-8 with scale bar (2.5 mm) at the vertical plane passing through line P-P'. (D) Time evolution of wicking radius R_w and droplet base radius R_d for the two temperature cases along with inset images for case C50-8 from the side camera. Wicking dominant and evaporation dominant regimes are shown for case C50-8. Reprinted with permission from Poudel et al. [69] ACS (2020)

The effect of temperature on the wicking distance is clear from the series of images. An image from the side camera is also shown for the instant t = 10.48 s for case C50-8 in Fig. 4.2C. From these images, the time evolution of the wicking radius R_w, droplet base radius R_d and wicking distance $w_d = R_w - R_d$ as well as the height of the spherical cap sitting on the top h_s is acquired. Figure 4.2D plots the evolution of R_w and R_d with time for the two temperature cases (additionally, insets show images from the side camera for case C50-8). It is observed that both R_w and R_d increase quickly to their corresponding maximum values during the initial stage; this

is the wicking dominant regime (Fig. 4.2D) where liquid propagation inside the nanochannels is governed by capillary and viscous forces [68]. Afterwards, the wicking front remains nearly steady as apparent from the plateau of data points in Fig. 4.2D; during this equilibrium phase, the evaporation rate at the menisci balances the liquid wicking rate into the channels and is termed evaporation dominant regime. All through this regime, the droplet's spherical cap base radius R_d remains steady while the droplet height h_s as well as droplet's spherical cap volume gradually decrease (apparent from the insets in Fig. 4.2D) as liquid wicks into the channels.

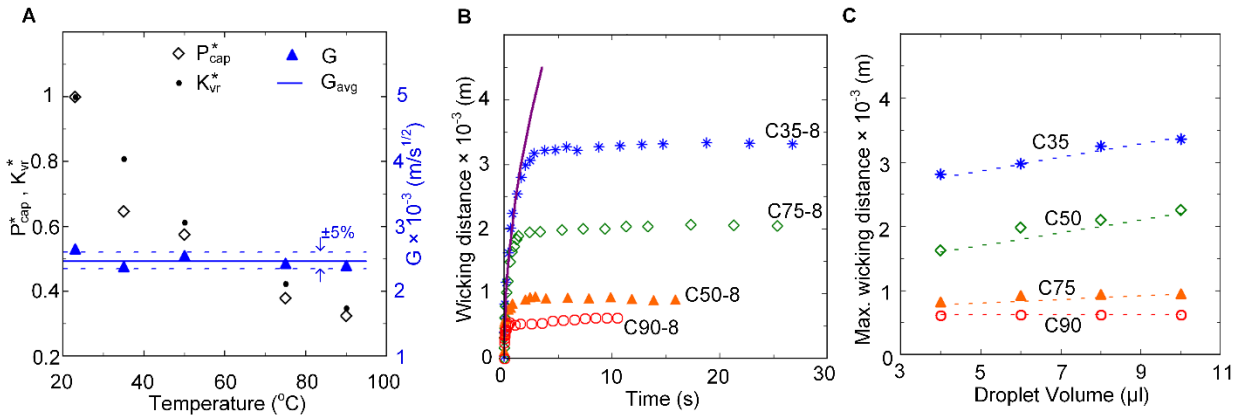

Figure 4.3 Wicking characteristics of the porous nanochannels at different surface temperatures. (A) Variation of non-dimensional capillary pressure and viscous resistance, and corresponding propagation coefficient, of wicking flow inside the nanochannels in the wicking dominant regime. (B) Evolution of wicking distance in nanochannels with time. (C) Maximum wicking distance relative to droplet volume; slopes of the dotted lines (linear curve fits) are 0.11, 0.095, 0.026 and 0.0002 for C35, C50, C75, and C90 cases respectively. Reprinted with permission from Poudel et al. [69] ACS (2020)

When the droplet completely wicks in, evaporation causes the wicking front to recede as seen with the decrease in R_w. Clearly, the overall dynamics of R_w and R_d is dependent on the surface

temperature of the sample, and the results of experiments performed in the present work can provide quantitative data on droplet evaporation needed for analyzing the high temperature applications like spray cooling. Hence, by using the data represented in Fig. 4.2, we quantify the evaporating menisci in micropores/nanochannels through the measurement of R_w and R_d, and compute the total rate of evaporation from the temporal variation of spherical cap volume (obtained from R_d and h_s) as explained next.

The well-defined geometry of our sample is used to determine the capillary pressure P_{cap}, viscous resistance K_{vr} and wicking distance w_d in the wicking dominant regime at different surface temperatures using the following equations: [42, 68]

$$P_{cap} = \frac{\gamma r_f cos\theta_c [2*\{(W+S)^2 - W^2\} + 4WH]}{H((S+W)^2 - S^2)} \quad \text{(Equation 4.1)}$$

$$K_{vr} = \frac{dP/dx}{u_{mean}} \quad \text{(Equation 4.2)}$$

$$w_d = G\sqrt{t} \quad \text{(Equation 4.3)}$$

where γ is surface tension, r_f is roughness factor of nanochannels wall (r_f ~ 1 from AMF images), θ_c is the intrinsic contact angle of DI water on Si substrate, W, H and S are nanochannels width, height, and spacing as explained earlier, and $G = \sqrt{2P_{cap}/K_{vr}}$ is the propagation coefficient. [42] Details on derivation of the equations as well as dependency of the parameters on temperature are available in Appendix A1.

Figure 4.3A shows the variation of non-dimensional P_{cap}^* and K_{vr}^* with temperature in the wicking dominant regime. The non-dimensional parameters are obtained by dividing with the corresponding values at room temperature (23°C) obtained from our prior work [68] i.e. $P_{cap}^* =$

$P_{cap}/P_{cap\_23^oC}$. In the scenario where, the parameters P_{cap} and K_{vr} have only been studied at room temperature [34, 42], here we report the variation of P_{cap} and K_{vr} with temperature, which in turn, provides an interesting outcome in terms of propagation coefficient G. As shown in Fig. 3A, both P_{cap}^* and K_{vr}^* decay with increase in temperature which interestingly results in a nearly constant value of propagation coefficient G, thus implying that the variation of wicking distance w_d with time (Eq. 4.3) is constant regardless of temperature and droplet volume in this regime. An average value of the propagation coefficient, G_{avg}, for the entire temperature range is computed. The finding is also confirmed in Fig. 4.3B which plots data for 8 µl volume droplet against a single w_d curve using constant G_{avg} value. This key outcome, that the initial wicking in nanochannels is independent of temperature and droplet volume, holds significant importance for high temperature applications such as pool boiling [46, 58, 70] and spray cooling [53, 60].

Beyond the initial wicking dominant phase, the variation of wicking distance with time deviates from the one predicted by Eq. 3 due to evaporation coupled with limited liquid supply from the droplet spherical cap. [68] Higher surface temperatures cause early divergence of w_d from the prediction of Eq. 3 (Fig. 4.3B). Since G_{avg} only predicts the variation of wicking distance with time in the initial regime, the maximum extent (w_{d-max}) of liquid penetration into the nanochannels would be dependent on droplet volume and evaporation rate (thus the surface temperature). Thus, w_{d-max} occurs when the wicking rate of liquid balances the evaporation rate at the menisci. Figure 4.3C plots the variation of w_{d-max} against droplet volume V for different surface temperatures. The dotted lines represent the linear curve-fit of the data points for each temperature. The slopes of the dotted lines suggest that, with increasing surface temperature, the impact of droplet volume on maximum wicking distance significantly decreases, with the slope being ~0 for surface temperature of 90°C implying $w_{d\text{-}max}$ does not depend on droplet volume at

that temperature (Fig. 4.3C). Such an observation is again important for designing surfaces for high temperature applications.

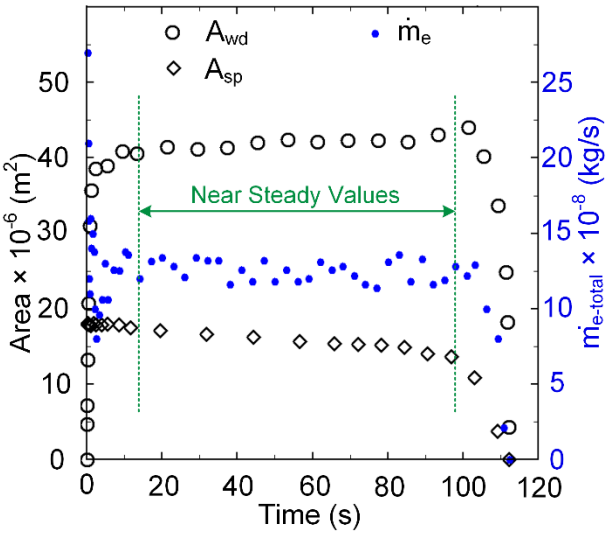

Figure 4.4 Temporal variation of wicked surface area A_{wd}, spherical cap area A_{sp} along with the estimated total rate of evaporation $\dot{m}_{e-total}$ during droplet wicking and evaporation for case C50-8. Reprinted with permission from Poudel et al. [69] ACS (2020)

Next, we focus on estimating the thin-film evaporation rate occurring in the nanochannels and micropores (see Fig. 4.1C), along with its potential application in spray cooling. Three associated parameters are identified and determined from experimental data: wicked surface area A_{wd} which only includes the area where liquid-filled micropores are exposed to ambient, droplet spherical cap surface area A_{sp}, and the total rate of evaporation $\dot{m}_{e-total}$ which is the combined evaporation rate from the menisci in nanochannels/micropores and from the droplet spherical cap interface (Fig. 4.1C). The temporal variation of these parameters is obtained from the data acquired from the images of the high speed camera and side camera using the following relations:

$$A_{wd} = \pi(R_w^2 - R_d^2) \quad \text{(Equation 4.4)}$$

$$A_{sp} = \pi(R_d^2 + h_s^2) \quad \text{(Equation 4.5)}$$

$$V_{sp} = \frac{1}{6}\pi h_s(3R_d^2 + h_s^2) \quad \text{(Equation 4.6)}$$

$$\dot{m}_{e-total} = \frac{\Delta V_{sp}\rho}{\Delta t} \quad \text{(Equation 4.7)}$$

The temporal evolution of the three parameters A_{wd}, A_{sp} and $\dot{m}_{e-total}$ is shown for case C50-8 in Fig. 4.4. Area A_{wd} increases quickly to attain a steady value with a stable wicking front within a few seconds. Area A_{sp} although decreases gradually due to wicking following evaporation, it can be assumed near steady in the limit 14 s < t < 98 s. Steady contact line above the nanochannels (static R_d) but slowly diminishing height of the spherical cap h_s as observed in Fig. 4.2 is the reason behind this near steady value of A_{sp} in this range. Interestingly, $\dot{m}_{e-total}$ also turns out to be steady within the same time range. Thus, the three parameters have near steady values in majority of the evaporation dominant regime; similar observation is made for each experimental case. Correspondingly, average values of A_{wd}, A_{sp} and $\dot{m}_{e-total}$ are determined within their near steady range for each case, and plotted in Figs. 4.5A-C, respectively. These three parameters are interconnected because the total rate of evaporation $\dot{m}_{e-total}$ comprises of the evaporation from the nanochannels/pores (directly related to A_{wd}) and the evaporation from the bulk liquid surface (spherical cap area A_{sp}).

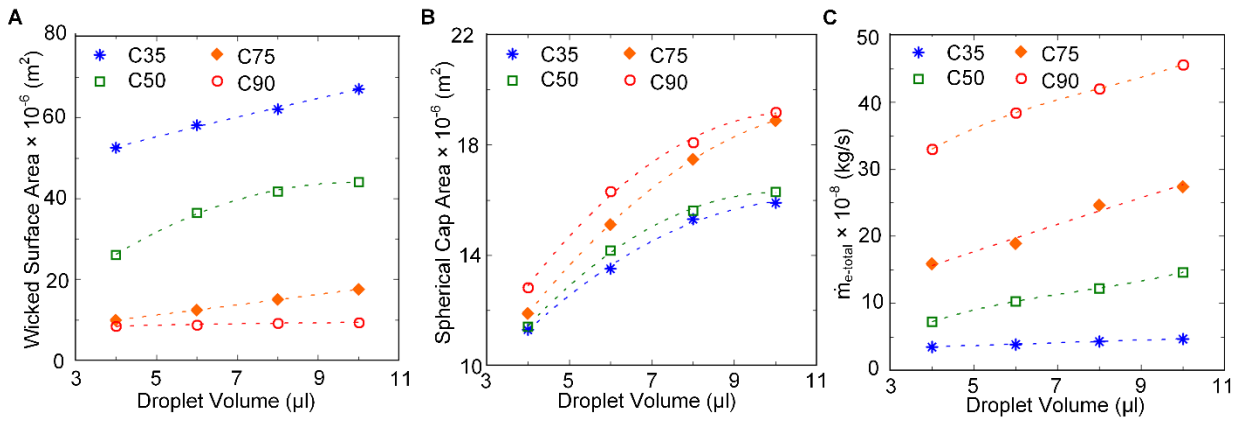

Figure 4.5 Variation of (A) wicked surface area A_{wd}, (B) spherical cap area A_{sp}, and (C) total evaporation rate variation relative to droplet volume during evaporation dominant regime for different surface temperatures. Dotted lines serve as guide for eyes. Reprinted with permission from Poudel et al. [69] ACS (2020)

In order to only determine evaporation flux ($\dot{m}''_{e-nc,p}$) from channels/pores where thin-film menisci are present, we first decouple it from the droplet spherical cap evaporation flux ($\dot{m}''_{e-sp}$) by expressing $\dot{m}_{e-total}$ as:

$$\dot{m}_{e-total} = A_{sp} * \dot{m}''_{e-sp} + (A_{nc} + A_p) * \dot{m}''_{e-nc,p} \qquad \text{(Equation 4.8)}$$

where, A_{nc} $(= 2\pi R_w H * k_{nc})$ is the projected area of the curvatures inside nanochannels (i.e wicking front), and A_p $(= A_{wd} * k_p)$ is the projected area of the curvatures at micropores. The constants k_{nc} and k_p are based on geometry of cross connected nanochannels and micropores with values ~0.5 and ~0.0314, respectively. For a surface temperature case, Equation 4.8 has two unknowns, $\dot{m}''_{e-sp}$ and $\dot{m}''_{e-nc,p}$, which can be solved with four sets of experimental data corresponding to the four droplet volume experiments performed at that temperature. Values of $\dot{m}''_{e-sp}$ and $\dot{m}''_{e-nc,p}$, for each temperature, are calculated within a small range of error (<5%).

Although, Eq. 4.8 is based on the assumption of linearity with A_{wd} and A_{sp}, we confirm this assumption as well the flux values through an additional and independent set of experiments as explained next.

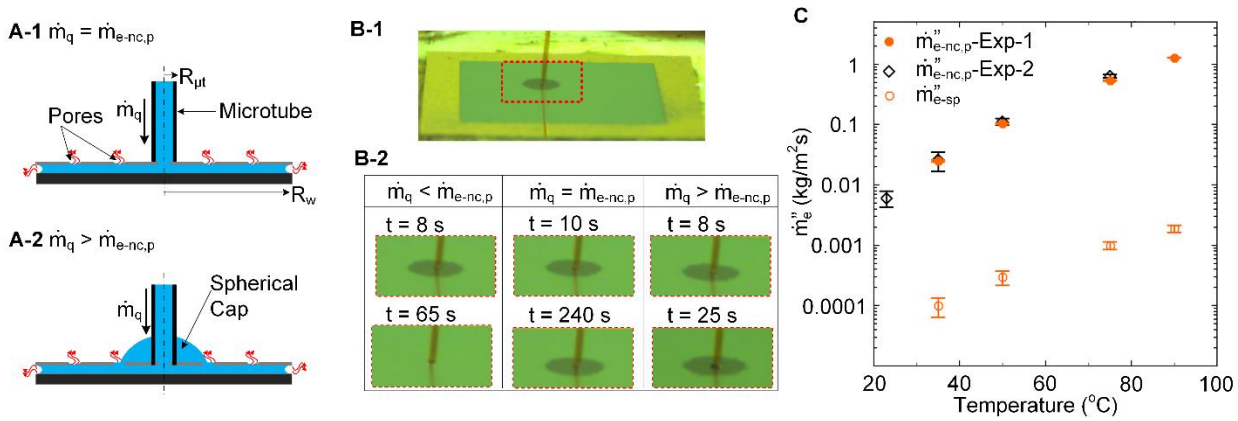

Figure 4.6 Direct experimental measurement of thin-film evaporation flux from nanochannels and micropores using continuous liquid supply. (A) Sketch to demonstrate the comparison between the flow rate of the pump $\dot{m}_q$ and the evaporation rate from nanochannels which result in the state of (A-1) equilibrium ($\dot{m}_q = \dot{m}_{e-nc,p}$) or (A-2) liquid accumulation above nanochannels ($\dot{m}_q > \dot{m}_{e-nc,p}$). (B-1) Side view of wicking and evaporation in porous nanochannels sample due to liquid supply through microtube. (B-2) Three different instances in incremental steps of $\dot{m}_q$ during the experiment on nanochannels sample at 35°C demonstrating dry out for $\dot{m}_q < \dot{m}_{e-nc,p}$, stable wicking front for $\dot{m}_q = \dot{m}_{e-nc,p}$ and liquid accumulation on top for $\dot{m}_q > \dot{m}_{e-nc,p}$. (C) Variation of thin-film evaporation flux with surface temperature from nanochannels/micropores and droplet spherical cap. Reprinted with permission from Poudel et al. [69] ACS (2020)

We performed a new set of experiments to directly measure the evaporation rate $\dot{m}_{e-nc,p}$ of thin-film menisci in nanochannels/micropores at same surface temperatures as before. We aim to

acquire a steady-state wicking front in the heated sample such that the evaporation rate $\dot{m}_{e-nc,p}$ is balanced by the water feed rate $\dot{m}_q$ to the sample through a microtube, i.e., $\dot{m}_q = \dot{m}_{e-nc,p}$ (Fig. 4.6A-1). If $\dot{m}_q > \dot{m}_{e-nc,p}$, liquid would accumulate on top of the channels (Fig. 4.6A-2) causing additional evaporation from the accumulated bulk liquid which would introduce error in $\dot{m}_{e-nc,p}$ measurement. Thus, in the experiments, flow of DI water through the microtube and onto the sample is controlled by an automatic-pump and tailored such that accumulation of bulk liquid atop the surface is avoided (Fig. 4.6B-1). Such a delicate flow balance is achieved by gradually increasing the liquid flow rate $\dot{m}_q$ of the pump in small steps starting from $\dot{m}_q$ = 0 kg/s (= 0 µl/min). Figure 4.6B-2 shows three different instances of gradual increment of $\dot{m}_q$, for the surface temperature of 35°C. At small flow rate of $\dot{m}_q$ (first column of Fig. 4.6B-2), wicking is initially observed but the wicked liquid dries out over time as the liquid flow rate is lower than the rate of evaporation i.e., $\dot{m}_q < \dot{m}_{e-nc,p}$. With increase in flow rate $\dot{m}_q$, we obtain a stable wicking front when the evaporated liquid from the nanochannels sample is exactly balanced by the liquid supplied through the microtube ($\dot{m}_q = \dot{m}_{e-nc,p}$) as seen in the second column. Further increment in $\dot{m}_q$ ($> \dot{m}_{e-nc,p}$) results in an undesirable accumulation of liquid on top of the channels as seen in the third column. After repeating similar set of experiments for all temperatures, we achieve the steady state thin-film evaporation rate $\dot{m}_{e-nc,p}$ from the menisci in the nanochannels and micropores.

Considering the projected area of menisci inside nanochannels and micropores during evaporation, we obtain the evaporation rate flux $\dot{m}''_{e-nc,p}$ as follows:

$$\hat{A}_{wd} = \pi\left(\hat{R}_w^2 - \hat{R}_{\mu t}^2\right) \qquad \text{(Equation 4.9)}$$

$$\dot{m}''_{e-nc,p} = \frac{\dot{m}_{e-nc,p}}{\hat{A}_p + \hat{A}_{nc}} = \frac{\dot{m}_{e-nc,p}}{\hat{A}_{wd} * k_p + 2\pi \hat{R}_w H * k_{nc}}$$ (Equation 4.10)

where, $\hat{R}_w$ and $\hat{R}_{\mu t}$ are the radii of wicked liquid and microtube respectively (Figure 4.6A-1). The variation of $\dot{m}''_{e-nc,p}$ with temperature obtained from these set of experiments is plotted in Figure 4.6C (labelled as $\dot{m}''_{e-nc,p}$-*Exp-2*). Figure 4.6C also shows the evaporation flux (labelled as $\dot{m}''_{e-nc,p}$-*Exp-1*) obtained through droplet wicking experiments as discussed earlier i.e., the values of $\dot{m}''_{e-nc,p}$ and $\dot{m}''_{e-sp}$ obtained by solving Eq. 4.8. As can be seen, the values of $\dot{m}''_{e-nc,p}$ obtained from the two independent experiments are in excellent agreement. The droplet experiments also allow us to estimate evaporation flux from the droplet interface $\dot{m}''_{e-sp}$ (Fig. 6C) and we find it to be about two orders of magnitude smaller than $\dot{m}''_{e-nc,p}$. Thus, thin-film evaporation and its augmentation is highly desired in droplet based thermal management solutions such as spray cooling.

Next, we demonstrate the potential of using our porous nanochannel design in spray cooling to achieve high heat flux dissipation. Using the experimentally measured evaporation flux rate $\dot{m}''_{e-nc,p}$, we calculate the heat flux in the nanochannels and micropores using the relation:

$$\dot{q}''_{nc,p} = \dot{m}''_{e-nc,p} * h_{fg}$$ (Equation 4.11)

where h_{fg} is the latent heat of evaporation at the corresponding surface temperature.

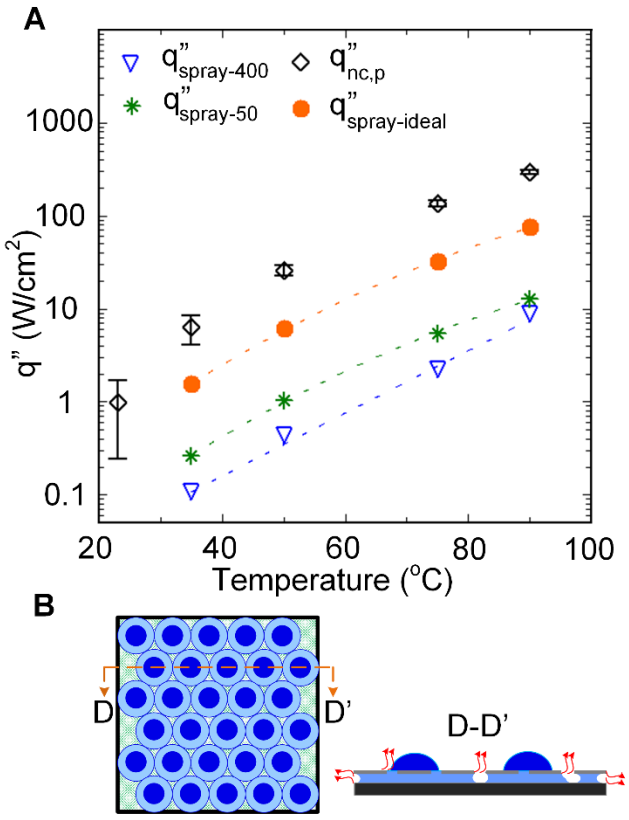

Figure 4.7 Potential use of porous nanochannels in spray cooling thermal management for high heat flux dissipation (A) Variation of heat flux with surface temperature based on the projected area of thin-film menisci present in channels/pores from evaporation experiments, along with the cooling performance (based on projected area of the sample) using different spray parameters. (B) A sketch demonstrating fcc distribution of droplets and corresponding wicking in nanochannels to achieve high heat flux dissipation. Reprinted with permission from Poudel et al. [69] ACS (2020)

The obtained variation of heat flux in channels/pores is plotted against temperature in Fig. 4.7A. Heat flux as high as ~294 W/cm^2 at surface temperature of 90°C is achieved through thin-film evaporation. In order to extend the present fundamental work to a relevant practical application of thermal management, we examine the performance of idealized spray cooling on the

fabricated porous nanochannels sample and estimate maximum possible heat flux removal rates. As shown in Fig. 4.7B, we consider an ideal face-centered-cubic (fcc) distribution of the wicked surface area of sprayed droplets atop the heated sample. Two cases are investigated where different spray-generated droplet diameters of 400 µm and 20 µm (represented as spray-400 and spray-20, respectively), based on available literature and practical feasibility [61, 71], are assumed to be deposited on the sample. From the volume of the individual droplet of spray V_{d-s} and the contact angle of the liquid on the nanochannels sample θ_{nc}, its corresponding spherical cap base radius R_{d-s} is evaluated and the corresponding wicking radius R_{w-s} is estimated from the existing results of the wicking test (see Appendix A2). Such an analysis helps estimate the maximum number of spray droplets sitting in fcc arrays on our sample (see Fig. 4.7B). Using the droplet distribution, the projected area of menisci in micropores and nanochannels is obtained from which the spray cooling performance $\dot{q}_s^{"}$ (heat flux removal based on the projected area of the sample) for each set of spray at the corresponding temperature is calculated:

$$\dot{q}_s^{"} = \frac{\dot{q}^{"} * (A_{p-s} + A_{nc-s})}{A_{sample}} = \frac{\dot{q}^{"} * n_d (\pi (R_{w-s}^2 - R_{d-s}^2) * k_p + 2\pi R_{w-s} H * k_{nc} * k_{nc})}{A_{sample}} \quad \text{(Equation 4.12)}$$

where, n_d is the number of droplets in the array obtained sitting atop the channels based on fcc distribution and a sample size of 1.4 cm × 1.4 cm (A_{sample} = 1.96 cm^2). For the two sprays, spray-400 and spray-20, the values for n_d are found to be in a wide range of 15-96 and 6,000-380,000 respectively (see Appendix A2) at different temperatures. Figure 4.7A shows the estimated heat flux removal for the two sprays $\dot{q}_{spray-400}^{"}$ and $\dot{q}_{spray-20}^{"}$; high heat flux dissipation of ~12.80 W/cm^2 can ideally be attained.

Additionally, in Fig. 4.7A, we observe that the extent of heat flux removal increases significantly (Y-axis being logarithmic), with a smaller droplet size of spray. Also, we know from the wicking test at high temperature, the proportion of the spherical cap volume from the total droplet volume decreases for smaller droplet volume (see Appendix A2). Thus, we can estimate a critical limit of droplet volume for wicking in nanochannels such that, the proportion of the spherical cap is zero (i.e., no spherical cap) and the entire liquid is wicked in. This critical limit is achieved when the droplet has a diameter ~4.5 μm. Hence, we again perform a similar spray cooling analysis but with an ideal spray of uniformly generated droplet diameters of ~4.5 μm. The variation of heat flux removal achieved through this ideal spray is also plotted in Fig. 4.7A. The heat flux dissipation can be significantly increased to ~77 W/cm^2 at substrate temperature of 90^{o}C with such small droplet diameters. It is noteworthy to mention here that for the identical nanochannels sample, we had reported pool boiling heat flux based on the projected area to be ~20 W/cm^2 at a surface temperature of 117^{o}C, and critical heat flux ~178 W/cm^2 at a surface temperature of ~140^{o}C. [46] Additionally, proper liquid supply design (e.g., injecting liquid or use of multiple spray nozzles) in our porous nanochannel surfaces can enable higher heat flux dissipation. With the prescribed flow rate, the forced convection of spray droplets can enhance the heat flux removal capacity to a level similar to that achieved in pool boiling heat transfer while avoiding the complexity of a boiling setup and operating in non-boiling regime of phase change heat transfer. This foregoing analysis highlights the thermal management potential of using thin-film evaporation in such structured surfaces via spray cooling.

4.4 Summary

A well-defined porous geometry of cross-connected nanochannels with micropores was fabricated and heated to study droplet coupled thin-film evaporation. A droplet placed on the

surface wicks into the channels through the pores and enables tracking of the evaporating menisci through time-resolved visualization. For various surface temperatures ranging from 35^{o}C – 90^{o}C and varying droplet volumes from 4 µl to 10 µl, wicking characteristics and evaporation rate were determined. It was found that initial wicking (i.e., in wicking dominant regime) in the nanochannels was independent of surface temperature and droplet volume. In the later stage of droplet wicking, i.e., evaporation dominant regime, the maximum wicking distance does not depend on droplet volume at high surface temperatures. Evaporation flux from channels/pores, where the thin-film menisci are present, was found to be about two orders of magnitude higher than from the droplet interface, and corresponding heat flux as high as ~294 W/cm^2 was obtained from the channels/pores. Applying the experimental findings of heat transfer and wicking characteristics towards potential use of spray cooling based thermal management, high heat flux dissipation ~ 77 W/cm^2 can ideally be attained from thin-film evaporation in the porous nanochannels. Additional enhancements in cooling performance can be achieved by further optimizing the nanochannels/micropores geometry.

Chapter 5: Thermal Management of Photovoltaics

5.1 Introduction

Being a renewable source, solar energy is extensively utilized through a variety of conversion approaches including photoelectricity, solar thermal system, photosynthesis based solar fuel, biomass, etc. [72] Of these, the photoelectrical conversion process is ought to be more advantageous regarding the ease of transmission and utilization, however achieving high efficiency in the very method is the most provocative aspect of the process. Unlike the solar thermal conversion process, which can be up to 60% efficient, the solar cell utilizes only a narrow range of wavelength (visible light) resulting to a typical conversion efficiency of < 20% in practical PV panels [72] (or up to 35% in certain special circumstances [73, 74]). This adds a further challenge in reducing the gap that exists between the solar energy potential and the extent of utilization [72]. In order to enhance the performance of a PV panel, several methods have been accomplished including reducing the optical losses [75, 76], employing a concentrated PV system [77, 78], minimizing the internal resistances of the solar cell [79, 80], applying post-processing techniques [81-83], using organic semiconductor [84-86] and low bandgap materials [87, 88], etc. Besides, cooling of the PV panel is projected to be the best alternative especially while considering the establishment of the PV plants in tropical zones with elevated ambient temperature [89-91], which unsurprisingly implies overheating of the PV panels.

When the solar radiation is incident on the solar cells in a photovoltaic (PV) module, only a small part of the absorbed energy is transformed into electrical power while a significant part raises the internal energy of the underlying material. The rise in internal energy generates heat, which reduces the overall efficiency of the photoelectric conversion process [92, 93] as well as diminishes the operating life [94] of the PV panel. The conversion efficiency of a solar cell can

vary widely with 3 – 20 % of the incident solar radiation transformed into electrical power [72, 95]. Based on the efficiency, a huge portion of the inbound energy gets dissipated in the form of heat and can raise the PV panel temperature up to 75^{o}C [96]. Several studies have highlighted overheating as the major hindrance to achieving a high conversion efficiency in a PV panel [92, 96-99]. Additionally, findings have reported the decline in the conversion efficiency by 0.5% - 0.7% per 1^{o}C rise in the temperature [96, 100] which further indicate a pressing need for an efficient cooling mechanism to regulate the PV panel temperature. Moreover, the temperature regulation of the PV surface potentially prevents any mechanical failure of the solar cell material due to thermal stresses as well [97]. Finally, the outcome of the applied cooling in the PV panel in terms of the solar cell performance acts cumulatively to the other methods [101-103], which further emphasizes the significance of exploring the PV cooling system. Cooling mechanisms can also be made financially viable by tuning the coolant supply [104, 105] or utilizing a passive flow [106, 107].

Several studies [98, 106, 108] have shown efficient cooling of the PV panel through an air-cooling system demonstrating a lesser need of energy to circulate the air coolant than liquid. However, a higher extent of cooling can be achieved with water cooling [97, 104, 107, 109] especially methods employing phase change [110-112] that removes a very large amount of latent heat. [109] employed water channels at the back face of the PV panel to continuously circulate liquid coolant. Similarly, jet impingement on the PV panel was introduced, which was capable to reduce the PV surface temperature from 69.7^{o}C to 36.6^{o}C [113]. With an aim to reduce the consumption of coolant, a periodic cycle of cooling by switching the sprinklers on/off was applied, which reported an enhancement in the annual energy production by 12% [104]. Additionally, a system of pulsed-spray cooling also showed an effective enhancement of 27% in

the electrical power output by consuming only 1/9th of the coolant that would be used in a steady supply [105]. In order to achieve higher cooling proficiency by exploiting latent heat, various phase change materials have also been utilized to regulate the PV panel temperature demonstrating an average cooling of 20 – 30^{o}C [99, 114]. Furthermore, a passive dissipation of heat through thin-film evaporation was achieved by using layers of synthetic clay [110] as well as cotton wick structures [111] on the back face of the PV panel ultimately enhancing the electrical power output by 19% and 14% respectively. Unlike the active supply of coolant, the passive flow of liquid by employing wick structures [110, 111] or heat pipes [115, 116], etc. do not need supplemental power to drive the flow of coolant. While the power consumed to drive the coolant in an active cooling system can consume a substantial portion of the generated electricity and reducing the enhancement in the electrical power by ~50% [117, 118], passive cooling system eliminates the burden to drive such external flow. With this understanding, the passive supply of liquid and heat flux dissipation through phase change are recognized as two key criteria for an efficient PV cooling system. In line with that, a device with micro/nano scale structures that can (1) continuously supply required liquid coolant through wicking [34, 119, 120] and (2) simultaneously allow a high heat removal rate at the evaporating menisci [23, 121, 122] is anticipated as the best candidate to offer a promising solution to the overheating issue of the PV panel. Accordingly, we utilize the porous nanochannels device [123] which has demonstrated excellent wicking characteristic [23, 34] as well as high heat flux dissipation through nanoscale thin-film evaporation [123], and numerically integrate it on the back face of a commercial PV panel to evaluate the extent of cooling. The cross-connected geometry of the buried nanochannels (height = 728 nm) offer a potential solution for high rate of wicking while the micropores (diameter = 2.1 μm) provided at each intersection host the sites for evaporating

menisci [34, 46, 123]. Hence, the findings of the heat flux removal attained in such porous nanochannels device [123] is utilized as a technique of thermal management and the numerical investigation of PV cooling employing energy balance model [124] is reported in this chapter.

5.2 Methods

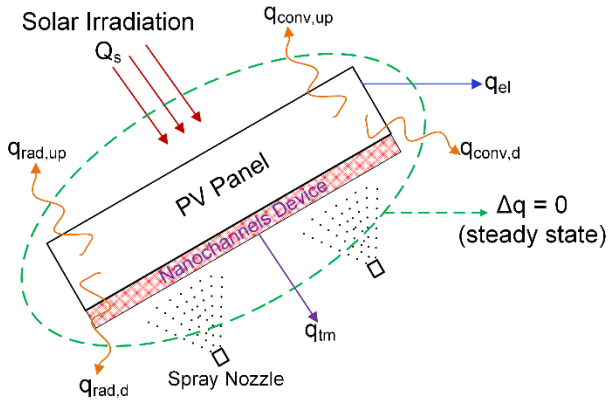

Figure 5.1 Schematic of a PV panel with nanochannels device attached on the back face illustrating the associated quantities of heat and energy transfer. Reprinted with permission from Poudel et al. [125] arXiv (2021).

The energy balance model [124] is utilized to numerically solve the governing equations of energy and heat transfer in order to determine the temperature distribution over the surface of the PV panel. When the incoming solar radiation flux (Q_s) is incident on the PV panel (Fig. 5.1), a part of it will cause the rise in internal energy of the PV panel material while some portion would be lost to the ambient via convection (q_{conv}) and radiation (q_{rad}) heat transfer per unit area. A fraction of the incoming radiation flux is converted into electrical power per unit area (q_{el}). Accordingly, the energy balance model is expressed as shown in Eq. 5.1.

$$q_s - q_{el} - q_{conv} - q_{rad} - q_{tm} = \rho C_p \delta \frac{dT_s}{dt} \qquad \text{Equation 5.1}$$

where, each term has the unit of W/m^2, $q_s = \varepsilon_o Q_s$, $\varepsilon_o = 0.9$ is the PV surface absorptivity δ is the thickness of PV panel, and q_{el} is the electrical power output from the PV panel per unit area which is dependent on the conversion efficiency of the PV panel (β) and is the function of the surface temperature T_s [115, 124]:

$$q_{el} = \beta Q_s = (21.737 - 0.1757 T_s) Q_s \quad \text{Equation 5.2}$$

q_{conv} is calculated as the sum of convection heat transfer at the front and back face of the PV panel:

$$q_{conv} = q_{conv,up} + q_{conv,d} \sim 2 q_{conv,up} = 2h(T_s - T_a) \quad \text{Equation 5.3}$$

where, T_s is the average surface temperature of the PV panel and T_a is the ambient temperature (T_a= 18^{o}C), h is the convection heat transfer coefficient, which is the function of wind speed (u_w) as $h = 2.8 + 3.8 u_w$ and $u_w = 2$ m/s [115, 124].

Similarly,

$$q_{rad} = q_{rad,up} + q_{rad,d} \cong 2 q_{rad,up} = 2\varepsilon_l \sigma (T_s^4 - T_a^4) \quad \text{Equation 5.4}$$

where, ε_l represents the emissivity of the PV panel surface (ε_l~ 0.7) [115, 124]

q_{tm} is the heat flux removal achieved through thermal management, which is obtained by employing the porous nanochannels device [123] (henceforth denoted as nanochannels). The nanochannels utilized in the present study offer a passive dissipation of high heat flux through thin-film evaporation of the spray droplets dispersed over it, thus eliminates the need of a continuous supply of coolant. This further prevents the loss of energy in driving the active flow and simplifies the analysis relating the economic viability of the energy management system.

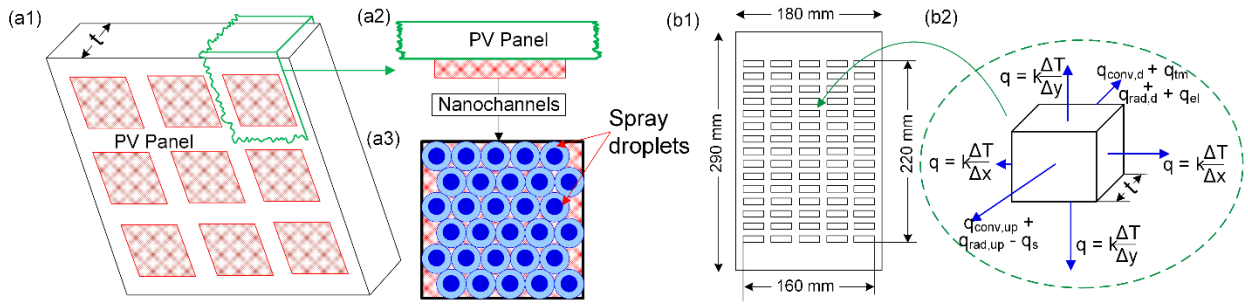

Figure 5.2 Detail of PV cooling system with nanochannels. (a1-a2) Integration of nanochannels devices on the back face of the PV Panel. (a3) Spray droplets dispersed over the nanochannels device. [123] (b1) The commercial PV panel utilized in present study. [115] (b2) A unit control volume in the discretized domain of the PV panel illustrating the associated transport quantities. Reprinted with permission from Poudel et al. [125] arXiv (2021).

In order to provide a suitable thermal management, the nanochannels are integrated on the back face of the PV panel to dissipate heat from the material of the PV panel. In order to achieve uniformity in the surface temperature, several such nanochannels are attached to the PV panel (see Fig. 5.2-a1), on top of which, the dispersed spray droplets wick and evaporate passively (see Figs. 5.2 a2-a3). Moreover, the number and distribution of the nanochannels device attached to the PV panel can be varied to tune the required extent of cooling. Figure 5.2-b1 shows the geometry of a commercial PV panel (size of 180 mm × 290 mm and thickness of 5.45 mm) employed for the numerical study in the present work. The PV panel having the monocrystalline silicon solar cells with same geometry has been utilized in several other studies [115, 124, 126]. Information about the material, fabrication and performance of the solar cells in this PV panel is adapted from literature [115, 124].

Next, to solve the energy balance equation (Eq. 5.1), the domain of the PV panel (Fig. 5.2-b1) is discretized into a finite number (N) of control volumes. For each control volume, the energy

balance equation (Eq. 5.1) is deduced with an additional term to account for the conduction heat transfer (q_{cond}) along the length and width of the PV panel as illustrated in Eq. 5.5. Fig. 5.2-b2 demonstrates all transport quantities associated with a typical inner control volume. For the control volume at the edge of the PV panel, boundary condition applied specified is convection + radiation. Additionally, the initial temperature of the entire domain is set as uniform and equal to the ambient temperature (T_a = 18 ^{o}C) and the properties of the PV panel material is assumed to be independent of temperature in the operating range.

$$q_s - q_{el} - q_{conv} - q_{cond} - q_{rad} - q_{tm} = \rho C_p \delta \frac{dT_s}{dt} \qquad \text{Equation 5.5}$$

By solving the transient state energy balance equation (Eq. 5.5), the surface temperature at the center of each control volume of the discretized domain is achieved through numerical iterations. The temperature distribution is further used to characterize the average surface temperature of the PV panel (T_s) at corresponding time instant (t). Initially, by varying the number of control volumes, multiple cases of numerical simulation with Q_s = 1,000 W/m^2 is studied and the evolution of T_s with time is compared to investigate the grid-sensitivity. From the grid sensitivity test, a grid with 200×400 (N = 80,000) control volumes is identified as the optimum one, which is then employed for all subsequent cases.

5.3 Results and Discussion:

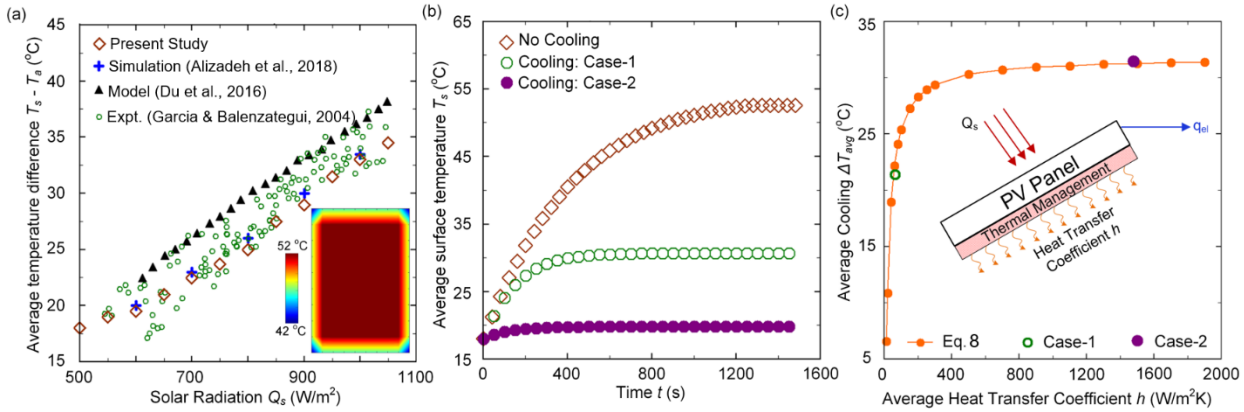

Figure 5.3 Thermal state of the reference PV panel at varying conditions. (a) Variation of the difference in average surface temperature and ambient temperature with solar radiation. The inset shows the steady state temperature distribution over the PV panel with Q_s = 1,000 W/m^2. (b) Temporal rise in average surface temperature of the PV panel for the cases of cooling and no cooling. (c) Variation of the average cooling achieved with the heat transfer coefficient for a generic thermal management. Reprinted with permission from Poudel et al. [125] arXiv (2021).

Initially, the energy balance equation (Eq. 5.5) is solved for the temperature distribution on the PV panel by varying Q_s = 500 W/m^2 to 1,050 W/m^2 and without any thermal management ($q_{tm} = 0$). As the PV panel temperature reaches a steady state, the difference in average temperature of the PV panel surface (T_s) and the ambient temperature (T_a) is obtained for each case of solar radiation and plotted in Fig. 5.3a. The inset in Fig. 5.3a also depicts the steady state temperature distribution over the PV panel surface corresponding to T_s = 1,000 W/m^2 at t = 1,500 s. The obtained variation of the average temperature difference ($T_s - T_a$) with the incident solar radiation shows an excellent agreement with the results of experiment [126] as well as numerical simulation [115] and analytical model [124] on the consistent PV panel as shown.

Thus, the plot in Fig. 5.3a establishes the accuracy and reliability of the numerical methods implemented in the present study.

When the specified solar radiation is incident to the PV panel, temperature of the PV panel surface (T_s) escalates from initial 18°C due to the rise in internal energy of the PV material. The surface temperature ultimately approaches a steady state in a certain duration of time designated as response time. Response time (R_t) is demarcated as the time duration at which the PV panel surface temperature reaches 99% of the final steady state temperature [124] due to the combined effect of gain in internal energy (owing to incoming radiation) and loss in heat (due to thermal management). Accordingly, Fig. 5.3b shows the temporal evolution of T_s corresponding to Q_s = 1,000 W/m^2 with the final steady state temperature of the PV panel being ~51.5°C with R_t ~ 1,500 s.

Next, the heat flux dissipation due to the employed nanochannels is introduced for the thermal management of the PV panel. The performance of the nanochannels in two different cases of spray cooling corresponding to the uniform spray droplets diameter 400 μm and 20 μm (denoted by Case-1 and Case-2 respectively) achieved earlier [123] is utilized here. The amount of heat flux removal during such process is found to be dependent on the surface temperature; Accordingly, following two expression for the heat flux as a function of T_s is deduced from the past work [123]:

$$\log_{10}(q_{tm}) = 0.03369T_s - 2.143 \qquad \text{Equation 5.6}$$

$$\log_{10}(q_{tm}) = 0.03036T_s - 1.577 \qquad \text{Equation 5.7}$$

The nanochannels are incorporated to the entire surface of the back face of the reference PV panel such that maximum and uniform heat flux dissipation is possible. When this applied

thermal management (q_{tm}) is introduced to the energy balance equation (Eq. 5.5), the surface temperature of the PV panel reduces. The variation of T_s with time for the two cases of cooling (dictated by Eqs. 5.6 and 5.7) with Q_s = 1,000 W/m^2 is also shown in Fig. 5.3b. The plot demonstrates the final steady state temperature to be to 30.5^{o}C and 20^{o}C for Case 1 and 2 respectively as compared to 51.5^{o}C for the case without any cooling. In addition, as compared to R_t ~ 1,500 s for no cooling case, the system with cooling, cases-1 and 2 reach the steady state of operation much sooner with R_t ~ 500 s and ~ 200 s respectively. It is essential to have a shorter R_t as the incoming radiation varies throughout the day and the thermal hysteresis are not trivial. A shorter response time achieved with the implemented thermal management further signifies the impact of the results reported here.

Next, we utilize the energy balance equation (Eq. 5.5) to compute the PV surface temperature distribution by considering a case of thermal management with specified heat transfer coefficient (h_{tm}). While the investigation of PV cooling by employing nanochannels provide the extent of cooling accomplished through corresponding removal of heat flux (Eqs. 5.6 & 5.7), the consideration of h_{tm} can provide an estimate of the cooling for a broader range of heat transfer concerning generic applications. The implication of thermal management with specified h_{tm} on PV cooling is crucial to comprehend the potential cooling performance of widespread techniques including phase change material, nanofluids, wickless heat pipes, etc. [127]. In order to resolve this, numerical study of PV cooling for a range of h_{tm} = 1 – 2,000 W/m^{2}K is performed by characterizing q_{tm} as:

$$q_{tm} = h_{tm}(T_s - T_a) \qquad \text{Equation 5.8}$$

Figure 5.3c shows the variation of the average cooling achieved with the heat transfer coefficient. Here, the extent of cooling achieved is characterized by average cooling (ΔT_{avg}) such that $\Delta T_{avg} = T_{s-wo} - T_{s-w}$, where T_{s-w} and T_{s-wo} are the steady state average surface temperature of the PV panel with and without thermal management respectively. This plot signifies a wide-ranging implication and can be utilized to estimate the average cooling of the PV panel obtained via a generic thermal management device of known heat transfer coefficient (h). Furthermore, the plot in Fig. 5.3c exhibits a unique nature of variation with h_{tm}; the initial rise in h_{tm} shows a steep increment in ΔT_{avg} but ultimately approaches its maximum limit. In such, a system will attain the maximum extent of cooling where a further increment in h_{tm} doesn't enhance ΔT_{avg} anymore, hence inferring an upper limit of the extent of the PV panel cooling. This is an exciting result obtained in regard that it predicts the theoretical limit of the PV panel cooling which is possible to establish only by characterizing q_{tm} in terms of h_{tm} in Eq. 5.5. Additionally, considering the steady state operation of the two cases of the PV panel cooling corresponding to Q_s = 1,000 W/m^2 (see. Fig. 5.3b), we back calculate the heat transfer coefficient from (Eqs. 5.6, 5.7) as $h_{tm} = q_{tm}/(T_s - T_a)$. The average cooling versus h_{tm} for these two cases are also presented in the same plot Fig. 5.3c. Clearly, the finer spray droplets in Case-2 provides a higher heat flux dissipating ability (Eq. 5.7) and exhibits a greater extent of PV panel cooling approaching the theoretical limit. Overall, Fig. 5.3c provides a universal standard to estimate PV cooling for a generic thermal management device and indicates the cooling ability of the employed nanochannels.

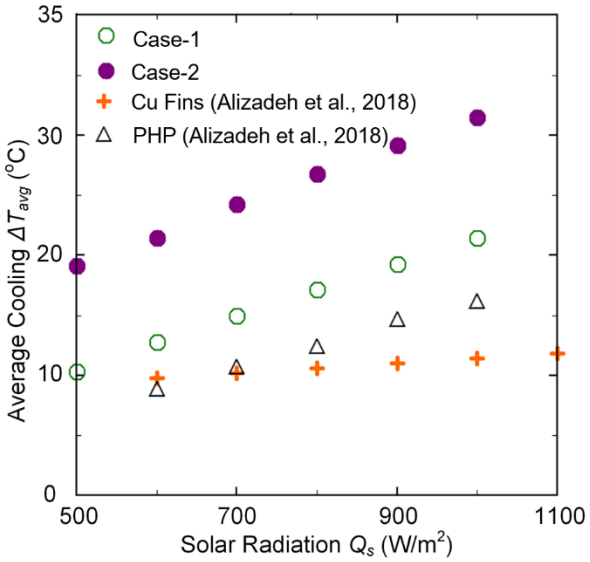

Figure 5.4 Variation of average cooling of the PV panel with incident solar radiation. Reprinted with permission from Poudel et al. [125] arXiv (2021).

Figures 5.3b-c provide the results of PV cooling for a constant value of solar radiation (Q_s = 1,000 W/m^2). However, in a realistic scenario, the intensity of solar radiation fluctuates with weather and is time dependent. Thus, it necessitates the investigation of the average cooling ΔT_{avg} for a varying range of Q_s. Considering the solar radiation variation Q_s = 500 W/m^2 to 1,000 W/m^2 with step of 100 W/m^2, the thermal management with nanochannels (Cases 1 and 2) is employed over again to solve Eq. 5.5 numerically. Figure 5.4 shows the variation of average cooling accomplished with the incident solar radiation. A significant extent of cooling of the PV panel using the nanochannels in the present study is achieved throughout the range of solar radiation considered. Moreover, Fig. 5.4 also demonstrates the superior cooling with the present method as compared to the past work of PV cooling achieved through Cu Fins and pulsating heat pipe (PHP) [115] on the same PV panel. Such an improvement in the present work is possible due to thin-film evaporation based phase-change heat transfer occurring in the porous nanochannels device [123]. Further, the enhancement in Case-2 as compared to Case-1 also

aligns well with the finding in terms of the heat transfer coefficient (see Fig. 5.3c) thus reiterating the significance of the reported technique of PV panel cooling.

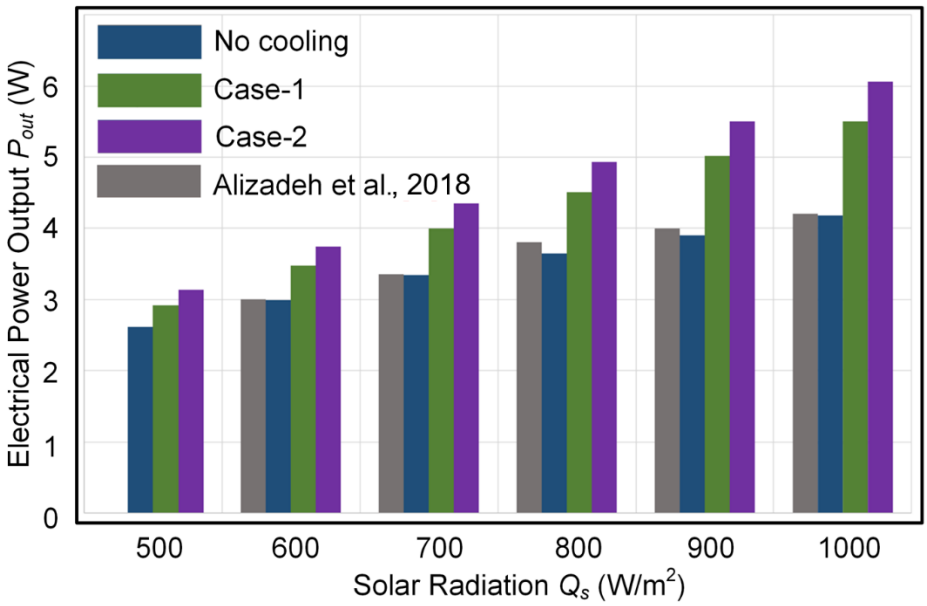

Figure 5.5 Electrical power output of the PV panel for various scenarios of thermal management at corresponding solar radiation. Reprinted with permission from Poudel et al. [125] arXiv (2021).

Following the findings of the PV panel cooling with the nanochannels, we report the performance of the PV panel in terms of electrical power output. As the employed thermal management reduces the surface temperature of the PV panel, this in turn enhances the photoelectric conversion efficiency and the electrical power output of the system. By considering the steady state average temperature of the PV panel surface (T_s), Eq. 5.2 is utilized to compute the electrical power output for the range of solar radiation considered in the present study. The chart in Fig. 5.5 shows the electrical power output attained with the cooling via nanochannels (Cases 1 and 2) as compared to the case without any thermal management. The chart also shows the numerically obtained results for the steady state electrical power output of the consistent PV

panel without employing any cooling as reported in a recent study [115]. In the range of Q_s considered, average enhancement of ε_{el} = 32.8% in the electrical power output is achieved with the employed thermal management corresponding to Case-2. The reported ε_{el} in the present work surpasses that in many other techniques of PV panel cooling including active spray (ε_{el} ~7%) [118], pulsating heat pipes (ε_{el} ~18%) [115], phase change material (ε_{el} ~23%) [128], pulsed water spray (ε_{el} ~27%) [105], hybrid photovoltaics-thermoelectric-heat system (ε_{el} ~30%) [129], etc.

5.4 Summary

This chapter presents a numerical investigation of photovoltaics (PV) panel cooling by employing spray-cooling heat flux dissipation on porous nanochannels integrated on the back face of the PV panel. The energy balance equation on the PV panel system is solved numerically to obtain the spatial and temporal variation of the temperature over the PV surface for different cases with and without thermal management. The extent of cooling achieved by applying thermal management with nanochannels device for a range of incident solar radiation is studied in detail. The numerical method is also used to deduce a universal curve which can predict the magnitude of PV cooling of any generic thermal management technique. The universal curve revealed the existence of a theoretical limit for the extent of cooling. Finally, the employed nanochannels device exhibited an excellent performance with an average cooling of up to 31^{o}C indicating its performance to be near the predicted theoretical limit. The overall enhancement in the electrical power output by 32.8% is obtained which surpasses other similar cooling methodologies reported in the literature.

Chapter 6: Disjoining Pressure Driven Flow in Nanochannel

6.1 Introduction

The absolute pressure in a nanoscale thin liquid film is significantly reduced from bulk due to solid-liquid interatomic interactions; such a reduction is characterized by the well-established disjoining pressure theory [130]. The effect of disjoining pressure on liquid film pressure is mathematically captured through the modified Young-Laplace equation. [131] Disjoining pressure also occurs in several other natural and engineering processes where thin liquid films are ubiquitous, such as in heat-transfer, [3, 4, 7, 23, 34, 36, 44, 46, 123, 131-133] droplet-spreading, [23, 34, 134] and those involving bubbles, [131, 135-137] etc. The quantitative contribution of interatomic interaction to disjoining pressure is dependent on the atomic composition and distance from the surface. It is mainly attributed to van der Waal's force if either solid or liquid atoms are non-polar; long-range electrostatic forces dominate when both solid and liquid atoms are polar. Since many natural phenomena and engineering applications involve the polar fluid water, we focus on the scenario comprising water – silicon dioxide combination where electrostatic forces can affect molecular motion of water up to tens to hundreds of nanometers from the surface [138-140]. On the basis of the quantification of disjoining pressure for polar liquid in a Gibbsian composite system [141, 142], here we develop a numerical model to gain broader understanding of transport of water in nanoscale pores and its potential impact on transpiration in 100 m tall redwood trees.

In current literature, theoretical estimation of disjoining pressure of polar molecular combinations, i.e. water – silicon dioxide, using DLVO theory requires approximation of surface potential; [143] while discrete numerical simulations, such as molecular dynamics, are currently limited by the computational ability to simulate large domains. In our recent work, [142] the

disjoining pressure of water was quantitatively characterized by conducting wicking experiments in 1-D silicon dioxide nanochannels. Disjoining pressure was found to dominate the driving mechanism for the liquid wicking in low height nanochannels (h < 100 nm). The average value of disjoining pressure ($\widehat{P_d}$) in the water film was deduced as an exponential function of the film thickness (δ) (i.e. half of the channel height); [142] however, due to the challenges of measuring local pressure at locations away from the surface at the nanometer scale, the knowledge of the disjoining pressure distribution in water film as a function of the distance (y) from the surface, $P_d(y)$, is still lacking [130, 144]. In this work, we first derivate an expression of $P_d(y)$ based on our prior experimental findings, then integrate $P_d(y)$ in continuum simulations, and finally apply the developed numerical methodology to investigate the transpiration mechanism. For this purpose, two different computational domains are considered. First, to validate the numerical technique of integrating the effect of disjoining pressure $P_d(y)$ in the Computational Fluid Dynamics (CFD) simulation, wicking in nanochannels of geometry consistent to recent experimental study [142] is investigated and presented following which, the developed method is employed in the system consisting of nanopore-tube-ground water tank to resemble the transpiration process in 100 m tall trees.

Stomatal transpiration in trees can generate the pressure difference for passive transport of water from ground to the leaves. [145, 146] Trees self-regulate the size of stomata pore opening which can range between micrometers [147] to a few nanometers [148]. In tall trees such as redwoods [149] which are 100 m high, a pressure difference of more than 10 times the atmospheric pressure is required to pull water against gravity from the soil to the leaves. Thus, assuming water in the soil is at 1 atm, absolute negative pressure more than -11 atm are supposed to occur in stomata pores. The overall process involves the evaporation of water at liquid vapor interface

in stomatal opening which potentially generates such large pressure difference enabling the passive flow of water. Thus, comprehension of the absolute negative pressure in liquid and the passive propagation of water in nanoscale pores is crucial to build the fundamental understanding of the process.

6.2 Expression of disjoining pressure

Here, we first develop an expression to estimate disjoining pressure of water as a function of distance from the solid wall $P_d(y)$, following which we implement the disjoining pressure effect in a commercial CFD solver by supplementing an additional source term in the momentum equation. The implementation is then utilized to simulate the wicking process of water in nanochannels connected to a reservoir (Fig. 6.1a). Our work integrates and validates a molecular level phenomenon (disjoining pressure) into continuum simulations and can be further used to study nanoscale effects as well as design engineering systems involving nanoscale liquid flows.

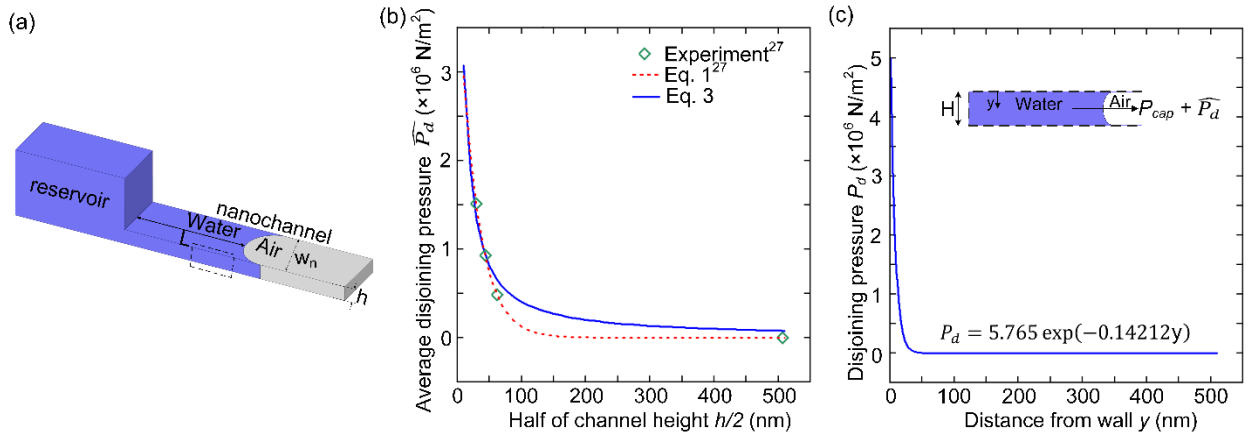

Figure 6.1 Wicking in nanochannel. (a) Schematic of water wicking in a nanochannel connected to a reservoir. (b) Variation of average disjoining pressure existing in a nanochannel with channel half-height. (c) Variation of disjoining pressure with distance from the wall. Reprinted with permission from Poudel et al. [150]. arXiv (2021).

Equation 6.1 represents the average value of disjoining pressure of water in nanochannel ($\widehat{P_d}$) as a function of the liquid film thickness (=$h/2$ which is half the nanochannel height) obtained from curve fit of experimental data in our recent work [142] (Fig. 6.1b). In order to develop an expression of P_d as a function of the distance from the surface (y), we adopt a similar exponential function as shown in Eq. 6.2, where *A* and *B* are constants to be determined. By integrating Eq. 6.2 with respect to y as shown in Eq. 6.3, the average disjoining pressure of water in nanochannel can be obtained, and then compared against Eq. 6.1 to estimate the constants as explained next.

$$\widehat{P_d} = 4.25 \exp\left(-0.035 \frac{h}{2}\right) \qquad \text{Equation 6.1}$$

$$P_d = A \exp(-By) \qquad \text{Equation 6.2}$$

$$\widehat{P_d} = \frac{1}{h}\int_0^h P_d(y)\, dy = \frac{1}{h}\int_0^h A \exp(-By)\, dy = \frac{A[1-\exp(-Bh)]}{hB} \qquad \text{Equation 6.3}$$

Constants *A* and *B* were determined by an iterative process. First, random values were assigned in Eq. 6.3, whose results were compared to that from Eq. 6.1. The values were converged in each iteration by minimizing the error between $\widehat{P_d}$ computed from Eq. 6.1 and Eq. 6.3. The convergence is obtained by estimating the coefficient of determination R^2 between the solutions of Eqs. 6.1 and 6.3 for '*N*' number of different nanochannel height cases with the corresponding h. Based on this analysis, the best fits of *A* and *B* are selected for the highest and the most stable value of R^2 (i.e., the value of R^2 which would be independent of the number of data-points considered). Eventually, constants *A* and *B* were finalized as 5.765 and 0.14212 respectively (see Eq. 6.4), with R^2 = 91.3% resolved to the precision of Δy = 1 nm with ~500 data points. Additional details on the iterative process to obtain values of *A* and *B* are also provided in Appendix A3.

$$P_d = 5.765\exp(-0.14212y)$$ Equation 6.4

Substituting these values of A and B, the averaged disjoining pressure ($\widehat{P_d}$) from Eq. 6.3 is in good agreement with both experimental data and fitting curve (Eq. 6.1) prediction (Fig. 6.1b). The corresponding disjoining pressure distribution P_d in water film is plotted in Fig. 6.1c.

Table 6.1 Nanochannels geometry and corresponding contact angles at top and side walls [142]

Case	Reservoir (Microchannel Geometry)		Nanochannel Geometry		Contact Angle on Nanochannel walls	
	Height (h_m)	Length (L_m) = 150 µm, Width (w_m) = 40 µm	Channel height (h)	Channel Length (L_n) = 150 µm, Channel width (w_n) = 10 µm	Top Wall	Side Wall
1	1.7 µm		59 nm		90°	29.4°
2	2.5 µm		87 nm		90°	27.3°
3	3.5 µm		124 nm		64.8°	40.6°
4	30 µm		1015 nm		39.6°	39.6°

6.3 Integration to CFD simulation

Next, to simulate the wicking process in nanochannels of geometry consistent with experiments [142] (Table 6.1), disjoining pressure effect is implemented in continuum simulation using a laminar multiphase model with the volume of fluids method. A commercial CFD software ANSYS Fluent is utilized to solve the governing equation of fluid flow and a *udf* which is linked to the momentum equation to specify the source term based on the disjoining pressure function. [151, 152] As shown in Fig. 6.2a, a nanochannel of height (h), length (L_n), and width (w_n) is

connected to the reservoir of height (h_m), length (L_m), and width (w_m). L_m and w_m were fixed as 150 µm and 40 µm respectively, while h_m changed with nanochannel height (h) with a fixed ratio (h_m /h) of ~30. Four channel heights (h) of 59 nm, 87 nm, 124 nm, and 1015 nm were simulated with fixed channel length L_n of 150 µm, and width w_n of 10 µm (Table 6.1). Based on the advantage of symmetry, only one-fourth portion of the physical domain is considered for the CFD simulation (Fig. 6.2b). The faces AB and EF towards the reservoir and the nanochannel respectively are open with the pressure outlet (1 atmosphere) boundary condition. The face ADF is symmetric and no-slip condition is set at all walls of nanochannel and reservoir. Surface tension is evoked using a continuous shear force model [153] (liquid-air surface tension γ = 0.072 N/m) together with wall adhesion and specified contact angles. The contact angles on the side and top walls of each case of nanochannel height are adopted from our prior experimental work [142] and are listed in Table 6.1. While the values of the contact angles for the small and large height nanochannels presented in Table 1 are obtained directly through an analysis based on experimental visualization and molecular dynamic simulation [142], the contact angle on top wall of the nanochannel with intermediate height h = 124 nm is not explicitly available. Thus, the same is deduced here employing an analysis based on the average disjoining pressure. In the earlier experimental study [142], the average disjoining pressure in the case of nanochannel with h = 124 nm is considered as a mean of two different scenarios (denoted as $\widehat{P_{d-m}}$) corresponding to the contact angles on the top wall (θ_{t-w}) of the channel: 90° and 39.6° respectively, while the contact angle on the side wall being (θ_{s-w} = 39.6°). For the CFD simulation, we introduce a new contact angle on the top wall ($\theta_{t-w}{}^{*}$), which would induce a disjoining pressure equivalent to $\widehat{P_{d-m}}$.

From the previous work[142], $\widehat{P_{d-m}}$ = 452,488.6 Pa

Hence,

$$\widehat{P_{d-m}} = \frac{6\mu C^2}{h^2} - 2\sigma\left(\frac{cos\theta_{t-w}^{*}}{h} + \frac{cos\theta_{s-w}}{w}\right) \qquad \text{Equation 6.5}$$

Where, C is the slope of fitted curve in wicking distance *v/s* $t^{1/2}$ plot; C = 1.62 for nanochannel with h = 124 nm, w = 10 µm [142].

Solving Eq. 5, we get θ_{t-w}^{*} = 64.8° (also see Table 6.1) which is utilized for simulation in case of h = 124 nm.

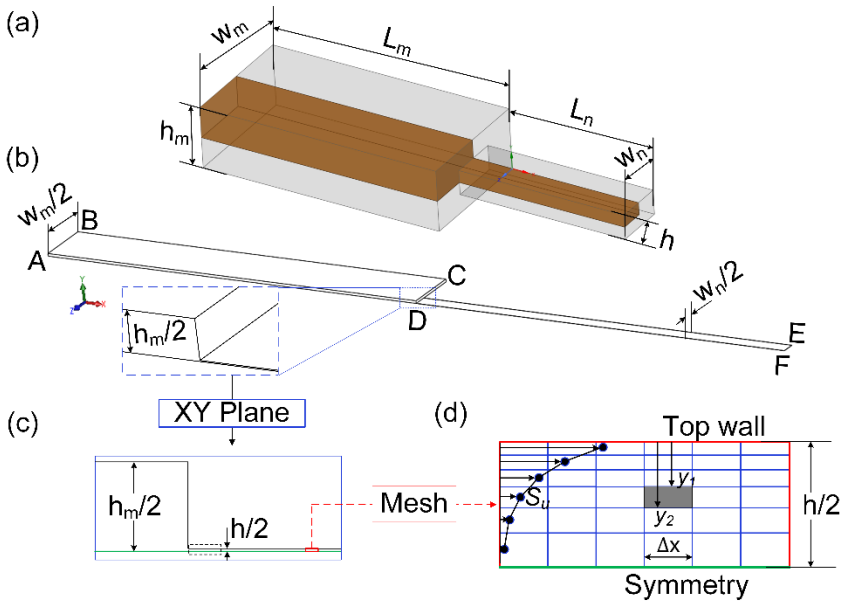

Figure 6.2 CFD Simulation of water wicking in a nanochannel. (a) Sketch of a nanochannel connected to a reservoir showing symmetry. (b) Computational domain utilized in the present study. (c) XY plane view of the domain showing the plane of symmetry. (d) Mesh refinement near the wall of nanochannel together with the specified source term profile along the height. Reprinted with permission from Poudel et al. [150] arXiv (2021).

Figure 6.2c illustrates a magnified view of the XY plane of the domain with the plane of symmetry (green line) and Fig. 6.2d demonstrates mesh refinement near the top wall of the nanochannel.

The effect of the disjoining pressure (Eq. 6.4) is included by adding a source term S_u in the liquid phase, which is added to the discretized form of the X-momentum equation through a *udf* as follows:

$$S_u = \int_{y_1}^{y_2} \frac{P_d}{\Delta x} \qquad \text{Equation 6.6}$$

where, y_1 and y_2 are limits of the finite volume cell in Y-axis and Δx is the cell width along X-axis (see Fig. 6.2d). The stated source term in the corresponding momentum equation is estimated at the center of each finite volume cell and acts as a supplementary driving force for liquid propagation. Moreover, the computational domain is discretized non-uniformly with the refined grid spacing (smaller finite volume cells) near the wall (see Fig. 6.2d) to better capture the exponential effect of disjoining pressure. Additional details on wicking simulation with uniform and non-uniform grids along with the grid-independence test and the Richardson's error estimation [154] for relative error in simulation is provided in Appendix A3.

6.4 Results

6.4.1 Wicking in nanochannel

Figure 6.3a shows the evolution of wicking distance *L* with time from CFD simulations for all four channel heights. By including the effects of both P_{cap} and P_d, the simulation data are in good agreement with experimental data. [142] Thus, the expression of disjoining pressure $P_d(y)$, as a function of distance from the surface y (Eq. 6.4), for water – silicon dioxide combination, as

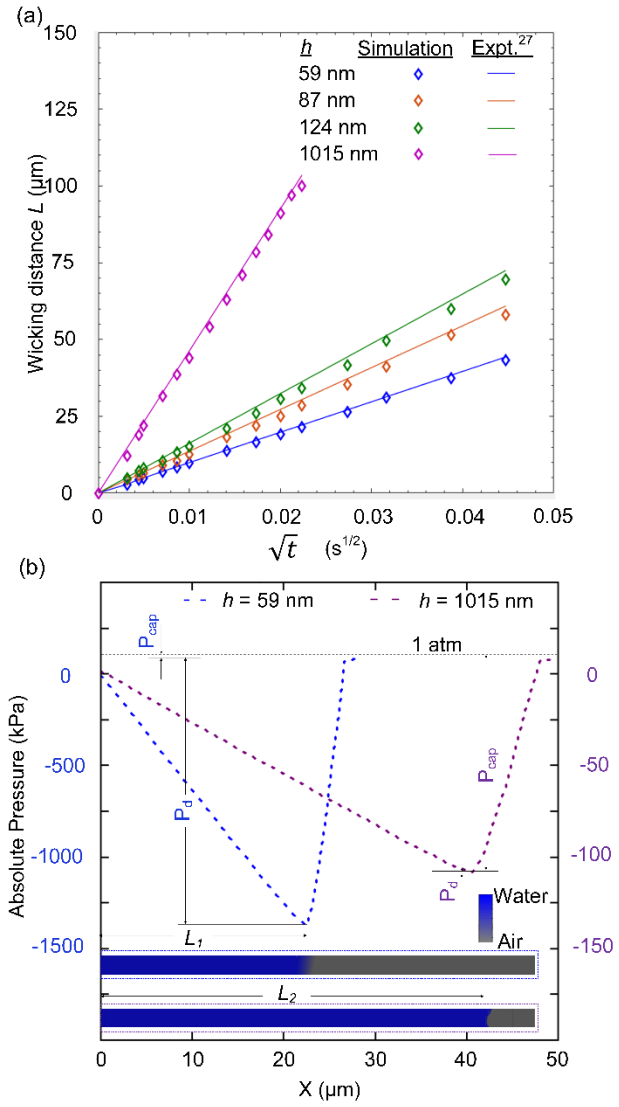

Figure 6.3 (a) Evolution of wicking distance with time for nanochannels of varying height. (b) Absolute pressure along the nanochannel length indicating the peak negative pressure at the meniscus. The inset (corresponding to the dashed-box of Fig. 6.2c) shows the liquid phase volume fraction contour plot of the nanochannel. Reprinted with permission from Poudel et al. [150] arXiv (2021).

well as the implementation of disjoining pressure effect to CFD solver is demonstrated to be accurate as they adequately reproduce the experimental outcome. Further information and

numerical values of S_u for each case of channel height are also provided in Appendix A3. The findings from the present work can be used to further study phenomenon where near-surface effects on liquid behavior are non-trivial.

The variation of pressure along the direction of wicking in 59 nm and 1015 nm channels is shown in Fig. 6.3b. During this process, there exists a pressure gradient along the direction of wicking with a peak negative pressure (P_n) at the meniscus, [4, 23, 42] and is estimated from the corresponding contour plots (insets of Fig. 6.3b) of liquid volume fraction inside the channel. The capillary pressure is obtained by $P_{cap} = 2\sigma\left(\frac{\cos\theta_{side}}{h} + \frac{\cos\theta_{top}}{w}\right)$, with contact angle values listed in Table 6.1; while the value of average disjoining pressure is obtained from Eq. 6.1. Table 6.2 lists all values of P_{cap}, $\widehat{P_d}$ and P_n for all channel heights. For small channel heights (<100 nm), P_d dominates and thus the relation $P_d \approx P_a - P_n$ holds; while in 1015 nm channel, P_d is negligible and thus the relation $P_{cap} \approx P_a - P_n$ applies. From this investigation of liquid film pressure, the relative contribution of P_{cap} and P_d on the overall driving mechanism is found to widely vary for the two extreme heights of nanochannels considered in the present study.

Table 6.2 The values of different pressures associated with each case of nanochannel height.

Channel height (h)	P_{cap}	$\widehat{P_d}$	P_n
59.6 nm	1.25×10^4	1.39×10^6	-1.40×10^6
87 nm	1.28×10^4	9.30×10^5	-8.78×10^5
124 nm	4.46×10^5	6.54×10^5	-8.23×10^5
1015 nm	1.09×10^5	7.91×10^4	-1.05×10^4

6.4.2 Transpiration in Trees

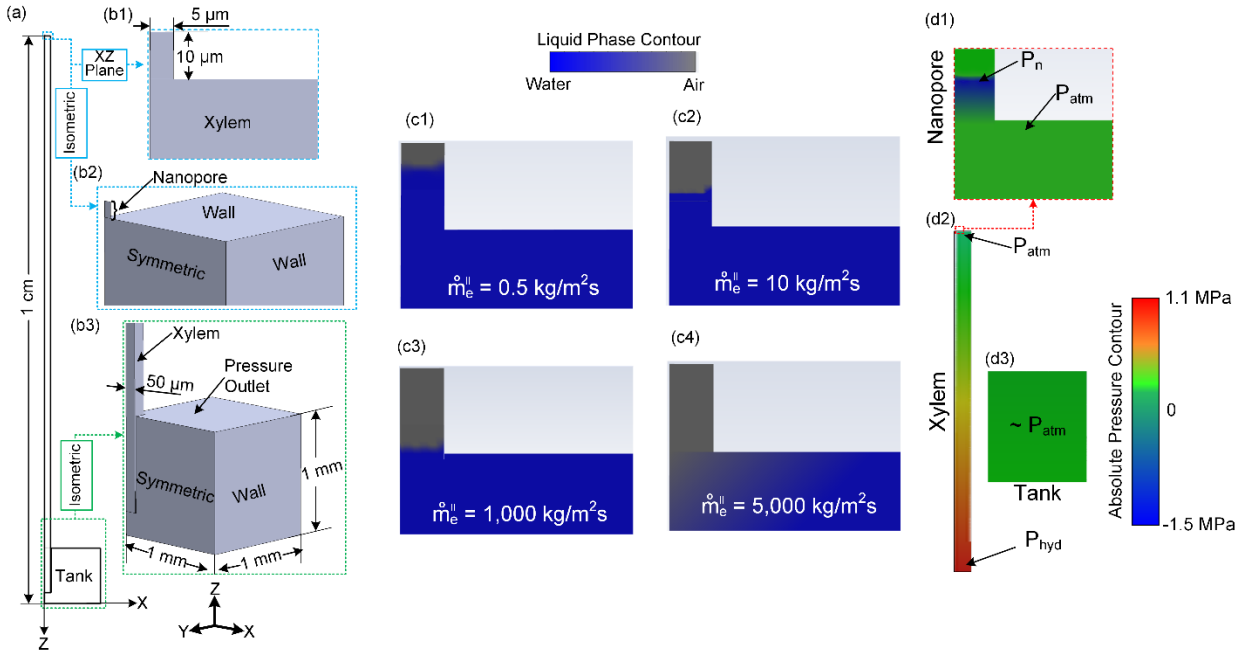

Figure 6.4 Numerical simulation of stomatal transpiration and passive water flow in xylem tubes. (a) Computational domain. (b) Different zones of computational domain indicating the boundary conditions. (c) Liquid phase contour plot illustrating the equilibrium position of meniscus in nanopore for different cases of $\dot{m}_e''$. (d) Absolute pressure contour plot showing the variation of disjoining pressure in nanopore and hydrostatic pressure in xylem. The section of xylem shown in d-2 is not to scale. Reprinted with permission from Poudel et al. [150] arXiv (2021).

Following the implementation of the effect of disjoining pressure in CFD simulation, we investigate the liquid transport through xylem in trees driven by evaporation at stomatal pore. Xylem tube of cross section 100 µm × 100 µm is connected to tank at bottom, and on top of the xylem, a nanopore is provided which resembles the stomatal opening in trees. The nanopore is 10 µm in height with a cross-section 59 nm × 10 µm (consistent to the nanochannel [142] and case 1 of Table 6.1). The nanopore opening is opted to have a rectangular cross section over a

circular/elliptical one since the wettability of water in confinement are well established for a flat surface [142] (also see Table 6.1). In the numerical simulation of transpiration in trees discussed in this section, evaporation (liquid to vapor mass transfer) at the meniscus of nanopore is evoked to represent the stomatal transpiration. Thus, it establishes a numerical system of transpiration driven passive flow of water through xylem in 100 m tall trees.

In the present numerical model, due to the constraint of aspect ratio, xylem height is only 1 cm. However, the operating condition is tuned to resemble a 100 m tall xylem tube by applying gravity equivalent to $10^4 \times g$ ($g = 9.81$ m/s^2) in only the xylem region of the computational domain. All other regions (tank and nanopore) are set with $g = 9.8$ m/s^2. As shown in Fig. 6.4a-b, only one-fourth part of the domain is considered for the simulation based on the advantage of symmetry. Fig. 6.4b also illustrates the geometrical parameters and boundary conditions at different faces of the computational domain. Moreover, the temperature throughout the domain is constant 300 K and the pressure outlet at open boundaries is set at 1 atm. A specified evaporation rate flux (liquid to vapor phase transition) at the meniscus ($\dot{m}_e^{''}$) is induced through a *udf* with mass source term. The effect of varying $\dot{m}_e^{''}$ on the transpiration driven flow is investigated with the focus on the equilibrium stage liquid level in nanopore (h_{np}), liquid transport velocity in xylem (u_{xl}) and in nanopore (u_{np}), and the effective pressure difference driving the passive flow (ΔP).

6.4.3 Evaporation in nanopore and passive water transport

Based on Fick's law of diffusion, the evaporation rate flux from a typical water meniscus is found to be ~0.5 kg/m^{2}s corresponding to the ambient temperature (T = 300 K) and relative humidity (RH = 30%). With the possible rise in temperature and lowering of ambient humidity,

$\dot{m}_e''$ can dramatically increase. Thus, eight different cases are simulated with $\dot{m}_e''$ = 0.5, 2.5, 10, 50, 100, 500, 1000, 5000 kg/m^{2}s. The liquid phase contour plot of the nanopore region indicating the meniscus in equilibrium position for $\dot{m}_e''$ = 0.5, 10, 1000, 5000 kg/m^{2}s is shown in Fig. 6.4c. For the case with the largest $\dot{m}_e''$ (= 5000 kg/m^{2}s), the evaporation mass flux surpasses the wicking flux, consequently receding of the meniscus towards the xylem tube is observed. This indicates non-physical behavior arising due to unnatural high $\dot{m}_e''$. Thus, the case with $\dot{m}_e''$ = 5000 kg/m^{2}s is excluded from further discussion here onwards. Similarly, Fig. 6.4d shows the variation of absolute pressure over the domain (nanopore, xylem, and tank) when the meniscus reaches an equilibrium position for the case with $\dot{m}_e''$ = 2.5 kg/m^{2}s. The two key aspects of absolute pressure in the system: disjoining pressure and hydrostatic pressure are revealed from the plot. The peak negative pressure (P_n) exists at the meniscus in nanopore while the hydrostatic pressure (P_{hyd}) of water in xylem results into the maximum positive pressure at the bottom of xylem.

As the evaporation rate is specified in the simulations, a balance between wicking flux and evaporation mass flux occurs in time and the liquid-vapor interface (i.e., meniscus) reaches an equilibrium stable position in the nanopore. In such an equilibrium, the continuous pull of water from the tank, i.e., against the gravitational pull of 100 m height, takes place in order to replenish the evaporated mass. Accordingly, the equilibrium position of meniscus lies at different heights in the nanopore depending on the rate of evaporation specified. The inset in Fig. 6.5 shows the sketch of evaporating meniscus in nanopore and liquid transport from ground (tank) where h_{np} is defined as distance of meniscus, at equilibrium, from xylem tube. Figure 6.5 shows that a significant drop in h_{np} occurs with higher $\dot{m}_e''$ values. The water transport velocity at xylem (u_{xl}) and in nanopore (u_{np}) is also obtained at equilibrium and plotted in Fig. 6.5. The transport

velocity in xylem is found to be in the order of 10^{-8} to 10^{-5} m/s for the range of $\dot{m}_e^{''}$ considered. Further, the speed of water transport in nanopore is found to be orders of magnitudes higher than that in xylem due to much smaller cross-sectional area. The numerical values of u_{xl} obtained here in a single xylem tube are lower than the reported rate of water transport in trees (~10^{-3} – 10^{-4} m/s) since the water transport in xylem is driven through evaporation in a single nanopore in our study, while multiple stomata are connected to a single xylem in nature. [155, 156]

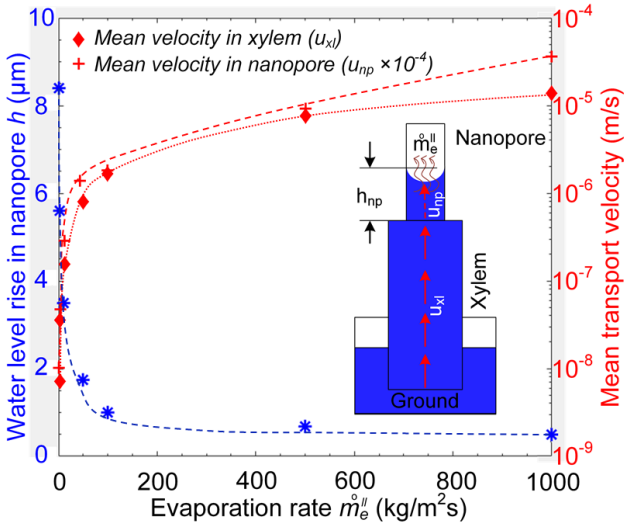

Figure 6.5 Variation of equilibrium stage water level in nanopore and mean transport velocity of water with the evaporation rate flux in meniscus. Dotted lines are guides to the eye. Reprinted with permission from Poudel et al. [150] arXiv (2021).

6.4.4 Pressure difference driving the flow

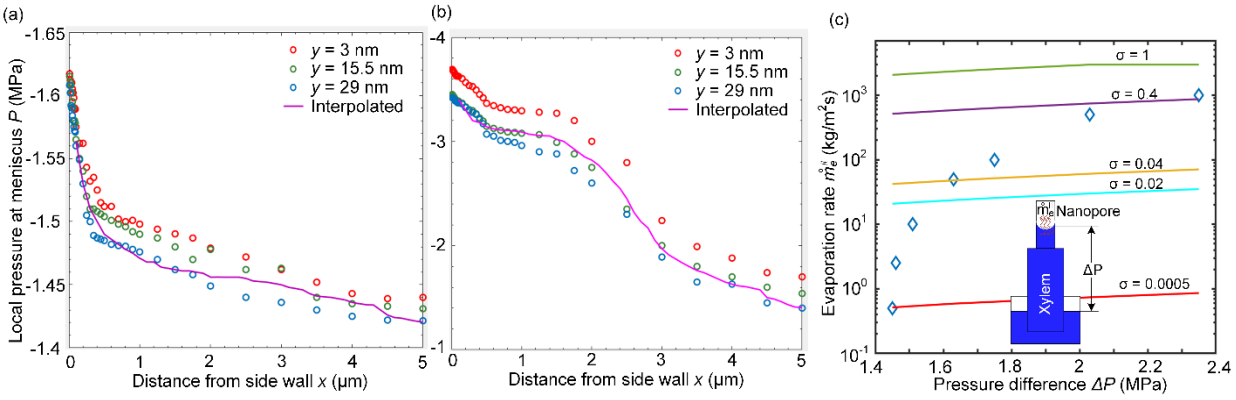

Figure 6.6 Variation of local pressure in the meniscus along X-axis at different depth in Y-axis at the nanopore during equilibrium for $\dot{m}_e^{''}$ = (a) 2.5, (b) 1000 kg/m^{2}s. (c) Relationship between the mass transfer rate at liquid vapor interface and the pressure difference driving the passive flow. Reprinted with permission from Poudel et al. [150] arXiv (2021).

Next, we investigate the pressure at the meniscus to gain insight into the relationship between the stomatal evaporation and the pressure difference driving the passive flow of water. Evaporation at the interface tends to deform the shape of meniscus and induces a local variation of absolute pressure along the meniscus. Such variation needs to be considered in order to estimate the average P_n for a given case of $\dot{m}_e^{''}$. Since the finite volume cells (or grid points) in the computational domain are not uniformly distributed (with refined grid spacing near the solid wall), the simple average of the local pressure values at all grid points along the meniscus is not appropriate to estimate P_n. Thus, the non-uniformly distributed data points in the variation of local absolute pressure in the meniscus along X-axis for each case of $\dot{m}_e^{''}$ (see Fig. 6.6a-b) is utilized to interpolate the local pressure values to the temporarily created uniform grid points along X-axis (Δx = 0.1 μm). The variation of the pressure at the interpolated data points is also

shown in Fig. 6.6a-b and P_n is computed as the mean of the interpolated data points of corresponding case. Here, inducing the evaporation at the meniscus in nanopore is found to greatly reduce the pressure in liquid film. As compared to the average peak negative pressure at the meniscus of P_n = -1.40 MPa without evaporation (see Table 6.2), we obtain P_n to be -1.48 MPa and -2.35 MPa for $\dot{m}_e^{"}$ = 2.5 and 1000 kg/m^{2}s, respectively, during evaporation. Using this methodology, P_n and thus the pressure difference driving the flow i.e., $\Delta P = P_{atm} - P_n$ are computed for all seven cases of $\dot{m}_e^{"}$ and the variation of ΔP with $\dot{m}_e^{"}$ is shown in Fig. 6.6c. Thus, a higher evaporation rate at the meniscus leads to a greater pressure difference which helps overcome the pressure drops in the nanopore and xylem tube, but at the cost of decreasing h_{np}. Eventually, increasing evaporation rate beyond a certain limit causes the meniscus to recede entirely from the nanopore resulting in the failure of the transpiration mechanism (as seen in our simulation case with $\dot{m}_e^{"}$ = 5000 kg/m^{2}s).

6.4.5 Kinetic theory and mass transfer across interface

Lastly, we performed an analysis of maximum mass transfer across an interface based on kinetic theory. [10, 157] The maximum mass flux across a water-vapor interface is given as [157]:

$$\dot{m}_e^{"} = \frac{2\sigma}{2-p_v}\sqrt{\frac{M}{2\pi R}}\left(\frac{p_{l,corr}}{\sqrt{T_l}} - \frac{p_v}{\sqrt{T_v}}\right) \qquad \text{Equation 6.7}$$

where, σ is accommodation coefficient, (M = 0.018 kg/mol) is the molar mass of fluid, (R = 8.314 J/K.mol) is ideal gas constant, (T_v = 300 K) and (p_v = 101325 Pa) are saturated vapor temperature and pressure respectively, (T_l = 300 K) is temperature of liquid, $p_{l,corr}$ is the corrected liquid pressure which is a function of p_n, surface tension of liquid (γ_{lv} = 0.072 N/m), radius of pore (r_p ~ 1 μm) and density of liquid (ρ = 1000 kg/m^3) [10]:

$$p_{l,corr} = p_n \exp\left(-\frac{2\gamma_{lv}M}{r_p R\rho}\right)$$ Equation 6.8

Here the value of $\dot{m}_e^{"}$ is dependent on accommodation coefficient which varies significantly with different fluids and is sensitive to the molecular properties of fluid. [158] Therefore, $\dot{m}_e^{"}$ is estimated from Eq. 6.8 over the entire range of P_n obtained in our simulations and for varying σ = 0.02, 0.04, 0.4, and 1. As shown in Fig. 6.6c, the variation of $\dot{m}_e^{"}$ with ΔP is found to be strongly dependent on σ. Furthermore, an additional curve for σ = 0.0005 is also created as shown in Fig. 6.6c which agrees with the lower limit of $\dot{m}_e^{"}$ in the present work. Figure 6.6c illustrates that, in order to have a very high flow rate of passive transport of water through xylem, the mass transfer (evaporation) at the meniscus in stomata should be high which in turn necessitates a high value of σ. Hence, this kinetic theory analysis coupled with our simulation results highlight the importance of three factors: 1) disjoining pressure, 2) evaporation rate, and 3) accommodation coefficient to naturally sustain the driving force to pull water against gravity. A practical limit to these factors, mainly tied to nanopore surface characteristics and water properties, result in a height limit to how tall trees can grow. [159, 160]

6.5 Summary

In summary, we utilize the experimental findings of average disjoining pressure of water in nanochannels and derive an expression for disjoining pressure distribution in a water film as a function of distance from the surface. The developed disjoining pressure expression is implemented in computational fluid dynamics solver to perform simulations of wicking in nanochannels and capture near-surface molecular effects. The simulation results are in excellent agreement with the experimental data, demonstrating the successful implementation and validation of disjoining pressure in continuum simulations. The disjoining pressure in the liquid

film was found to be the primary driving mechanism for the flow in geometry of characteristic dimension < 100 nm. The implementation of disjoining pressure is further utilized to numerically simulate the transpiration process in trees. The relationship between the evaporation rate at liquid-vapor interface in nanopore and the consequent pressure difference created to drive the passive flow of water through xylem is studied in detail. Within a critical limit, a higher rate of evaporation at the nanopore meniscus is found to be associated with larger pressure difference driving the flow of water and the higher flow rate through xylem tubes in 100 m tall trees. When the evaporation rate is between 1000 - 5000 kg/m^2s, the disjoining pressure driven supply of water cannot balance the evaporation at the meniscus thus resulting into the retraction of the meniscus and failure of the system with self-driven transpiration mechanism in trees. The numerical investigation is supplemented with an analysis based on kinetic theory which dictates a limit on the maximum mass transfer at the liquid-vapor interface demonstrating the upper limit on height of trees. The present work provides insights to the mechanism of transpiration and passive water transport on trees as well as lays a foundation for future continuum studies of physical phenomenon where nanoscale liquid films are prominent.

Chapter 7: Homogeneous Bubble Nucleation in Nanochannel

7.1 Introduction:

Liquid-vapor phase-change phenomenon is an extensively discussed topic in literature. Latent heat associated with phase-change enables a large amount of heat transfer that can be engaged in a multitude of applications including electronics cooling, waste heat recovery, energy-conversion, nuclear reactors, building thermal management, etc. [161-166] Along with the surge in the use of various micro/nanoscale geometries to enhance the phase-change heat-transfer, it necessitates the detail understanding of thermodynamic and physiochemical processes involved in wicking, thin-film evaporation, and vapor bubble nucleation in such geometries. Accordingly, several studies in the past have reported the detail physics and practical implications of the processes of wicking [23, 34, 165, 167, 168], thin-film evaporation [28, 48, 69, 169], boiling [43, 46, 170-172], spray-cooling [31, 173, 174], etc. and have indicated the superior performance of micro/nano scale structures due to greater wettability and enhancement in three-phase contact lines. Amongst these, the investigation of phase-change inside nanoscale confinement is particularly interesting but vaguely understood phenomenon in heat transfer. Due to an extremely high rate of phase-change heat transfer at micro/nano scales, the phenomenon gathers attention for further exploration and interpretation that can facilitate to advance heat transfer research.

The comprehension of the vapor bubble nucleation and growth phenomenon is mostly limited within the scope of boiling over the open geometry of micro/nano scale structures achieved during pool or flow boiling. [46, 169, 170, 175-177] Because of the challenges associated with the altered properties of liquid under nano-confinement and a unique physiochemical behavior arising due to dominance of disjoining pressure, [130, 131, 178] the investigation of the bubble

nucleation within nanoscale confinement has not yet been reported. [179-181] Although molecular dynamics based simulations [180, 182, 183] and a few experiments [179, 181, 184] shed some light on the fundamental of temperature and pressure during bubble nucleation, they still lack the association with the key parameter disjoining pressure and nor do they provide knowledge of heat-fluxes. Moreover, the nucleation studies reported in literature involve either heterogeneous nucleation [182, 184-186] or consider the working fluid other than water [179, 183, 187]. The investigation of nucleation behavior in the confined nanoscale film of polar liquid (water) can potentially advance the development of future heat-transfer device that can be employed in nuclear reactors, electronic cooling, or outer space applications. Thus, the systematic study of homogeneous nucleation inside the confined geometry of nanochannel pre-filled with deionized (DI) water by considering the implication of disjoining pressure is the focus of the present work. Our recent study, where we experimentally studied the wicking in nanochannels of different heights and obtained the expression of disjoining pressure as a function of nanoscale liquid film thickness [178] lays the foundation of our present work. The experimental finding [178] was latter utilized to develop a generalized expression of disjoining pressure as a function of distance from the solid wall for water-SiO_2 pair, and the effect of disjoining pressure was also implemented in a commercial Computational Fluid Dynamics (CFD) software ANSYS Fluent [188] in a separate work. [150] The same expression of P_d along with the implementation in CFD simulation is utilized here to investigate the liquid-vapor phase change (nucleation) inside the confined space of nanochannel of height (h = 59 nm).

7.2 Methods

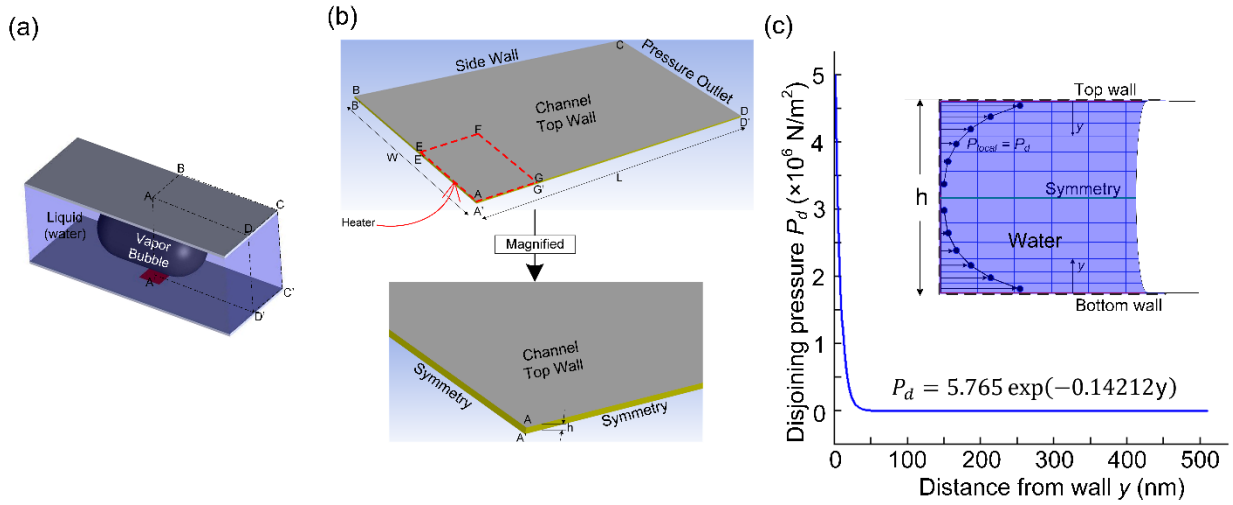

Figure 7.1 (a) Sketch of a vapor bubble inside the nanochannel containing confined water film and a source of constant heat provided at the bottom of the channel. (b) Computational domain illustrating the boundary conditions. (c) Variation of disjoining pressure with the distance from wall in water-SiO2 pair. (Reproduced with permission from arXiv. Poudel et al. (2021) [150]). Inset in (c) shows the variation of pressure along the grid-points in the direction of channel height. (Poudel et al. – Under Review)

In the present work, the investigation of vapor bubble nucleation inside the confined space of nanochannel is performed using numerical simulations. A nanochannel of height (h = 59 nm) and width (w = 10 μm) is initially filled with deionized (DI) water at room temperature. When a heat source (either a point laser in experiment or the constant heat-flux boundary condition in simulation) is applied at a spot on one of the faces of the nanochannel, temperature of the liquid rises, and a vapor bubble nucleation is ultimately observed as shown in Fig. 7.1a. Computational domain utilized for CFD simulation is shown in Fig. 7.1b. Here, the computational domain (ABCD-A'B'C'D') is taken as one-fourth part of the physical domain due to the advantage of

symmetry. Figure 7.1b also illustrates the boundary conditions associated with different faces of the computational domain. Solid walls of the nanochannel are provided with adiabatic and no-slip boundary conditions with the wettability consistent to our previous studies [150, 178]. The exit of the channel is designated as pressure outlet with 1 atm pressure. The spot of heating A'E'F'G' at the bottom wall of the nanochannel highlighted with red dotted line is provided with no-slip wall and specified heat-flux.

$P_d = 5.765 \exp(-0.14212y)$ Equation 7.1

where, y is the distance from SiO_2 surface (wall).

During initialization, liquid water is filled in entire domain and heat is supplied at the hotspot. The expression of variation of the disjoining pressure with the distance from the wall [150] (provided in Eq. 7.1) is shown in Fig. 7.1c. Equation 7.1 is utilized to induce the effect of disjoining pressure in the nanoscale liquid film under confinement. The pressure at the grid-points along the channel height is altered using this expression in numerical simulation (Eq. 7.1) with a user defined function (UDF) containing ADJUST function in FLUENT. [189] A system of pressure variation inside the channel having the maximum absolute pressure at the grid-point nearest to the solid wall is achieved. The variation of such adjusted pressure at the cross-section of the nanochannel is also illustrated in the inset of Fig. 7.1c.

In addition to the pressure adjustment, the simulation is set with the liquid-vapor phase change (saturation) temperature as the function of local pressure. The maximum and minimum local pressure at the corner and center of the channel correspond to the relatively higher and lower saturation temperature respectively. This effect of disjoining pressure and the relationship of pressure with saturation temperature allows the initial phase change near the center of the

channel cross-section or at the mid-height. Initial phase change is the onset of nucleation, later the vapor bubble either grows or diminishes or shows non-physical behavior based on various combinations of specified heat-flux (q) and phase-transition coefficient (C_o) which will be discussed in later section. Furthermore, the effect of disjoining pressure in the nanoscale liquid film is such that it supplements the driving force for the propagation of liquid. [150, 178] Such effect was implemented in CFD simulation by inducing an additional source term (S_u) once the vapor bubble is formed and liquid-vapor interface is distinct. S_u in the finite volume cells has the direction towards the center of the vapor bubble. Further details in the implementation of the effect of disjoining pressure on the nucleation inside nanochannel is discussed in Appendix A4 along with flow-chart of the steps.

7.3 Results

When the specified heat-flux is applied at the heater section of the bottom wall of the nanochannel, initial sensible heating of the liquid film takes place. Since the absolute pressure of the liquid around the mid-height region of the nanochannel is lowest, the region corresponds to the lowest saturation temperature. Hence, the initiation of the vapor bubble nucleation occurs at the mid-height of the nanochannel. Figure 7.2a shows the top view of the vapor bubble during formation for the case with q = 30 W/cm^2 and $C_o = 10^7$. Figure 3b-c shows the side-sectional view of the vapor bubble inside the nanochannel which clearly illustrates a scenario of homogeneous nucleation. In the present study, q and C_o are varied in a wide range to investigate their effect on nucleation temperature (T_o), vapor bubble size as well as the liquid film thickness underneath the bubble (d_L) (see Fig. 7.2c). The findings of simulation are also compared with the independent experiment of vapor bubble nucleation inside the fabricated sample of SiO_2 nanochannel. [178]

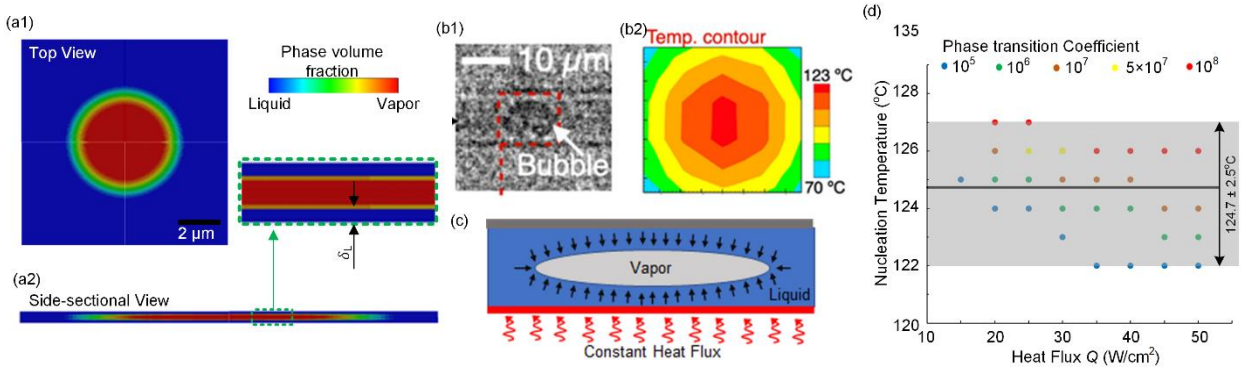

Figure 7.2 Vapor bubble nucleation inside confined space of nanochannel. (a1-a3) Top and side-sectional view of vapor bubble nucleation after supplying heat-flux at the hotspot along with the liquid film thickness (d_L) underneath the vapor bubble highlighting the homogeneous nucleation. Vapor bubble (b1) Under microscope, and (b2) Temperature contour plot observed using the infrared camera showing the nucleation temperature for h = 59 nm obtained experimentally. (Reproduced with permission from ACS 2021 [178]). (c) Schematic of a vapor bubble at the mid-height of the nanochannel along with heat-flux at the bottom wall and the source term directed towards the center of the vapor bubble. (d) Variation of nucleation temperature with specified heat-flux at hotspot obtained for various cases of phase-transition coefficients. (Poudel et al. – Under Review)

Figure 7.2 b-1 and b-2 show the experimentally obtained high-speed camera visualization image and infrared camera image respectively for the case of vapor bubble nucleation inside nanochannel h = 59 nm. [178] The nucleation temperature was found to be 123 ^{o}C consistent to the one obtained from CFD simulation ~ 125 ^{o}C. In case of experiment, it is observed that the liquid water quickly rewets the SiO_2 wall when the heat source is turned off and the vapor bubble collapses. [178] It is inferred that the disjoining pressure which is dominant near the surface

leads to the intact liquid film adsorbed to the solid wall without the formation of three-phase contact line. Accordingly, the source term (S_u) introduced in CFD simulation as discussed in Section 7.3 is also active with the presence of liquid-vapor interface and the resultant effect of the combination of q, C_o and S_u determines the vapor bubble shape and size. Figure 7.2c demonstrates S_u acting towards the center of the vapor bubble (black arrows) while the continuous supply of heat takes place from the bottom.

First, q is varied between the range of 5 – 50 W/cm^2 at the step of 5 W/cm^2, and C_o is varied in the range of 10^5 – 10^8 and the effect on T_o is recorded for each case. For a very small q (< 20 W/cm^2) and all values of C_o except 10^8, the supplied heat-flux only increases the temperature of liquid but never approaches the saturation temperature for a very long duration of time (> 1000 μs) thus no nucleation is observed for those cases. For rest of the cases, the variation of T_o with q is shown in Fig. 7.2c. Interestingly, a very small variation in T_o (124.7 ± 2.5 ^{o}C) is detected for the range of q and C_o considered. The saturation temperature (phase-transition) is set as the function of local pressure which in turn is dictated from P_d via ADJUST function and is independent of q and C_o. Hence, such T_o is found to be nearly independent on q and C_o. However, the shape of vapor bubble and similarity with the experimental observation [178] differs within such variation which requires an additional investigation on the q and C_o resulting into the various scenarios of vapor bubble nucleation as discussed next.

When q and C_o are varied, four different scenarios of nucleation or no-nucleation are obtained as demonstrated in Fig. 7.3a. As mentioned earlier, for q < 20 W/cm^2, no phase-transition thus no-nucleation is achieved, and such scenario is referred as Case-A. Similarly, for the relatively larger values of q and C_o (Case-B), initial vapor bubble formation is achieved however such bubble vanishes due to the dominant effect of S_u acting towards the center of the bubble. In

contrast to Cases-A, B, for a combination of the very large q and C_o, nucleation takes place, and the vapor bubble continuously grows preventing the rewetting of nanochannel wall and allowing the formation of 3-phase contact line (see Fig. 7.3d). Nevertheless, a narrow range of q and C_o is identified which corresponds to a steady state vapor bubble (see Fig. 7.3c). Such scenarios of steady state vapor bubble and continuously growing bubble are referred as Case-C and Case-D respectively. Figure 7.3a-d shows the volume fraction contour plot illustrating the initial and steady state of four scenarios of nucleation. Additionally, a phase-diagram between q and C_o is constructed as shown in Fig. 7.3e and the shaded regions are also formed to distinguish various scenarios (Cases-A to D). Evidently, a narrow band of green region in the phase-diagram corresponds to the cases of nucleation which is consistent to the experimental observation. [178]

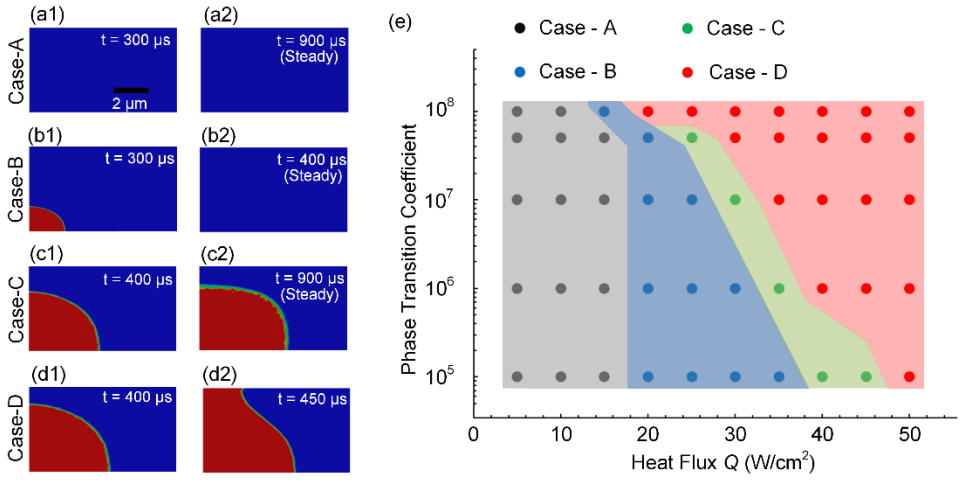

Figure 7.3 Vapor bubble nucleation showing initial and final steady state phase volume fraction contour plots for (a) Case-A, (b) Case-B, (c) Case-C, and (d) Case-D. (e) Phase diagram between phase transition coefficient (C_o) and supplied heat-flux (q). (Poudel et al. – Under Review)

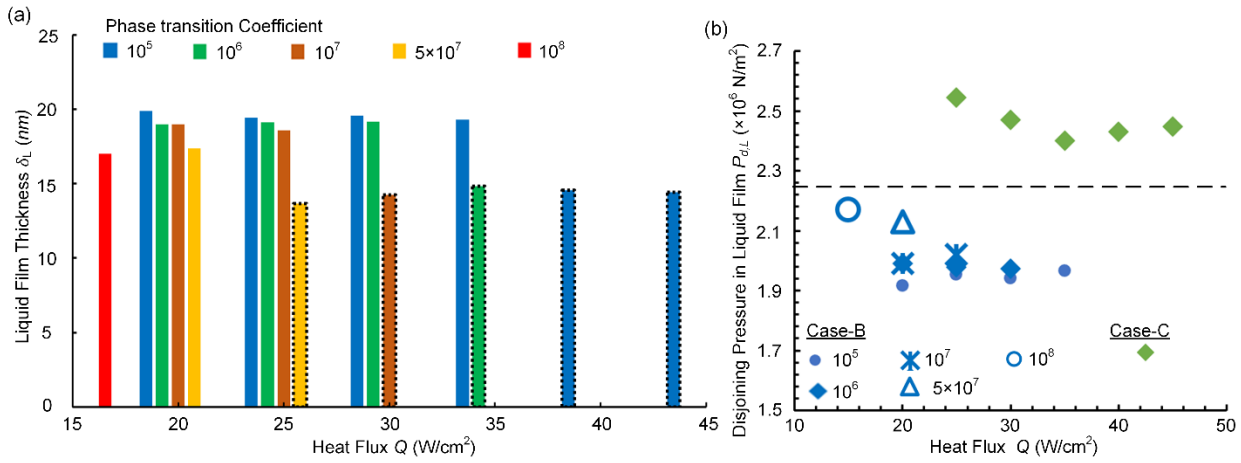

Figure 7.4 (a) Liquid film thickness for various cases of bubble nucleation simulation. (b) Variation of disjoining pressure in the liquid film underneath the vapor bubble with the supplied heat-flux. (Poudel et al. – Under Review)

Additionally, to comprehend the physics behind this observation, the average liquid film thickness underneath the vapor bubble (d_L) and the associated disjoining pressure in such liquid film ($P_{d,L}$) are investigated next. Figure 7.4a shows the d_L for all situations corresponding to simulations of Case-B, and C. For Case-C, d_L is smaller (< 15 nm) as compared to Case-B, and for Case-D the three-phase contact line is formed which prevents the effective estimation of d_L due to the transient nature. The smaller d_L observed for Case-C indicates a higher $P_{d,L}$ which is apparent from the plot in Fig. 7.4b. The variation of $P_{d,L}$ shown in Fig. 7.4b for the scenarios of Case-B, C are calculated using Eq. 7.1 for the corresponding value of $y = d_L$. The maximum $P_{d,L}$ observed is in the range of 2.4 – 2.6 MPa. The reason behind the observation of the formation of three-phase contact line in Case-D is the disjoining pressure in the liquid film is insufficient to keep the liquid film intact at higher q and C_o thus causing the liquid film thickness to continuously decrease and eventually dry out.

7.4 Summary

In this chapter, we report the numerical investigation of bubble nucleation behavior in nanochannel. The phase-change phenomenon under nanoscale confinement is studied by considering the effect of disjoining pressure which is responsible to alter the properties and behavior of polar liquid (water) under confinement. By performing a series of simulations, a systematic study of the effect of heat-flux and phase-transition coefficient on the bubble nucleation and growth is understood. The information of heat-flux, liquid-film thickness underneath the bubble, and the associated disjoining pressure in such liquid-film are determined which would otherwise be impossible to obtain experimentally. In order to have a homogeneous nucleation, there exists a limit on supplied heat-flux (approx. 50 W/cm^2), beyond which the disjoining pressure in liquid-film thickness cannot sustain the evaporation rate causing the film to dry out and form the three-phase contact line. The results of simulation demonstrate an excellent agreement with the experimental findings as well as open a novel methodology of investigating bubble nucleation in nano confinement by employing computational fluid dynamics.

Chapter 8: Conclusion and Future Work

8.1 Conclusion

Droplet coupled wicking was studied, by experimental and numerical techniques, on fabricated cross-connected nanochannels of height ~728 nm and ~100 nm, buried under a SiO_2 surface, with pores at each intersect. An analytical model based on capillary pressure and viscous resistance was developed to predict the evolution of wicking distance with time. During the later stage of the droplet wicking phenomenon, evaporation from the menisci at micropores and nanochannels dominates which consequently removes the heat from the substrate through evaporative cooling. Numerical simulation using computational fluid dynamics is carried out to understand the dynamics of evaporation on such nanochannels. Findings from CFD demonstrate the existence of varying menisci shapes which create new contact line regions underneath the pores causing the exponential increment of evaporation flux. Evaporation flux along with wicking flux velocity and pressure distribution along the nanochannel were estimated in submicron porous nano/microstructures, with potential design applications in heat pipes and spray cooling technologies.

Moreover, the evaporation of a droplet on the same nanochannels sample is studied at elevated temperatures. The droplet placed on the surface wicks into the channels through the pores and enables tracking of the evaporating menisci through time-resolved visualization. Wicking characteristics and evaporation rates were determined for the varying droplet volumes from 4 µl to 10 µl and surface temperatures ranging from 35^oC – 90^oC. It was found that initial wicking in the nanochannels was independent of surface temperature and droplet volume. In the later stage of droplet wicking i.e., evaporation dominant regime, the maximum wicking distance does not depend on droplet volume at high surface temperatures. Additionally, evaporation flux from

channels/pores, where the thin-film menisci are present, was found to be about two orders of magnitude higher than from the droplet interface, and corresponding heat flux as high as ~294 W/cm^2 was obtained from the channels/pores. Applying the experimental findings of heat transfer and wicking characteristics towards the potential use of spray cooling based thermal management, high heat flux dissipation ~ 77 W/cm^2 can ideally be attained from thin-film evaporation in the porous nanochannels. An additional enhancement in cooling performance can be achieved by further optimizing the nanochannels/micropores geometry.

Moving ahead with the further work in thermal management using micro/nano structured surfaces, the obtained results is implemented to numerically evaluate the cooling and corresponding performance of output in a commercial photovoltaic panel. The nanochannels device was found to reduce the PV surface temperature significantly with an average cooling of 31.5^oC. Additionally, the enhancement in the electrical power output by ~33% was achieved numerically.

In addition to utilizing the cooling techniques in different applications, further comprehension of fundamental aspects of fluid flow in nanoscale is also equally important. Evidence shows that the properties of liquid in a confined geometry of nanometers scale will be different than in bulk. Unraveling such properties and their implication is important to achieve ultra-high efficient thermal management as well as to comprehend certain engineering and biological flows. One such property is the disjoining pressure of water in confined geometry. Accordingly, an expression of disjoining pressure in a water film as a function of distance from the surface from prior experimental findings is developed. Such an expression is key to understand the disjoining pressure driven flow of nanoscale liquid film as well as to investigate the effect of nanoscale confinement on liquid-vapor phase change. The disjoining pressure is then implemented in a

commercial Computational Fluid Dynamics solver and the effect of the same on wicking in nanochannels of varying height 59 nm – 1 micron is simulated. The passive flow simulation considering the effect of disjoining pressure enabled the investigation of transpiration and water transport on 100 m tall trees. A domain comprising of nanopore connected to a tube with a ground-based water tank, thus mimicking the stomata-xylem-soil pathway in trees is simulated. Moreover, the same technique of disjoining pressure is utilized to study bubble nucleation inside a nanochannel filled with liquid water. The bubble nucleation temperature was found to be ~125^{o}C which agreed with the experimental observation ~123^{o}C. By means of nucleation simulation, lesser-known parameters of homogeneous nucleation like heat-flux, liquid film thickness underneath the vapor bubble, etc. are identified which would aid on development of future high-heat flux dissipating devices.

8.2 Future Work

In near future, first, I plan to investigate the liquid-vapor phase change phenomenon over the nanochannels at an elevated range of temperature (100^{o}C – 300^{o}C). Leidenfrost effect where, liquid close to a surface heated to above the liquid's boiling point creates an insulating vapor layer and liquid doesn't make physical contact with the heated surface is an interesting physiochemical phenomenon in that temperature range which governs several engineering and natural processes. A liquid droplet at Leidenfrost hovers over the surface and offers a frictionless motion. Additionally, from my preliminary study of Leidenfrost over the nanochannels surface, I have found that the temperature of transition to Leidenfrost, as well as the behavior of liquid droplet impact, spreading and droplet rolling to be affected by wettability and porosity the nanochannels surface. Thus, in future, I want to pursue further experiments which can shed light on understanding the phenomenon better.

Next, I want to extend the findings of bubble nucleation in nanochannel to achieve a practical heat-transfer device that can be employed in energy-conversion application as well as in miniaturized devices including micro-electronics for cooling purpose. The comprehension of nucleation temperature and associated heat-flux developed in the present work would provide foundation for the future work. Similarly, the fundamental understanding of disjoining pressure on nanoscale liquid film and its successful implementation on computational fluid dynamics simulation can be utilized to investigate several other physio-biological problems involving liquid films. The physics of flow in blood vessels (especially capillaries), intra-cellular and inter-cellular transport in animals and plants, etc. can be explored with the understanding from the past. Similarly, disjoining pressure being the near-surface phenomenon can also be inter-related with thermal and hydrodynamic boundary layers involved in flow over the surface in applications like microfluids, nanorobots, etc. The numerical modeling of such processes can offer a better design and efficient operation of microfluidic devices, as well as aid on future development of nanorobots and soft robots.

Appendix A1

A1-1 Design of Nanochannels Geometry

The design of nanochannels geometry is such that, the pores provide the way for the supplied liquid to enter into the nanochannels through wicking while the cross-connection of the channels provides easy liquid exchange during liquid spreading. The width of the channels (~4.5 μm) was chosen to be wide enough to allow for imaging the meniscus while also accommodating the ~2 μm size pores at each intersection. The channel height (~728 nm) is designed based on the following factors:

1) The height is limited by the maximum thickness of the sacrificial layers during nano-fabrication, which is around 1 μm due to the film stress.
2) The other factors affecting wicking in channels should be excluded, such as electroviscous effect, disjoining effect, etc. which come into the picture at ~ 100 nm.
3) In order to prevent boiling inside the channels, the characteristic dimension of the channel (~height) has to be less than the critical radius of nucleation (~2-3 μm).
4) The wicking volume and distance should be large enough to conduct analysis with minimum errors, which prefers higher channels.

Based on these reasons, the channel height was chosen to be between 500 nm and 1 micron, and it turned out to be 728 nm after fabrication.

A1-2 Goniometer Images

Figure A3 shows a goniometer image of a sessile droplet deposited on a flat surface of Silicon and on the fabricated nanochannels sample. The intrinsic contact angle for the flat surface is

obtained to be 25.3±1.2° while the contact angle of the droplet at Wenzel state for the hydrophilic nanochannels sample is observed to be 12.5±1.1°.

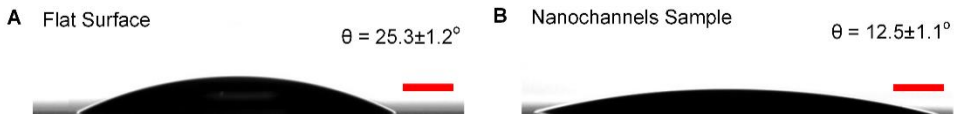

Figure A1 Goniometer images of a sessile droplet deposited on a flat surface and the nanochannels sample

A1-3 Analytical Models

In this section, details in analytical models used to calculate the capillary pressure based on thermodynamic definition and the viscous resistance of wicking flow inside the nanochannels are mentioned.

The thermodynamic definition of the capillary pressure is the ratio of change in surface energy ΔE to the change in volume ΔV during liquid propagation in one unit cell of the nanochannels.

$$P_{cap} = \frac{\Delta E}{\Delta V} = \frac{\gamma r_f \cos\theta_c [2*\{(W+S)^2 - W^2\} + 4WH]}{H((S+W)^2 - S^2)} \quad \text{(Equation A1)}$$

where, γ is surface tension, r_f is the roughness factor for the nanochannels wall which is close to 1 (from AFM images in section S1), θ_c = 26° is the intrinsic contact angle of liquid (deionized water) on SiO_2 surface (see figure S3), W, S, and H are width, spacing, and height of nanochannels.

Similarly, viscous resistance K_{vr} is equal to the ratio of dP/dx to u_{mean}. And the ratio of dP/dx to u_{mean} is obtained by solving Brinkman's equation which is as follows:

$$\mu \frac{d^2u}{dy^2} - \varepsilon \frac{dP}{dx} - \mu\alpha^2 \varepsilon u = 0 \qquad \text{(Equation A2)}$$

where, u is the velocity of liquid propagation, ε is the porosity (ε = 0.70), μ is viscosity and α^{-2} is the permeability of the nanochannels sample. Permeability is calculated based on the analytical equation as follows:

$$\alpha^{-2} = (S+W)^2 \frac{\ln c^{-1/2} - 0.738 + c - 0.887c^2 + 2.038c^3 + o(c^4)}{4\pi} \qquad \text{(Equation A3)}$$

where, c = solid fraction of the sample, $c = 1 - \varepsilon = 0.30$.

Liquid properties are taken at the respective surface temperature. θ_c is assumed to be constant over all temperatures. Equation A2 is a 2nd order differential equation that needs to be solved for variable 'u'. However, in the equation, 'dP/dx' is also not known so, we cannot compute the explicit value of 'u'. Hence, we solve Eq. A2 to obtain the ratio of 'u' to 'dP/dx' as illustrated below:

The general solution for the differential Eq. A2 will be of the form:

$$u(y) = C_1 \frac{dP}{dx} e^{\alpha\sqrt{\varepsilon}y} + C_2 \frac{dP}{dx} e^{-\alpha\sqrt{\varepsilon}y} - \frac{1}{\alpha^2\mu}\frac{dP}{dx} \qquad \text{(Equation A4)}$$

Now, applying the no-slip boundary condition at u(y = - H/2) = 0 (bottom wall of nanochannel) and and u(y = H/2) = 0 (top wall of the nanochannel), we get the solution as follows:

$$(y) = \frac{1}{\alpha^2\mu}\frac{dP}{dx}\left(\frac{1-e^{-\alpha\sqrt{\varepsilon}H}}{e^{\alpha\sqrt{\varepsilon}H}-e^{-\alpha\sqrt{\varepsilon}H}}\right)e^{\alpha\sqrt{\varepsilon}y} + \frac{1}{\alpha^2\mu}\frac{dP}{dx}\left(1-\frac{1-e^{-\alpha\sqrt{\varepsilon}H}}{e^{\alpha\sqrt{\varepsilon}H}-e^{-\alpha\sqrt{\varepsilon}H}}\right)e^{-\alpha\sqrt{\varepsilon}y} - \frac{1}{\alpha^2\mu}\frac{dP}{dx} \qquad \text{(Equation A5)}$$

$$\Rightarrow u(y) = \frac{dP}{dx}\left(\frac{1}{\alpha^2\mu}\right)\left[\left(\frac{1-e^{-\alpha\sqrt{\varepsilon}H}}{e^{\alpha\sqrt{\varepsilon}H}-e^{-\alpha\sqrt{\varepsilon}H}}\right)e^{\alpha\sqrt{\varepsilon}y} + \left(1-\frac{1-e^{-\alpha\sqrt{\varepsilon}H}}{e^{\alpha\sqrt{\varepsilon}H}-e^{-\alpha\sqrt{\varepsilon}H}}\right)e^{-\alpha\sqrt{\varepsilon}y} - 1\right]$$

$$\Rightarrow \left(\frac{u(y)}{\frac{dP}{dx}}\right) = \left(\frac{1}{\alpha^2\mu}\right)\left[\left(\frac{1-e^{-\alpha\sqrt{\varepsilon}H}}{e^{\alpha\sqrt{\varepsilon}H}-e^{-\alpha\sqrt{\varepsilon}H}}\right)e^{\alpha\sqrt{\varepsilon}y} + \left(1-\frac{1-e^{-\alpha\sqrt{\varepsilon}H}}{e^{\alpha\sqrt{\varepsilon}H}-e^{-\alpha\sqrt{\varepsilon}H}}\right)e^{-\alpha\sqrt{\varepsilon}y} - 1\right]$$

Finally, the expression ‘u(y) / (dP/dx)’ is used to calculate the required ratio as follows:

$$\left(\frac{\frac{dP}{dx}}{u_{mean}}\right) = \frac{1}{\int_{-H/2}^{H/2}\left(\frac{u(y)}{\frac{dP}{dx}}\right)dy} \quad \text{(Equation A6)}$$

Thus, we have, viscous resistance as:

$$K_{vr} = \frac{dP/dx}{u_{mean}} \quad \text{(Equation A7)}$$

Finally, the analytical solution for wicking distance is given as:

$$w_d = G\sqrt{t} \quad \text{(Equation A8)}$$

where, $G = \sqrt{2P_{cap}/K_{vr}}$ is known as the propagation coefficient.

Appendix A2

A2-1 Experimental Procedure

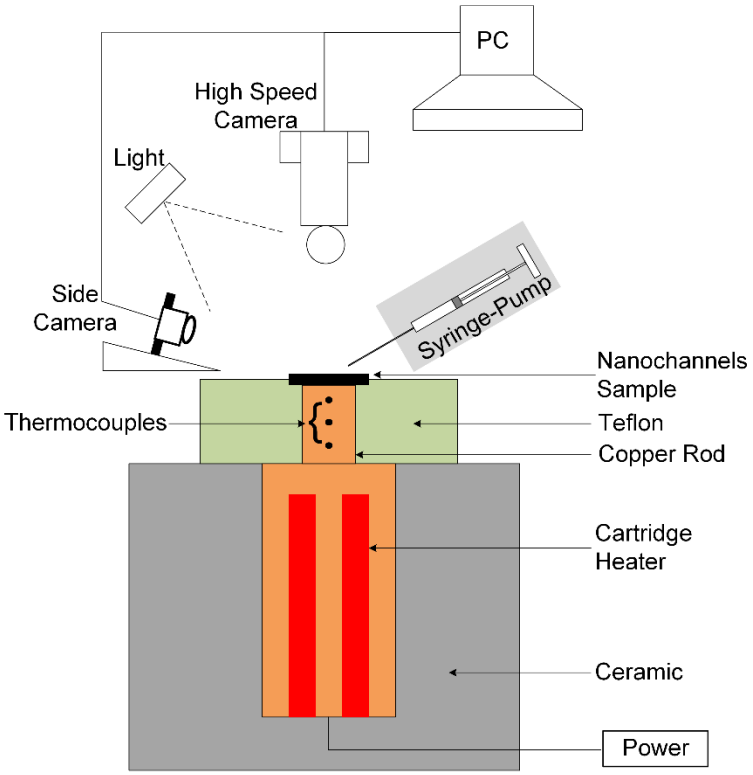

Figure A2 Schematic of the experimental setup

Figure A2 illustrates a schematic of the experimental setup used in the study of droplet evaporation on porous nanochannels. As shown in the figure, a copper rod heater enclosed in a Teflon shell is supplied with power through a cartridge heater for surface heating. The nanochannels sample is bonded on the top of the copper rod using a proper solder. The temperature of the nanochannels surface is estimated by extrapolating the thermocouples reading at a different location along the axis of the copper rod. A PID controller is used to stabilize the surface temperature through controlled heating during the experiments. For the generation of the precise volume of sessile droplet, the syringe controlled using an automatic pump with least

count 0.1 ul and error < 0.35%. The syringe-pump arrangement is capable to traverse vertically. In order to acquire the time-resolved images of droplet wicking in the nanochannels sample, a high-speed camera is mounted at the top of the arrangement, which captures the phenomena at 50 frames per second. As the nanochannels wall is made of 300 nm of SiO_2 layer, we can view the internal flow through the nanochannels top wall and visualize the wicking behavior inside the nanochannels. A side camera at an inclination of 12^o is also used to monitor the temporal variation of the amount of liquid sitting at the top of the sample during wicking and evaporation. The acquired images are stored and analyzed to obtain the physical data of wicking and evaporation in nanochannels. Each case is carried out at least twice and the results are found to be repeatable.

A2-2 Droplet and Spray Parameters

Figure A3 presents the different relevant geometrical areas used in the calculation in the present work. First, the wetted area (A_{wd}) and spherical cap are (A_{sp}) as shown in Fig. A3 A, B are calculated by using the following relations:

$$A_{wd} = \pi(R_w^2 - R_d^2) \quad \text{(Equation A9)}$$

$$A_{sp} = \pi(R_d^2 + h_s^2) \quad \text{(Equation A10)}$$

where, R_w, R_d and h_s are obtained directly from experiments as explained earlier.

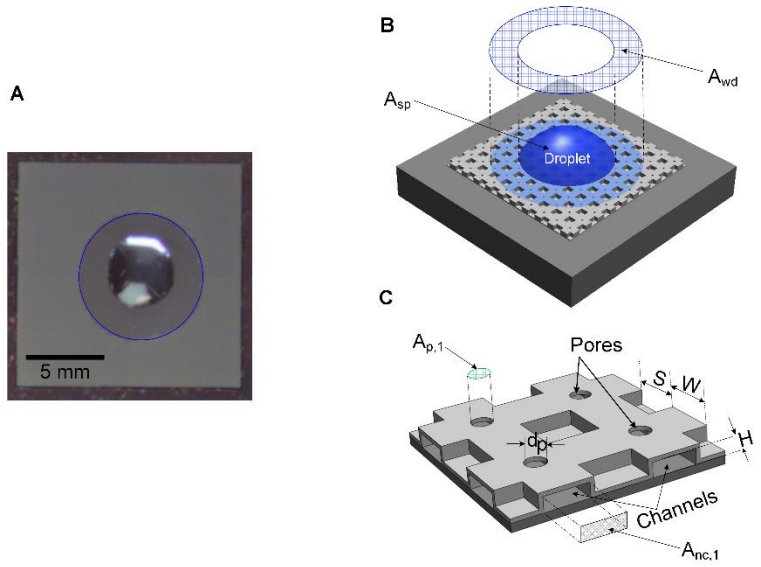

Figure A3 (A) High-speed camera image showing droplet evaporation on nanochannels sample. (B) Isometric view of nanochannels geometry indicating the projected area of an individual pore ($A_{p,1}$) and a nanochannel ($A_{nc,1}$). (C) Droplet wicking sketch to indicate the spherical cap area (A_{sp}) and wicked surface area (A_{wd}).

Next, we calculate the total area of pores within the wicked surface area (A_p) and the area of nanochannels at the circumference or the wicking front (see blue circle in Fig. A5-A) by summing the individual area of a pore $A_{p,1}$ and the individual area of nanochannel $A_{nc,1}$ respectively (see Fig. A5-C). Alternatively, for our uniform geometry of nanochannels, we can consider A_p as a fraction of A_{wd} as follows:

$$A_p = A_{wd} * k_p \quad \text{(Equation A11)}$$

Similarly, A_{nc} also calculated from the circumference as:

$$A_{nc} = 2\pi R_w H * k_{nc} \quad \text{(Equation A12)}$$

where, the constants k_{nc} and k_p are based on geometry of cross connected nanochannels and micropores with values ~0.5 and ~0.0314, respectively.

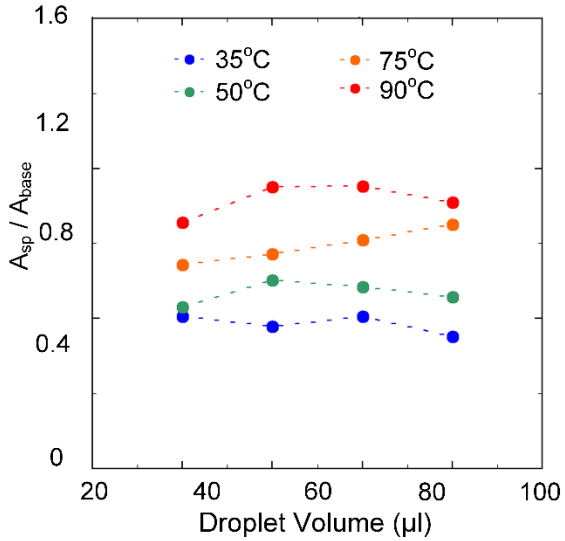

Figure A4 Comparison of area ratio (A_{sp}/A_{base}) associated with spherical droplet on the top surface at different surface temperatures.

Further, the variation of A_{sp}/A_{base} with droplet volume for different temperature is found to be useful in back-calculating the contact angle of the spherical cap on top of the nanochannels by using the following relations for a spherical cap:

$$A_{sp} = 2\pi \frac{R_d^2}{(\sin\theta)^2}(1-\cos\theta) \qquad \text{(Equation A13)}$$

$$A_{sp} = 2\frac{A_{base}}{1-(\cos\theta)^2}(1-\cos\theta) \qquad \text{(Equation A14)}$$

$$\cos\theta = \left(\frac{2}{\left(\frac{A_{sp}}{A_{base}}\right)} - 1\right) \qquad \text{(Equation A15)}$$

Based on these equations, a rough estimation of contact angle ~35° to ~63° in the range of temperature 35°C – 90°C is obtained.

Next, in order to examine the performance of spray cooling on the fabricated nanochannels sample. We considered two different spray parameters each with uniform droplet diameter 400 µm and 20 µm represented by spray-400 and spray-20 respectively. The face-centered-cubic distribution of the droplets and wicked surface area at the top of the sample is considered. For the spray with droplet diameter D_{d-s}, and the corresponding volume V_{d-s}, we compute the spherical cap base radius R_{d-s} as follows:

$$V_{d-s} = \frac{\pi}{6} D_{d-s}^3 \qquad \text{(Equation A16)}$$

$$R_{d-s} = \left(V_{d-s} \frac{3}{\pi(2+cos\theta)(1-cos\theta)^2}\right)^{1/3} sin\theta \qquad \text{(Equation A17)}$$

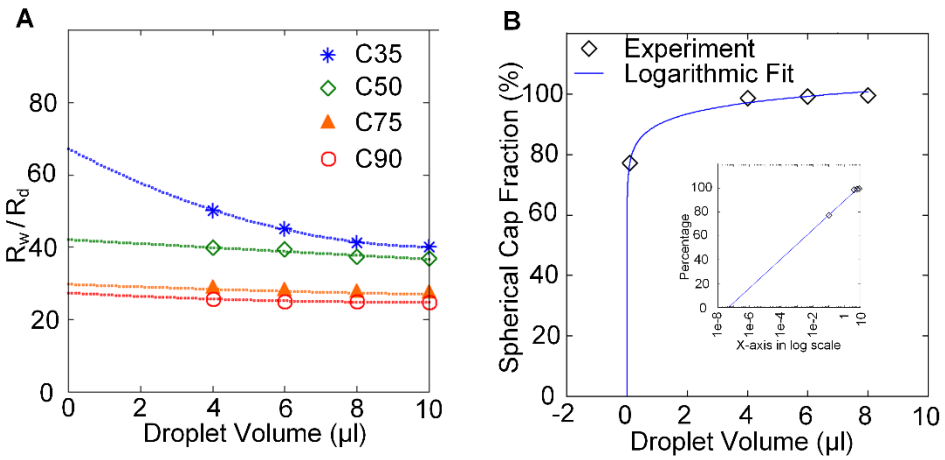

Figure A5 (A) Variation of R_w/R_d ratio with droplet volume and (B) Variation of average spherical cap fraction with droplet volume

Then, wicking radius of an individual droplet of spray participating in heat transfer R_{w-s} is calculated as:

$$R_{w-s} = k_{d-s} * R_{d-s} \quad \text{(Equation A18)}$$

where, k_{d-s} is the ratio of R_w to R_d which is obtained from the 2nd order polynomial curve fit of the results of droplet wicking experiments at each temperature. As shown in Fig. A5-A, the ratio R_w/R_d is obtained for the droplet volume of spray corresponding to spray-400 and spray-20 (see Table A1).

Table A1 Parameters of spray droplets.

Parameters		35°C	50°C	75°C	90°C
k_{d-s}	Spray-400	3.3	2.2	1.46	1.3
	Spray-20				
n_d	Spray-400	15	33	75	96
	Spray-20	5888	13248	30078	379838

Once, R_{w-s} is known, we calculate the maximum number of spray droplets n_d sitting on the sample of 1.4 cm × 1.4 cm in size.

Furthermore, it is inferred from the droplet wicking experiment that, the fraction of spherical cap volume (V_{sp}) of the total droplet volume (V) decreases with a decrease in droplet volume. Hence, we aimed to estimate a critical limit of the spray droplet volume V_{d-s} for which the fraction of the spherical cap volume V_{sp} is '0' and the entire liquid wicks into the nanochannels. With this motive, the variation of spherical cap volume fraction with droplet volume is plotted

and a logarithmic fit to the experimental data points is also generated as shown in Fig. A5-B. In addition to the different droplet volumes studied so far, we performed the wicking test for an additional droplet volume of 0.1 µl and is also shown in Fig. A5-B. With the available resources, a sessile droplet of 0.1 µl size is the limit in terms of droplet generation and analysis using image processing. From the generated logarithmic fit, it is observed that the spherical cap volume fraction would be '0' at the limit of spray droplet size V_{d-s}~4.7E-8 µl, which is equivalent to the spray with a uniform droplet of diameter D_{d-s}~4.5 µm. Hence, the analysis of spray cooling performance using the spray parameter with D_{d-s}~4.5 µm is also performed in a similar manner, which is labeled as *spray-ideal*.

Appendix A3

A3-1 Expression of Disjoining Pressure $P_d(y)$

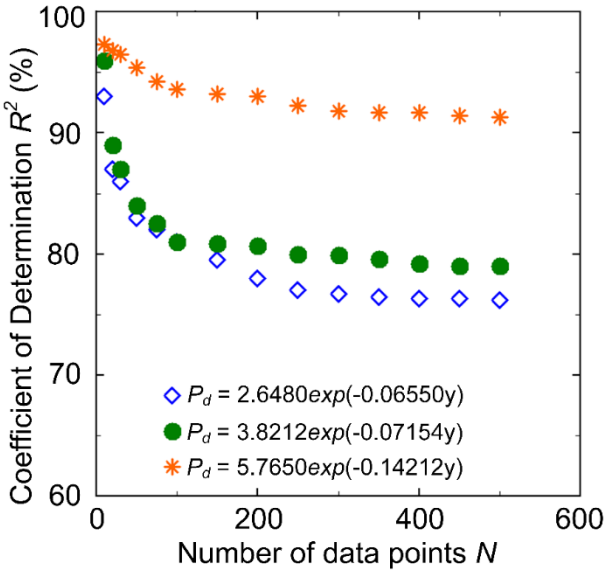

Figure A6 Variation of coefficient of determination with the number of data points for different combinations of A & B.

Equation A19 represents the average value of disjoining pressure of water in nanochannel ($\widehat{P_d}$) as a function of the liquid film thickness (=$h/2$ which is half the nanochannel height) obtained our previous work. In order to develop an expression of P_d as a function of the distance from the surface (y), we adopt a similar exponential function as shown in Eq. A20, where *A* and *B* are constants to be determined. By integrating Eq. A20 with respect to y as shown in Eq. A21, the average disjoining pressure of water in nanochannel can be obtained, and then compared against Eq. A19 to estimate the constants as explained next.

$$\widehat{P_d} = 4.25 \exp\left(-0.035 \frac{h}{2}\right) \qquad \text{Equation A19}$$

$$P_d = A\exp(-By) \qquad \text{Equation A20}$$

$$\widehat{P_d} = \frac{1}{h}\int_0^h P_d(y)\,dy = \frac{1}{h}\int_0^h A\exp(-By)\,dy = \frac{A[1-\exp(-Bh)]}{hB} \qquad \text{Equation A21}$$

Constants A and B were determined by an iterative process. First, random values of A and B were assigned in Eq. A21, whose results were compared to that from Eq. A19. The values were converged in each iteration by minimizing the error between P_d computed from Eq. A19 and Eq. A21. The convergence is obtained by estimating the coefficient of determination R^2 between the solutions of Eqs. A19 and A21 for 'N' number of different nanochannel height cases with the corresponding *h*. By doing so, the best fits for A and B are obtained corresponding to maximum R^2. However, in this scheme, it is possible that R^2 value is very high (>90%) for several combinations of A and B, especially when the number of data points used for comparing R^2 is low (N < 20). Figure A8 shows the variation of R^2 with N for three different sets of A and B. It is noted that when the number of data points 'N' increases, R^2 drops for most of the cases (or combinations of A and B). Based on this analysis, the best fits of A and B are selected for the highest and the most stable value of R^2 (i.e., the value of R^2 which would be independent of the number of data-points considered). Eventually, constants A and B were finalized as 5.765 and 0.14212 respectively (see Eq. A22), with R^2 = 91.3% resolved to the precision of Δy = 1 nm with ~500 data points.

$$P_d = 5.765\exp(-0.14212y) \qquad \text{Equation A22}$$

A3-2 Mesh Parameters

As explained earlier, the supplied source term (S_u) to induce the effect of disjoining pressure will clearly be dependent on grid-spacing. Accordingly, when the computational domain (nanochannel) is discretized into finite volume cells, two different scenarios of grid-spacing

come into the picture; especially, along the channel height, the grid spacing could be uniform or non-uniform. Thus, we performed CFD simulation for h = 59 nm nanochannel case with uniform and non-uniform distribution of 6 finite volume cells along $h/2$ each. The result of wicking distance (L) evolution with time (t) is compared for these two cases. As shown in Fig. A9-a a mesh with non-uniform grid spacing along the channel height (i.e., grid spacing refined near the top wall of the nanochannel) is found to better include the disjoining pressure effect on wicking as compared to one with uniform gird. Thus, a mesh with refined grid spacing near the wall is employed in all cases of simulation considered in the present study.

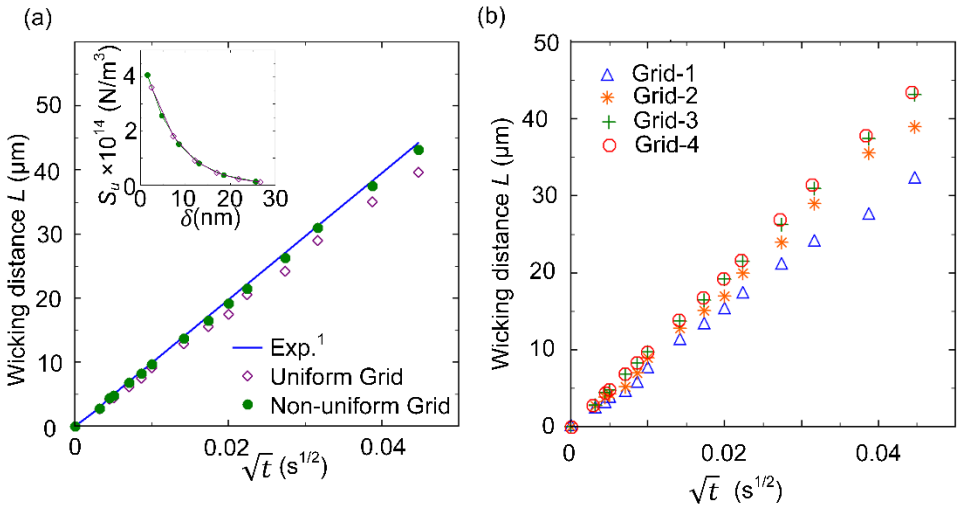

Figure A7 Comparison of wicking distance evolution with time for simulation in nanochannel of h = 59 nm (a) Employing uniform and non-uniform grid spacing. (b) By using different levels of mesh refinement for non-uniform grid.

Next, a grid-independent study was performed by varying the number of finite volume cells along the channel height, using different meshes. For the 59 nm channel, four different meshes with non-uniform grid spacing were utilized, with 4, 5, 6, and 7 finite volume cells along the channel half-height respectively (denoted as Grid-1, Grid-2, Grid-3, and Grid-4. As seen in Fig.

A7-b, the result of Grid-3 (6 finite volume cells) is consistent with the result of Grid-4 (7 finite volume cells), indicating that Grid-3 is an optimum one. Moreover, an analysis of Richardson's error estimation is employed to obtain the relative error in simulation with different grids. In this method, the wicking results for h = 59 nm with Grid-2, Grid-3, and Grid-4 are utilized for estimating the relative error in computation; Grid-3 is considered a base grid while Grid-2 and Grid-4 are relatively coarse and fine grids, respectively.

Thus, the error values for the coarse and fine grids:

$$E_1^{Coarse} = \frac{R_{32}^{o} R^{o} \varepsilon}{1 - R_{32}^{o}} \qquad \text{Equation A23}$$

$$E_2^{Fine} = \frac{\varepsilon}{1 - R_{43}^{o}} \qquad \text{Equation A24}$$

where, ε is the absolute error value between the wicking distance for corresponding grids, R is the mesh refinement factor ($R_{jk} = {R_j}/{R_k}$) and for a 3D mesh, it can be obtained by using Eq. A25 for a j[th] mesh and o is the order of accuracy which is taken as 2 in the present analysis.

$$R_j = \left[\frac{1}{N}\sum_i^N \Delta V_i\right]^{1/3} \qquad \text{Equation A25}$$

Where, ΔV_i is the volume of the i[th] cell of the computational domain and N is the total number of finite volume cells in the j[th] mesh.

Finally, the grid-convergence index (GCI) is calculated based on the errors:

$$GCI = F_S |E| \qquad \text{Equation A26}$$

Where, F_S is the factor of safety ($F_S = 2$).

Table A2. Richardson's Error and Grid Convergence Index.

t (μs)	L_{coarse} (μm)	L_{base} (μm)	L_{fine} (μm)	ε_{coarse}	ε_{fine}	E_1^{coarse}	E_2^{fine}	GCI_{coarse} %	GCI_{fine} %
20	0.0038	0.0044	0.00442	0.0006	-2E-05	-0.00529	1.87E-04	1.058442	3.74E-02
50	0.0052	0.00685	0.0069	0.00165	-5E-05	-0.01455	4.67E-04	2.910716	9.34E-02
400	0.017	0.0192	0.0193	0.0022	-0.0001	-0.0194	9.34E-04	3.880954	1.87E-01
2000	0.039	0.0432	0.0435	0.0042	-0.0003	-0.03705	2.80E-03	7.409095	5.60E-01

Table A2 shows the details of error values and GCI at different instants of time during wicking in nanochannels for h = 59 nm. It is evident that the absolute values of error for the fine grid (E_2^{fine}) is much lower than the corresponding value for the coarse grid (E_1^{coarse}). The grid-convergence values reveal that the error in simulation results based on Grid-3 is minimum with

extensive grid convergence. Thus, meshing based on Grid-3 is used and wicking simulations are performed for different channel heights.

A3-3 Spatial variation of S_u

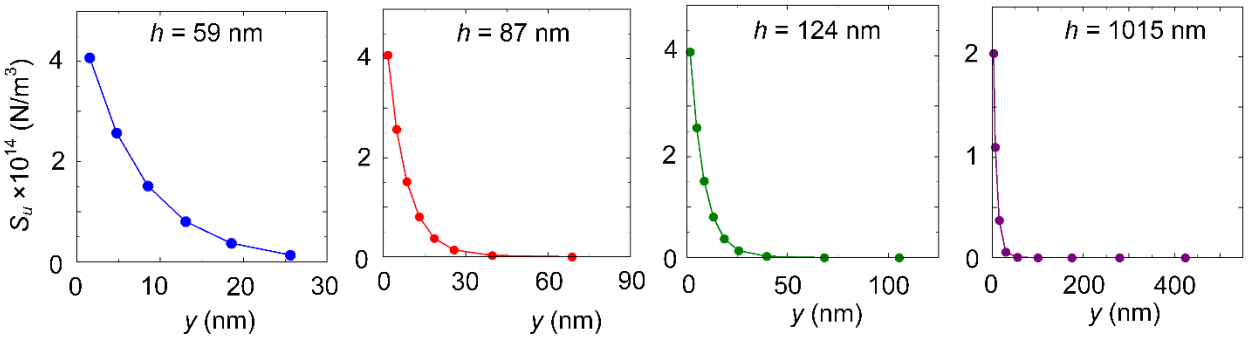

Figure A8 Spatial variation of additional source term (S_u) along the channel half-height to include additional driving force due to disjoining pressure.

The plots in Fig. A8 show the spatial variation of S_u in the direction of channel height for each case of channels discussed in Chapter 6. The number of data points (solid circle) in each plot denotes the corresponding number of finite volume cells along $h/2$, and the horizontal axis indicates the distance of the finite volume cell center from the top wall of the channel. These numerical values of S_u are obtained from the method explained in Chapter 6.

Appendix A4

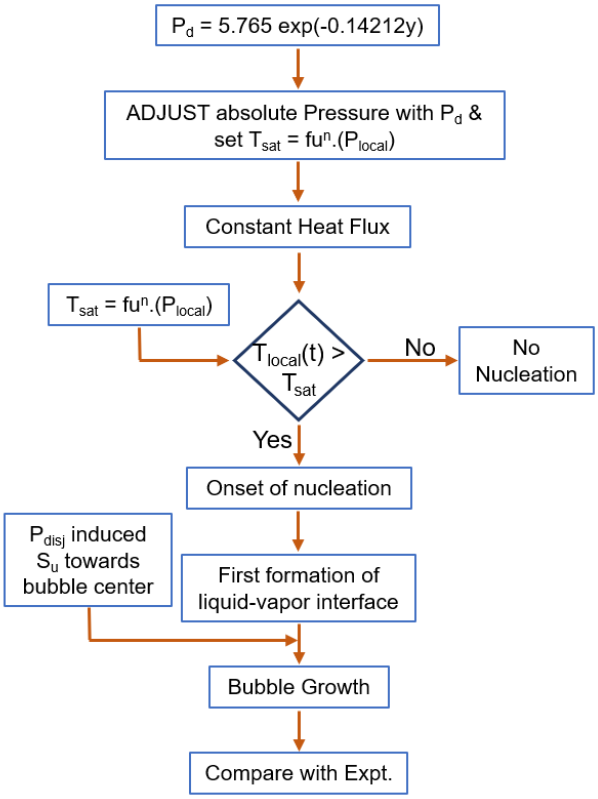

Figure A9 Flow chart showing the implementation of disjoining pressure in CFD simulation and the steps to investigate bubble nucleation.

The expression of disjoining pressure is first implemented in CFD simulation by using ADJUST function in Fluent, the entire steps is illustrated in Fig. A9. This function sets the grid points at different values of absolute pressure allowing the variation inside the nanochannels along the channel height. A constant heat-flux supplied at the bottom wall of the nanochannel initially heats the water film which tends to transit phase into vapor depending on the local pressure. The saturation temperature is set to be function of local pressure thus, allowing the initial phase change (onset of nucleation) to occur at the mid-height of the nanochannel because of the lowest absolute pressure. Once the vapor bubble forms and the vapor-liquid interface is distinct, another

user defined function is activated which supplies the additional source term in the momentum equation, the resultant of which is directed towards the center of the vapor bubble. Based on the combined effect of source term, applied heat flux and the phase-transition coefficient, the vapor bubble either grows or vanishes or reaches a steady state. Finally, the steady state vapor bubble is compared with the experimental observation.

References:

1. Bodla, K.K., J.Y. Murthy, and S.V. Garimella, *Evaporation analysis in sintered wick microstructures.* International Journal of Heat and Mass Transfer, 2013. **61**: p. 729-741.
2. Gaskell, S.J., *Electrospray: Principles and practice.* Journal of Mass Spectrometry, 1997. **32**(7): p. 677-688.
3. Kim, J., *Spray cooling heat transfer: The state of the art.* International Journal of Heat and Fluid Flow, 2007. **28**(4): p. 753-767.
4. Ranjan, R., et al., *Wicking and thermal characteristics of micropillared structures for use in passive heat spreaders.* International Journal of Heat and Mass Transfer, 2012. **55**(4): p. 586-596.
5. Wemp, C.K. and V.P. Carey, *Tuning superhydrophilic nanostructured surfaces to maximize water droplet evaporation heat transfer performance.* Journal of Heat Transfer, 2018. **140**(10).
6. Hu, H., J.A. Weibel, and S.V. Garimella, *Role of nanoscale roughness in the heat transfer characteristics of thin film evaporation.* International Journal of Heat and Mass Transfer, 2020. **150**: p. 119306.
7. Plawsky, J., et al., *Nano-and microstructures for thin-film evaporation—A review.* Nanoscale and microscale thermophysical engineering, 2014. **18**(3): p. 251-269.
8. Wang, H., S.V. Garimella, and J.Y. Murthy, *Characteristics of an evaporating thin film in a microchannel.* international journal of heat and mass transfer, 2007. **50**(19-20): p. 3933-3942.
9. Hanlon, M. and H. Ma, *Evaporation heat transfer in sintered porous media.* J. Heat Transfer, 2003. **125**(4): p. 644-652.

10. Xiao, R., S.C. Maroo, and E.N. Wang, *Negative pressures in nanoporous membranes for thin film evaporation.* Applied Physics Letters, 2013. **102**(12): p. 123103.

11. Kim, H.D. and M.H. Kim, *Effect of nanoparticle deposition on capillary wicking that influences the critical heat flux in nanofluids.* Applied physics letters, 2007. **91**(1): p. 014104.

12. Kwon, H.-m., J.C. Bird, and K.K. Varanasi, *Increasing Leidenfrost point using micro-nano hierarchical surface structures.* Applied Physics Letters, 2013. **103**(20): p. 201601.

13. Xiang, C., et al., *Large-scale, uniform, and superhydrophobic titania nanotubes at the inner surface of 1000 mm long titanium tubes.* The Journal of Physical Chemistry C, 2017. **121**(28): p. 15448-15455.

14. Cheng, Y.-T., et al., *Microscopic observations of condensation of water on lotus leaves.* Applied Physics Letters, 2005. **87**(19): p. 194112.

15. McCarthy, M., et al., *Materials, fabrication, and manufacturing of micro/nanostructured surfaces for phase-change heat transfer enhancement.* Nanoscale and Microscale Thermophysical Engineering, 2014. **18**(3): p. 288-310.

16. Plawsky, J.L., J.K. Kim, and E.F. Schubert, *Engineered nanoporous and nanostructured films.* Materials Today, 2009. **12**(6): p. 36-45.

17. Carey, V. and A. Wemhoff, *Disjoining pressure effects in ultra-thin liquid films in micropassages—comparison of thermodynamic theory with predictions of molecular dynamics simulations.* 2006.

18. Dhavaleswarapu, H.K., J.Y. Murthy, and S.V. Garimella, *Numerical investigation of an evaporating meniscus in a channel.* International journal of heat and mass transfer, 2012. **55**(4): p. 915-924.

19. Ma, H., et al., *Fluid flow and heat transfer in the evaporating thin film region.* Microfluidics and Nanofluidics, 2008. **4**(3): p. 237-243.

20. Maroo, S.C. and J. Chung, *Heat transfer characteristics and pressure variation in a nanoscale evaporating meniscus.* International Journal of Heat and Mass Transfer, 2010. **53**(15-16): p. 3335-3345.

21. Migliaccio, C.P., H.K. Dhavaleswarapu, and S.V. Garimella, *Temperature measurements near the contact line of an evaporating meniscus V-groove.* International Journal of Heat and Mass Transfer, 2011. **54**(7-8): p. 1520-1526.

22. Narayanan, S., A.G. Fedorov, and Y.K. Joshi, *Interfacial transport of evaporating water confined in nanopores.* Langmuir, 2011. **27**(17): p. 10666-10676.

23. Poudel, S., A. Zou, and S.C. Maroo, *Evaporation Dynamics in Buried Nanochannels with Micropores.* Langmuir, 2020. **36**(27): p. 7801-7807.

24. Zhu, Y., et al., *Prediction and characterization of dry-out heat flux in micropillar wick structures.* Langmuir, 2016. **32**(7): p. 1920-1927.

25. Somasundaram, S., et al., *Thermal design optimization of evaporator micropillar wicks.* International Journal of Thermal Sciences, 2018. **134**: p. 179-187.

26. Vaartstra, G., Z. Lu, and E.N. Wang, *Simultaneous prediction of dryout heat flux and local temperature for thin film evaporation in micropillar wicks.* International Journal of Heat and Mass Transfer, 2019. **136**: p. 170-177.

27. Wei, M., et al., *Optimization and thermal characterization of uniform silicon micropillar based evaporators.* International Journal of Heat and Mass Transfer, 2018. **127**: p. 51-60.

28. Adera, S., et al., *Design of micropillar wicks for thin-film evaporation.* International Journal of Heat and Mass Transfer, 2016. **101**: p. 280-294.

29. Narayanan, S., A.G. Fedorov, and Y.K. Joshi, *Heat and mass transfer during evaporation of thin liquid films confined by nanoporous membranes subjected to air jet impingement.* International Journal of Heat and Mass Transfer, 2013. **58**(1-2): p. 300-311.

30. Sodtke, C. and P. Stephan, *Spray cooling on micro structured surfaces.* International Journal of Heat and Mass Transfer, 2007. **50**(19-20): p. 4089-4097.

31. Zhang, Z., et al., *Experimental investigation of spray cooling on micro-, nano-and hybrid-structured surfaces.* International Journal of Heat and Mass Transfer, 2015. **80**: p. 26-37.

32. Blake, T., et al., *Droplet spreading: a microscopic approach.* Colloids and Surfaces A: Physicochemical and Engineering Aspects, 1999. **149**(1-3): p. 123-130.

33. De Ruijter, M.J., J. De Coninck, and G. Oshanin, *Droplet spreading: partial wetting regime revisited.* Langmuir, 1999. **15**(6): p. 2209-2216.

34. Poudel, S., A. Zou, and S.C. Maroo, *Wicking in Cross-Connected Buried Nanochannels.* The Journal of Physical Chemistry C, 2019. **123**(38): p. 23529-23534.

35. Singh, S.K., et al., *Wetting dynamics and evaporation of sessile droplets on nano-porous alumina surfaces.* Colloids and Surfaces A: Physicochemical and Engineering Aspects, 2013. **432**: p. 71-81.

36. Wemp, C.K. and V.P. Carey, *Water wicking and droplet spreading on randomly structured thin nanoporous layers.* Langmuir, 2017. **33**(50): p. 14513-14525.

37. Mehrizi, A.A. and H. Wang, *Evaporating thin film profile near the contact line of a partially wetting water droplet under environmental heating.* International Journal of Heat and Mass Transfer, 2017. **107**: p. 1-5.

38. Bonn, D., et al., *Wetting and spreading.* Reviews of modern physics, 2009. **81**(2): p. 739.

39. Carroll, G.T., et al., *Photochemical micropatterning of carbohydrates on a surface.* Langmuir, 2006. **22**(6): p. 2899-2905.

40. Fuller, S.B., E.J. Wilhelm, and J.M. Jacobson, *Ink-jet printed nanoparticle microelectromechanical systems.* Journal of Microelectromechanical systems, 2002. **11**(1): p. 54-60.

41. Tarozzi, L., A. Muscio, and P. Tartarini, *Experimental tests of dropwise cooling on infrared-transparent media.* Experimental Thermal and Fluid Science, 2007. **31**(8): p. 857-865.

42. Xiao, R., R. Enright, and E.N. Wang, *Prediction and optimization of liquid propagation in micropillar arrays.* Langmuir, 2010. **26**(19): p. 15070-15075.

43. Ahn, H.S., et al., *The effect of capillary wicking action of micro/nano structures on pool boiling critical heat flux.* International Journal of Heat and Mass Transfer, 2012. **55**(1-3): p. 89-92.

44. Chen, R., et al., *Nanowires for enhanced boiling heat transfer.* Nano letters, 2009. **9**(2): p. 548-553.

45. Opoku, R. and J.P. Kizito, *Experimental investigation of heat transfer characteristics and performance of smooth and wicking surfaces in spray cooling for high heat flux applications.* Results in Engineering, 2020. **6**: p. 100119.

46. Zou, A., et al., *Pool boiling coupled with nanoscale evaporation using buried nanochannels.* Langmuir, 2019. **35**(39): p. 12689-12693.

47. Tang, H., et al., *Review of applications and developments of ultra-thin micro heat pipes for electronic cooling.* Applied energy, 2018. **223**: p. 383-400.

48. Farokhnia, N., et al., *Rational micro/nanostructuring for thin-film evaporation.* The Journal of Physical Chemistry C, 2016. **120**(16): p. 8742-8750.

49. Mai, T.T., et al., *Dynamics of wicking in silicon nanopillars fabricated with interference lithography and metal-assisted chemical etching.* Langmuir, 2012. **28**(31): p. 11465-11471.

50. Brinkman, H.C., *A calculation of the viscous force exerted by a flowing fluid on a dense swarm of particles.* Flow, Turbulence and Combustion, 1949. **1**(1): p. 27-34.

51. Raghupathi, P. and S. Kandlikar, *Pool boiling enhancement through contact line augmentation.* Applied Physics Letters, 2017. **110**(20): p. 204101.

52. Zhang, Z., et al., *Experimental investigation of spray cooling on smooth and micro-structured surfaces.* International Journal of Heat and Mass Transfer, 2014. **76**: p. 366-375.

53. Kim, J.H., *Spray cooling heat transfer: The state of the art.* International Journal of Heat and Fluid Flow, 2007. **28**(4): p. 753-767.

54. Wemp, C.K. and V.P. Carey, *Tuning Superhydrophilic Nanostructured Surfaces to Maximize Water Droplet Evaporation Heat Transfer Performance.* Journal of Heat Transfer-Transactions of the Asme, 2018. **140**(10).

55. Plawsky, J.L., et al., *Nano- and Microstructures for Thin-Film Evaporation-a Review.* Nanoscale and Microscale Thermophysical Engineering, 2014. **18**(3): p. 251-269.

56. Kwon, H.M., J.C. Bird, and K.K. Varanasi, *Increasing Leidenfrost point using micro-nano hierarchical surface structures.* Applied Physics Letters, 2013. **103**(20).

57. Xiang, C.J., et al., *Large-Scale, Uniform, and Superhydrophobic Titania Nanotubes at the Inner Surface of 1000 mm Long Titanium Tubes.* Journal of Physical Chemistry C, 2017. **121**(28): p. 15448-15455.

58. Chen, R., et al., *Nanowires for Enhanced Boiling Heat Transfer.* Nano Letters, 2009. **9**(2): p. 548-553.

59. Auliano, M., et al., *Can Wicking Control Droplet Cooling?* Langmuir, 2019. **35**(20): p. 6562-6570.

60. Zhang, Z., et al., *Experimental investigation of spray cooling on micro-, nano- and hybrid-structured surfaces.* International Journal of Heat and Mass Transfer, 2015. **80**: p. 26-37.

61. Zhang, Z., et al., *Experimental investigation of spray cooling on smooth and micro-structured surfaces.* International Journal of Heat and Mass Transfer, 2014. **76**: p. 366-375.

62. Dash, S. and S.V. Garimella, *Droplet evaporation on heated hydrophobic and superhydrophobic surfaces.* Physical Review E, 2014. **89**(4): p. 042402.

63. Sazhin, S.S., *Advanced models of fuel droplet heating and evaporation.* Progress in energy and combustion science, 2006. **32**(2): p. 162-214.

64. Tran, T., et al., *Drop impact on superheated surfaces.* Physical review letters, 2012. **108**(3): p. 036101.

65. Carey, V.P., et al. *Mechanism Interaction During Droplet Evaporation on Nanostructured Hydrophilic Surfaces*. in *ASME International Mechanical Engineering Congress and Exposition*. 2018. American Society of Mechanical Engineers.

66. Bonn, D., et al., *Wetting and spreading.* Reviews of Modern Physics, 2009. **81**(2): p. 739-805.

67. Carroll, G.T., et al., *Photochemical micropatterning of carbohydrates on a surface.* Langmuir, 2006. **22**(6): p. 2899-2905.

68. Poudel, S., A. Zou, and S.C. Maroo, *Wicking in Cross-Connected Buried Nanochannels.* Journal of Physical Chemistry C, 2019. **123**(38): p. 23529-23534.

69. Poudel, S., A. Zou, and S.C. Maroo, *Droplet evaporation on porous nanochannels for high heat flux dissipation.* ACS applied materials & interfaces, 2020. **13**(1): p. 1853-1860.

70. Kim, H.D. and M.H. Kim, *Effect of nanoparticle deposition on capillary wicking that influences the critical heat flux in nanofluids.* Applied Physics Letters, 2007. **91**(1).

71. Silk, E.A., E.L. Golliher, and R.P. Selvam, *Spray cooling heat transfer: Technology overview and assessment of future challenges for micro-gravity application.* Energy Conversion and Management, 2008. **49**(3): p. 453-468.

72. Crabtree, G.W. and N.S. Lewis, *Solar energy conversion.* Physics today, 2007. **60**(3): p. 37-42.

73. Ajuria, J., et al., *Inverted ITO-free organic solar cells based on p and n semiconducting oxides. New designs for integration in tandem cells, top or bottom detecting devices, and photovoltaic windows.* Energy & Environmental Science, 2011. **4**(2): p. 453-458.

74. Essig, S., et al., *Raising the one-sun conversion efficiency of III–V/Si solar cells to 32.8% for two junctions and 35.9% for three junctions.* Nature Energy, 2017. **2**(9): p. 1-9.

75. Escarré, J., et al., *Geometric light trapping for high efficiency thin film silicon solar cells.* Solar Energy Materials and Solar Cells, 2012. **98**: p. 185-190.

76. Forbes, L., *Texturing, reflectivity, diffuse scattering and light trapping in silicon solar cells.* Solar Energy, 2012. **86**(1): p. 319-325.

77. Lasich, J., et al. *World's first demonstration of a 140kWp Heliostat Concentrator PV (HCPV) system*. in *2009 34th IEEE Photovoltaic Specialists Conference (PVSC)*. 2009. IEEE.

78. Schuetz, M.A., et al., *Design and construction of a∼7× low-concentration photovoltaic system based on compound parabolic concentrators.* IEEE journal of photovoltaics, 2012. **2**(3): p. 382-386.

79. Al-Rifai, M.H., J. Carstensen, and H. Föll, *A simple passivation technique for the edge area of silicon solar cells improves the efficiency.* Solar energy materials and solar cells, 2002. **72**(1-4): p. 327-333.

80. Han, L., et al., *Improvement of efficiency of dye-sensitized solar cells by reduction of internal resistance.* Applied Physics Letters, 2005. **86**(21): p. 213501.

81. Ghimire, N., et al., *Mitigating Open-Circuit Voltage Loss in Pb–Sn Low-Band Gap Perovskite Solar Cells via Additive Engineering.* ACS Applied Energy Materials, 2021.

82. Tang, R., et al., *Highly efficient and stable planar heterojunction solar cell based on sputtered and post-selenized Sb2Se3 thin film.* Nano Energy, 2019. **64**: p. 103929.

83. Yuan, J., et al., *Surface Trap States Passivation for High-Performance Inorganic Perovskite Solar Cells.* Solar RRL, 2018. **2**(10): p. 1800188.

84. Cheng, Y.-J., S.-H. Yang, and C.-S. Hsu, *Synthesis of conjugated polymers for organic solar cell applications.* Chemical reviews, 2009. **109**(11): p. 5868-5923.

85. Xue, R., et al., *Organic solar cell materials toward commercialization.* Small, 2018. **14**(41): p. 1801793.

86. Yuan, J., et al., *Single-junction organic solar cell with over 15% efficiency using fused-ring acceptor with electron-deficient core.* Joule, 2019. **3**(4): p. 1140-1151.

87. Boudreault, P.-L.T., A. Najari, and M. Leclerc, *Processable low-bandgap polymers for photovoltaic applications.* Chemistry of Materials, 2011. **23**(3): p. 456-469.

88. Dou, L., et al., *Tandem polymer solar cells featuring a spectrally matched low-bandgap polymer.* Nature Photonics, 2012. **6**(3): p. 180-185.

89. Daher, D.H., et al., *Impact of tropical desert maritime climate on the performance of a PV grid-connected power plant.* Renewable energy, 2018. **125**: p. 729-737.

90. Dewi, T., P. Risma, and Y. Oktarina. *A Review of Factors Affecting the Efficiency and Output of a PV system Applied in Tropical Climate*. in *IOP Conference Series: Earth and Environmental Science*. 2019. IOP Publishing.

91. Ogbomo, O.O., et al., *A review of photovoltaic module technologies for increased performance in tropical climate.* Renewable and Sustainable Energy Reviews, 2017. **75**: p. 1225-1238.

92. Du, D., J. Darkwa, and G. Kokogiannakis, *Thermal management systems for photovoltaics (PV) installations: a critical review.* Solar Energy, 2013. **97**: p. 238-254.

93. Hasanuzzaman, M., et al., *Global advancement of cooling technologies for PV systems: a review.* Solar Energy, 2016. **137**: p. 25-45.

94. Sharma, R., et al., *Life span and overall performance enhancement of Solar Photovoltaic cell using water as coolant: A recent review.* Materials Today: Proceedings, 2018. **5**(9): p. 18202-18210.

95. Green, M.A., et al., *Solar cell efficiency tables (version 52).* Progress in Photovoltaics: Research and Applications, 2018. **26**(7): p. 427-436.

96. Abd-Elhady, M., Z. Serag, and H. Kandil, *An innovative solution to the overheating problem of PV panels.* Energy conversion and management, 2018. **157**: p. 452-459.

97. Bahaidarah, H.M., A.A. Baloch, and P. Gandhidasan, *Uniform cooling of photovoltaic panels: A review.* Renewable and Sustainable Energy Reviews, 2016. **57**: p. 1520-1544.

98. Najafi, H. and K.A. Woodbury, *Optimization of a cooling system based on Peltier effect for photovoltaic cells.* Solar Energy, 2013. **91**: p. 152-160.

99. Waqas, A. and J. Ji, *Thermal management of conventional PV panel using PCM with movable shutters–A numerical study.* Solar Energy, 2017. **158**: p. 797-807.

100. Rabie, R., et al., *Thermal management of concentrator photovoltaic systems using new configurations of phase change material heat sinks.* Solar Energy, 2019. **183**: p. 632-652.

101. Rejeb, O., et al., *Novel solar PV/Thermal collector design for the enhancement of thermal and electrical performances.* Renewable Energy, 2020. **146**: p. 610-627.

102. Vaillon, R., et al., *Pathways for mitigating thermal losses in solar photovoltaics.* Scientific reports, 2018. **8**(1): p. 1-9.

103. Yan, H., S. Ye, and D.S. Seferos, *Unusual Performance Increase in Polymer Solar Cells by Cooling a Hot Donor/Acceptor Ink in a Good Solvent.* ACS applied materials & interfaces, 2018. **10**(1): p. 979-984.

104. Castanheira, A.F., J.F. Fernandes, and P.C. Branco, *Demonstration project of a cooling system for existing PV power plants in Portugal.* Applied Energy, 2018. **211**: p. 1297-1307.

105. Hadipour, A., M.R. Zargarabadi, and S. Rashidi, *An efficient pulsed-spray water cooling system for photovoltaic panels: Experimental study and cost analysis.* Renewable Energy, 2021. **164**: p. 867-875.

106. Mittelman, G., A. Alshare, and J.H. Davidson, *A model and heat transfer correlation for rooftop integrated photovoltaics with a passive air cooling channel.* Solar Energy, 2009. **83**(8): p. 1150-1160.

107. Nižetić, S., A. Papadopoulos, and E. Giama, *Comprehensive analysis and general economic-environmental evaluation of cooling techniques for photovoltaic panels, Part I: Passive cooling techniques.* Energy Conversion and Management, 2017. **149**: p. 334-354.

108. Mazón-Hernández, R., et al., *Improving the electrical parameters of a photovoltaic panel by means of an induced or forced air stream.* International Journal of Photoenergy, 2013. **2013**.

109. Jakhar, S., M.S. Soni, and N. Gakkhar, *An integrated photovoltaic thermal solar (IPVTS) system with earth water heat exchanger cooling: Energy and exergy analysis.* Solar Energy, 2017. **157**: p. 81-93.

110. Alami, A.H., *Effects of evaporative cooling on efficiency of photovoltaic modules.* Energy Conversion and Management, 2014. **77**: p. 668-679.

111. Chandrasekar, M. and T. Senthilkumar, *Experimental demonstration of enhanced solar energy utilization in flat PV (photovoltaic) modules cooled by heat spreaders in conjunction with cotton wick structures.* Energy, 2015. **90**: p. 1401-1410.

112. Nižetić, S., E. Giama, and A. Papadopoulos, *Comprehensive analysis and general economic-environmental evaluation of cooling techniques for photovoltaic panels, Part II: Active cooling techniques.* Energy Conversion and Management, 2018. **155**: p. 301-323.

113. Bahaidarah, H.M., *Experimental performance evaluation and modeling of jet impingement cooling for thermal management of photovoltaics.* Solar Energy, 2016. **135**: p. 605-617.

114. Huang, M., P. Eames, and B. Norton, *Phase change materials for limiting temperature rise in building integrated photovoltaics.* Solar Energy, 2006. **80**(9): p. 1121-1130.

115. Alizadeh, H., et al., *Numerical simulation of PV cooling by using single turn pulsating heat pipe.* International Journal of Heat and Mass Transfer, 2018. **127**: p. 203-208.

116. Shittu, S., et al., *Comparative study of a concentrated photovoltaic-thermoelectric system with and without flat plate heat pipe.* Energy Conversion and Management, 2019. **193**: p. 1-14.

117. Bai, A., et al., *Technical and economic effects of cooling of monocrystalline photovoltaic modules under Hungarian conditions.* Renewable and Sustainable Energy Reviews, 2016. **60**: p. 1086-1099.

118. Nižetić, S., et al., *Water spray cooling technique applied on a photovoltaic panel: The performance response.* Energy conversion and management, 2016. **108**: p. 287-296.

119. Krishnan, S.R., J. Bal, and S.A. Putnam, *A simple analytic model for predicting the wicking velocity in micropillar arrays.* Scientific reports, 2019. **9**(1): p. 1-9.

120. Lee, J., et al., *Capillary wicking in hierarchically textured copper nanowire arrays.* ACS applied materials & interfaces, 2018. **11**(1): p. 1546-1554.

121. Fischer, S., et al., *Effect of nano-textured heater surfaces on evaporation at a single meniscus.* International Journal of Heat and Mass Transfer, 2017. **108**: p. 2444-2450.

122. Jasvanth, V., et al., *Numerical investigation of an evaporating meniscus in a heated capillary slot.* Heat and Mass Transfer, 2019. **55**(12): p. 3675-3688.

123. Poudel, S., A. Zou, and S.C. Maroo, *Droplet Evaporation on Porous Nanochannels for High Heat Flux Dissipation.* ACS Applied Materials & Interfaces, 2020.

124. Du, Y., et al., *Evaluation of photovoltaic panel temperature in realistic scenarios.* Energy Conversion and Management, 2016. **108**: p. 60-67.

125. Poudel, S., A. Zou, and S.C. Maroo, *Thermal Management of Photovoltaics using Porous Nanochannels.* arXiv preprint arXiv:2105.04745, 2021.

126. García, M.A. and J. Balenzategui, *Estimation of photovoltaic module yearly temperature and performance based on nominal operation cell temperature calculations.* Renewable energy, 2004. **29**(12): p. 1997-2010.

127. Verma, S., et al., *Cooling techniques of the PV module: a review.* Materials Today: Proceedings, 2021. **38**: p. 253-258.

128. Hasan, A., et al., *Yearly energy performance of a photovoltaic-phase change material (PV-PCM) system in hot climate.* Solar Energy, 2017. **146**: p. 417-429.

129. Yang, D. and H. Yin, *Energy conversion efficiency of a novel hybrid solar system for photovoltaic, thermoelectric, and heat utilization.* IEEE Transactions on Energy Conversion, 2011. **26**(2): p. 662-670.

130. Derjaguin, B. and N. Churaev, *On the question of determining the concept of disjoining pressure and its role in the equilibrium and flow of thin films.* Journal of Colloid and Interface Science, 1978. **66**(3): p. 389-398.

131. Chatterjee, A., J.L. Plawsky, and P.C. Wayner Jr, *Disjoining pressure and capillarity in the constrained vapor bubble heat transfer system.* Advances in colloid and interface science, 2011. **168**(1-2): p. 40-49.

132. Aksoy, Y.T., et al., *The Impact of Nanofluids on Droplet/Spray Cooling of a Heated Surface: A Critical Review.* Energies, 2021. **14**(1): p. 80.

133. Nguyen, T.T., et al., *Rip currents: A spontaneous heat transfer enhancement mechanism in a wickless heat pipe.* International Journal of Heat and Mass Transfer, 2020. **149**: p. 119170.

134. Wasan, D., A. Nikolov, and K. Kondiparty, *The wetting and spreading of nanofluids on solids: Role of the structural disjoining pressure.* Current Opinion in Colloid & Interface Science, 2011. **16**(4): p. 344-349.

135. Joanny, J. and P. De Gennes, *Role of long-range forces in heterogeneous nucleation.* Journal of colloid and interface science, 1986. **111**(1): p. 94-101.

136. Kheshgi, H.S. and L. Scriven, *Dewetting: Nucleation and growth of dry regions.* Chemical engineering science, 1991. **46**(2): p. 519-526.

137. Panchamgam, S.S., et al., *Comprehensive experimental and theoretical study of fluid flow and heat transfer in a microscopic evaporating meniscus in a miniature heat exchanger.* International Journal of Heat and Mass Transfer, 2008. **51**(21-22): p. 5368-5379.

138. Mancinelli, R., et al., *Multiscale approach to the structural study of water confined in MCM41.* The Journal of Physical Chemistry B, 2009. **113**(50): p. 16169-16177.

139. Tsukahara, T., et al., *NMR study of water molecules confined in extended nanospaces.* Angewandte Chemie, 2007. **119**(7): p. 1199-1202.

140. Tsukahara, T., et al., *NMR studies of structure and dynamics of liquid molecules confined in extended nanospaces.* The Journal of Physical Chemistry B, 2009. **113**(31): p. 10808-10816.

141. Elliott, J.A., *Gibbsian surface thermodynamics.* The Journal of Physical Chemistry B, 2020. **124**(48): p. 10859-10878.

142. Zou, A., et al., *Disjoining Pressure of Water in Nanochannels.* Nano Letters, 2021.

143. Yoon, R.-H. and B.S. Aksoy, *Hydrophobic forces in thin water films stabilized by dodecylammonium chloride.* Journal of colloid and interface science, 1999. **211**(1): p. 1-10.

144. Wasan, D.T. and A.D. Nikolov, *Spreading of nanofluids on solids.* Nature, 2003. **423**(6936): p. 156-159.

145. Wheeler, T.D. and A.D. Stroock, *The transpiration of water at negative pressures in a synthetic tree.* Nature, 2008. **455**(7210): p. 208-212.

146. Zou, A., M. Gupta, and S.C. Maroo, *Transpiration Mechanism in Confined Nanopores.* The journal of physical chemistry letters, 2020. **11**(9): p. 3637-3641.

147. Fanourakis, D., et al., *Pore size regulates operating stomatal conductance, while stomatal densities drive the partitioning of conductance between leaf sides.* Annals of botany, 2015. **115**(4): p. 555-565.

148. Chichiriccò, G. and A. Poma, *Penetration and toxicity of nanomaterials in higher plants.* Nanomaterials, 2015. **5**(2): p. 851-873.

149. Tyree, M.T., *Plant hydraulics: the ascent of water.* Nature, 2003. **423**(6943): p. 923-923.

150. Poudel, S., A. Zou, and S.C. Maroo, *Disjoining Pressure Driven Transpiration of Water in a Simulated Tree.* arXiv preprint arXiv:2111.10927, 2021.

151. Fluent, F., *User's Guide, Fluent.* Inc., New Hampshire, 1998.

152. CFX-Solver, A., *Theory guide.* Release ll, 2006.

153. Brackbill, J.U., D.B. Kothe, and C. Zemach, *A continuum method for modeling surface tension.* Journal of computational physics, 1992. **100**(2): p. 335-354.

154. Roache, P.J., *Quantification of uncertainty in computational fluid dynamics.* Annual review of fluid Mechanics, 1997. **29**(1): p. 123-160.

155. Koch, G.W. and A.L. Fredeen, *Transport challenges in tall trees*, in *Vascular transport in plants*. 2005, Elsevier. p. 437-456.

156. Ma, W. *Study on the water flow in the xylem of plants*. in *AIP Conference Proceedings*. 2017. AIP Publishing LLC.

157. Carey, V.P., *Liquid-vapor phase-change phenomena, Hemisphere Pub.* Corp: Washington, DC, 1992.

158. Paul, B., *Compilation of evaporation coefficients.* ARS Journal, 1962. **32**(9): p. 1321-1328.

159. Koch, G.W., et al., *The limits to tree height.* Nature, 2004. **428**(6985): p. 851-854.

160. Ryan, M.G. and B.J. Yoder, *Hydraulic limits to tree height and tree growth.* Bioscience, 1997. **47**(4): p. 235-242.

161. Biwole, P.H., P. Eclache, and F. Kuznik, *Phase-change materials to improve solar panel's performance.* Energy and Buildings, 2013. **62**: p. 59-67.

162. Jaworski, M., *Thermal performance of heat spreader for electronics cooling with incorporated phase change material.* Applied Thermal Engineering, 2012. **35**: p. 212-219.

163. Kandasamy, R., X.-Q. Wang, and A.S. Mujumdar, *Application of phase change materials in thermal management of electronics.* Applied Thermal Engineering, 2007. **27**(17-18): p. 2822-2832.

164. Lee, K.O., et al., *Assessing the integration of a thin phase change material (PCM) layer in a residential building wall for heat transfer reduction and management.* Applied Energy, 2015. **137**: p. 699-706.

165. Rahman, M.M., et al., *Supercritical water heat transfer for nuclear reactor applications: A review.* Annals of Nuclear Energy, 2016. **97**: p. 53-65.

166. Shon, J., H. Kim, and K. Lee, *Improved heat storage rate for an automobile coolant waste heat recovery system using phase-change material in a fin–tube heat exchanger.* Applied energy, 2014. **113**: p. 680-689.

167. Kim, B.S., et al., *Interfacial wicking dynamics and its impact on critical heat flux of boiling heat transfer.* Applied Physics Letters, 2014. **105**(19): p. 191601.

168. Rokoni, A., D.-O. Kim, and Y. Sun, *Micropattern-controlled wicking enhancement in hierarchical micro/nanostructures.* Soft matter, 2019. **15**(32): p. 6518-6529.

169. Chung, J., T. Chen, and S. Maroo, *A review of recent progress on nano/micro scale nucleate boiling fundamentals.* Frontiers in Heat and Mass Transfer (FHMT), 2011. **2**(2).

170. Dong, L., X. Quan, and P. Cheng, *An experimental investigation of enhanced pool boiling heat transfer from surfaces with micro/nano-structures.* International Journal of Heat and Mass Transfer, 2014. **71**: p. 189-196.

171. Khan, S.A., M.A. Atieh, and M. Koç, *Micro-nano scale surface coating for nucleate boiling heat transfer: a critical review.* Energies, 2018. **11**(11): p. 3189.

172. Launay, S., et al., *Hybrid micro-nano structured thermal interfaces for pool boiling heat transfer enhancement.* Microelectronics Journal, 2006. **37**(11): p. 1158-1164.

173. Chen, J.-n., et al., *Phenomenon and mechanism of spray cooling on nanowire arrayed and hybrid micro/nanostructured surfaces.* Journal of Heat Transfer, 2018. **140**(11).

174. Xu, R.-N., et al., *Experimental investigation of closed loop spray cooling with micro-and hybrid micro-/nano-engineered surfaces.* Applied Thermal Engineering, 2020. **180**: p. 115697.

175. Seddon, J.R., et al., *Surface bubble nucleation stability.* Physical review letters, 2011. **106**(5): p. 056101.

176. Wen, R., et al., *Enhanced bubble nucleation and liquid rewetting for highly efficient boiling heat transfer on two-level hierarchical surfaces with patterned copper nanowire arrays.* Nano Energy, 2017. **38**: p. 59-65.

177. Zou, A., M. Gupta, and S.C. Maroo, *Origin, evolution, and movement of microlayer in pool boiling.* The journal of physical chemistry letters, 2018. **9**(14): p. 3863-3869.

178. Zou, A., et al., *Disjoining Pressure of Water in Nanochannels.* Nano letters, 2021. **21**(18): p. 7769-7774.

179. Bao, B., et al., *Bubble nucleation and growth in nanochannels.* Physical Chemistry Chemical Physics, 2017. **19**(12): p. 8223-8229.

180. Hasan, M.N., et al. *Nano scale dynamics of bubble nucleation in confined liquid subjected to rapid cooling: Effect of solid-liquid interfacial wettability*. in *AIP Conference Proceedings*. 2017. AIP Publishing LLC.

181. Hou, Z., et al., *Manipulating the topology of nanoscale skyrmion bubbles by spatially geometric confinement.* ACS nano, 2019. **13**(1): p. 922-929.

182. Gupta, M., A. Zou, and S.C. Maroo, *Onset and critical radius of heterogeneous bubble nucleation.* Applied Physics Letters, 2020. **116**(10): p. 103704.

183. Zhang, Y., et al., *Molecular dynamics simulations of He bubble nucleation at grain boundaries.* Journal of Physics: Condensed Matter, 2012. **24**(30): p. 305005.

184. Witharana, S., et al., *Bubble nucleation on nano-to micro-size cavities and posts: an experimental validation of classical theory.* Journal of Applied Physics, 2012. **112**(6): p. 064904.

185. Yuan, H., et al., *Heterogeneous bubble nucleation model on heated surface based on free energy analysis.* International Journal of Heat and Mass Transfer, 2018. **122**: p. 1198-1209.

186. Yuan, H., et al., *Heterogeneous bubble nucleation on heated surface from insoluble gas.* International Journal of Heat and Mass Transfer, 2016. **101**: p. 1185-1192.

187. Cowgill, D.F., *Helium nano-bubble evolution in aging metal tritides.* Fusion science and technology, 2005. **48**(1): p. 539-544.

188. Fluent, A., *Ansys fluent.* Academic Research. Release, 2015. **14**.

189. Fluent, A., *Fluent 14.0 user's guide.* ANSYS FLUENT Inc, 2011.

Biography

Sajag Poudel is a Ph.D. Candidate in the Department of Mechanical and Aerospace Engineering at Syracuse University, NY. He has performed research in the field of thermal management employing phase-change heat-transfer by using micro/nano structured geometries. His research findings have been published in journals including ACS Nano Letters, ACS Applied Materials and Interfaces, Langmuir, Journal of Physical Chemistry C, Physics of Fluids, etc. He was born and brought up in the Himalayan nation, Nepal, and completed his previous education from India including M.S. in Aerospace Engineering from Indian Institute of Technology Kanpur. His research interest lies in the field of energy system, heat-transfer, numerical modeling, and fluid mechanics. He has won the First Prize Award for the best presentation during a Symposium organized by the American Physical Society and has recently been awarded with the National Science Foundation Research Grant (NSF-INTERN) to pursue 5 months Research Internship on High-Temperature Energy Conversion at the Oak Ridge National Laboratory, TN. He is joining the U.S. Department of Energy – Argonne National Laboratory as a Postdoctoral Appointee in January 2022.